Synthesis and characterization of mixed-metal hybrid perovskites

Aniruddha Ray
4516656

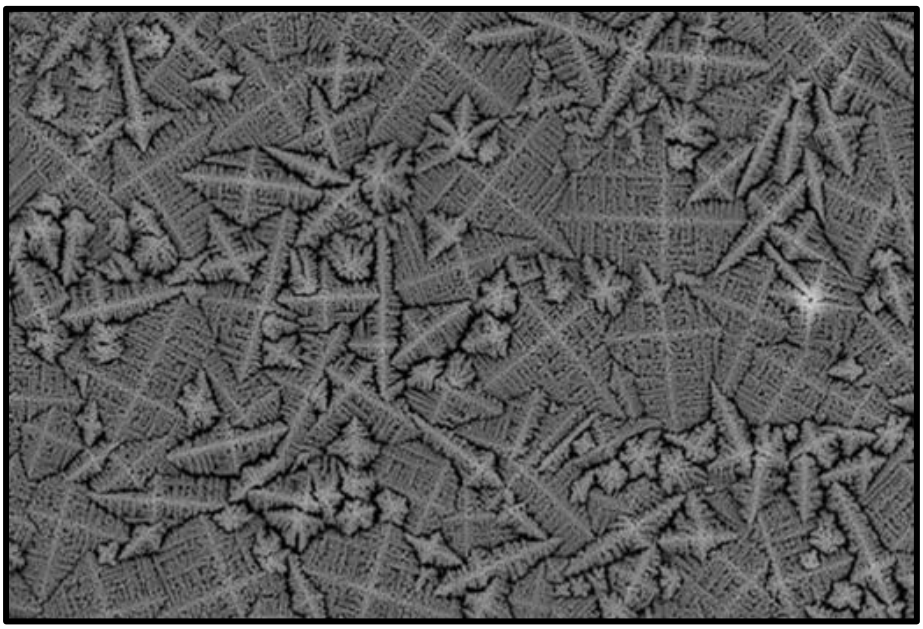

TU Delft

Synthesis and characterization of mixed-metal hybrid perovskites

By

Aniruddha Ray

in partial fulfilment of the requirements for the degree of

Master of Science
in Materials Engineering and Applications

at the Delft University of Technology,
to be defended publicly on Thursday August 24, 2017 at 14:15 PM.

Supervisor:	Dr. Davide Bartesaghi	
	Dr. Tom J. Savenije	
	Dr. Amarante J. Bottger	
Thesis committee:	Dr. Amarante J. Bottger	TU Delft
	Dr. Tom J. Savenije	TU Delft
	Dr. Davide Bartesaghi	TU Delft
	Prof. Jilt Sietsma	TU Delft
	Dr. Vera Popovich	TU Delft

TU Delft

Abstract

Metal halide perovskites have attracted a lot of attention over the last decade as a potential low cost alternative to traditional silicon based photovoltaics. Solar cells based on these materials have already achieved power conversion efficiency (PCE) of 22%. However, these high performing compositions are lead containing which is regarded as a potential risk for humans as well as the environment. A lot of research effort has been put into completely replacing lead with other group-14 elements such as tin and germanium, due to their similar sizes and electronic configuration. These kinds of perovskites have shown promising optoelectronic properties but are highly unstable due to the easy oxidation of tin and germanium.

In this thesis an alternative approach of mixing lead with other smaller divalent metal cations is explored. $MAPbI_3$ is synthesized using lead acetate due to the facile removal of byproducts and its tolerance for mixing with other metal salts. The alternate metal salts were selected on the basis of their solubility in commonly used solvents and the suitability of the crystal structure of the precursor compound for perovskite structure formation. We found manganese to be a suitable substituent of lead and the upper limit for these mixed metal perovskites after geometrical calculations as well as experimental verification is found to be around 30%. Though the mixed metal compositions maintain the tetragonal crystal structure of lead based perovskites, a secondary crystalline phase is observed with increased lead substitution. Efforts are made to identify its composition and to remove it by optimizing the thermal treatment as well as the ratio between the other precursors. The optimized recipe for 30% lead substituted showed phase purity as well as good optical and electronic properties. Detailed compositional analysis revealed that, unlike $MAPbI_3$ synthesized using chloride based precursors, in these mixed metal compositions chlorine is also incorporated in the films containing manganese especially near the substrate interface. This suggests that the smaller metal cation has an affinity for the smaller halide anion and that it plays a key role in the initiation of nucleation in such mixed metal (Pb:Mn) compositions. Finally, solar cells were made as a proof of concept incorporating these mixed metal perovskites and devices with up to 1.45% PCE were obtained.

Table of Contents

Acknowledgements

I take this opportunity to express my gratitude to the people who have been instrumental in the successful completion of this project.

Firstly, I would like to thank my supervisor Davide Bartesaghi for his constant guidance and enthusiastic support and involvement with the project. His calm and composed approach to research is something I have learned immensely from. I would also like to thank Dr. Tom Savenije and Dr. Amarante Bottger for providing me the opportunity to continue researching and studying this fascinating class of materials and also for steering me in the right direction whenever I needed it. I am also grateful to them for always making the time for a discussion regarding the results and for all their constructive suggestions.

I would also like to extedn my gratitude towards Ruben for all his help in and out of the labs. Finally, I would like to thank my partners in lab, Jetsabel, Sanjana and Eva for making the whole experience higly enjoyable.

Finally, I would like to thank my parents and friends who have been a constant source of motivation and positivity.

Abbreviations

PCE	Power Conversion Efficiency
MA	Methylammonium
Ac	Acetate (CH_3COO^-)
DMF	N,N-dimethylformamide
DMSO	Dimethyl sulfoxide
HTM	Hole Transport Material
PEDOT:PSS	Poly(3,4-ethylenedioxythiophene) doped with poly(styrene sulfonate)
XRD	X-ray Diffraction
SEM	Scanning Electron Microscopy
EDX	Energy-Dispersive X-ray Spectroscopy
XPS	X-ray Photoelectron Spectroscopy
BSE	Back-Scattered Electrons
UV-VIS	Ultraviolet-Visible
PL	Photoluminescence
TRMC	Time Resolved Microwave Conductivity

Introduction

Worldwide, governments are setting themselves targets to combat environmental climate change and express their commitment towards adopting renewable energy sources. European Union recently charted a new regionally binding target, according to which it requires a minimum of 27% of all energy consumption to be met by renewable means by 2030 [1]. Furthermore, in the last few years, solar photovoltaics (PV) has especially seen a big jump in developing countries due to increased awareness of its potential to alleviate pollution and CO_2 emission without hindering the rapid economic growth these areas are experiencing [1].

Mainstream silicon solar cell technology aided by the exponential growth in the micro-fabrication industry has continued to gain substantial reduction in its manufacturing costs. This combined with abundant supply of raw materials and device stability has assured its place as the most widely used PV technology. However, manufacturing monocrystalline silicon is highly energy intensive requiring extremely precise processing control. Furthermore, due to the indirect bandgap of silicon, thick layers are needed to sufficiently absorb the appropriate range of the solar spectrum. The brittle nature of these thick layers of crystalline silicon along certain cleavage planes [2] results in losses during manufacturing and also require thick expensive glass supports that limit their areas of application. Research breakthroughs have stagnated in this field, opening up opportunities for competing technologies that promise significantly cheaper and more environmental friendly processing methods as well as higher energy densities.

A new generation of hybrid halide perovskites, recently rediscovered in the last decade offers promising results on these fronts [3]. They have exceptional optoelectronic properties and are easily fabricated using inexpensive precursors and low temperature solution-phase techniques that have already shown adaptability to roll-to-roll (R2R) processes on polymer foil substrates [4]. Photovoltaic devices incorporating these hybrid materials have gone from 3.8% [5] PCE in 2009 to 22.1% in 2017 [6]. This structure has also been found to be highly tolerant to the incorporation of various elements showing composition dependent properties such as a tunable optical direct bandgap. This tunability is being exploited to optimize them for applications such as the top component in tandem PV architectures [7] as well as potential building materials [8][9]. These materials however have two key hurdles that are at the focal point of research related to PV applications. The first has been to study and solve their intrinsic and extrinsic stability issues. While the other is to find less toxic alternatives to lead, a central component in all high performing perovskite compositions, and this is also the main topic of this thesis.

1.1 Salient Features of hybrid halide perovskites

1.1.1 Structure

The term perovskite was originally used to describe the crystal structure of a naturally occurring mineral calcium titanate ($CaTiO_3$). Due to the complex interplay between the charge, spin and structural properties, this family of inorganic materials was found to exhibit a myriad of novel and exciting phenomena like superconductivity, magnetoresistance, ferroelectricity, magneto-electricity, anti-ferromagnetism, anti-ferroelectricity [10].

Nowadays metal halide compounds have also been fabricated with a similar structure and stoichiometry ABX_3 as seen in the figure 1. The B site inorganic cation and the X site halide

anion form an octahedral inorganic framework, with the A site cation (organic/inorganic) located in the centre occupying the cuboctahedral cavity. Furthermore, these materials have shown remarkable structural tunability based on the connectivity of the BX_6 octahedra. Forming 3D corner-sharing structures, to multilayered 2D networks as well as all the way down to isolated 0D octahedral clusters [11]. The size of the A site cation has been found to determine the dimensionality of the octahedral framework. [11]. However, materials adopting these structures also shown an affinity for undergoing phase transitions in response to temperature and pressure. Cubic, tetragonal, trigonal or orthorhombic are the common phases that are formed by this class of materials, all showing widely different properties.

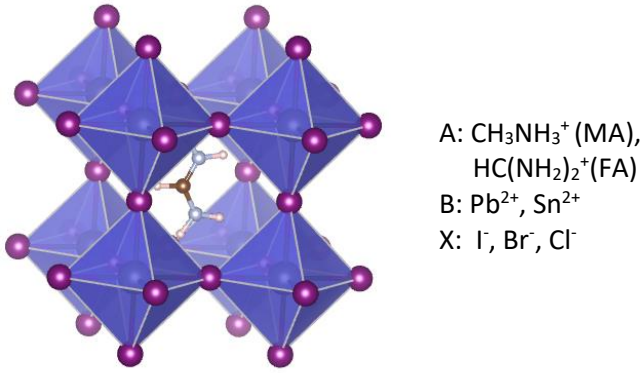

Figure 1: Structure of metal halide perovskite where A is a monovalent cation, B is a divalent metal cation and X is a monovalent halide anion.

The most commonly investigated hybrid perovskite to date is methylammonium lead triiodide ($MAPbI_3$) [10]. It has a 3-dimensional perovskite structure and has been shown to adopt three different phases, a high temperature cubic phase above 330 K, a room temperature tetragonal phase between 330 K and 160 K and a low temperature orthorhombic phase below 160 K. Transitions between such phases change the electronic band structure and the resulting optoelectronic properties of the material.

1.1.2 Unique properties

Perovskite materials have been fabricated via both solution-based as well as vacuum-based methods. Irrespective of the deposition method, they show exceptionally high visible absorption coefficients with a sharp absorption edge and in the case of $MAPbI_3$, Urbach energies as low as 15 meV. This value is close to that obtained for monocrystalline gallium arsenide compounds (GaAs) and attests to the low level of energetic disorder [12]. Moreover, in the standard $MAPbI_3$ composition, exciton binding energy have been experimentally found to be in the order of 5-6 meV at room temperature, giving the indication that the photoexcitation primarily results in the creation of free charge carriers instead of excitons. [13][14]. Once again this kind of nature is more similar to inorganic semiconductors such GaAs than to organic molecular solids which usually requires complex strategies to disassociate the excitons.

Due to its high absorption coefficients, $MAPbI_3$ was assumed to be a direct band gap material but this explanation was inconsistent with its unusually low intrinsic bimolecular recombination rates. These has been found to be up to four order of magnitude below that predicted by Langevin theory subsequently leading to one of the largest reported charge carrier diffusion lengths [15]. Recently, a rationalization of this unique blend of properties has been attributed to the presence of a mixed direct-indirect bandgap character in $MAPbI_3$. Generation of charge carriers is hypothesized to proceed via a direct transition following photoexcitation

while non geminate electron hole recombination has been found to be a thermally activated process requiring a phonon contribution [16][17][18].

However, despite the fantastic intrinsic properties mentioned above, there are other extrinsic factors that limit the optoelectronic properties in these materials. For instance, charge carrier mobilities tend to be generally hindered by charge carrier scattering at grain boundaries, dopants and a disordered energy landscape [19]. Optimizing growth conditions and the choice of precursors has made a significant difference in the types, energetics and density of traps introduced during processing [20]. Development of processing protocols has been at the crux of the enormous improvements seen in the performance of PV devices using hybrid perovskites. The specific details of the protocols used in this study such as excess organic salt, lead acetate precursors and the effect of chlorine presence in the final perovskite film are elaborated upon later.

Finally, perovskites have a highly tunable composition with unique structure-property relationships making it suitable for various applications. Size of A site cation has been shown to influence the dimensionality of the inorganic octahedral framework, as previously mentioned, and also indirectly influence the optical and electronic properties by affecting the BX_6 octahedral units [21]. Progressive substitution of the iodide at the X site with smaller bromide allows to tune the band gap of MA based perovskites between 1.5 eV and 2.3 eV [22]. From density-functional theory (DFT) calculations it has been shown that the upper valence band is dominated by the halide p orbitals while the conduction band minima is formed primarily by the 6p orbital of lead [23]. B site metal cation alloying of lead and tin has also shown a similar but non linear band gap tunable character [24].

1.3 Deposition Methods

Metal halide perovskites have been produced primarily by either precipitation from solution or vapor phase deposition. The solution based techniques can be broadly categorized into the one step, two step and the solvent engineering method [25].

The one step deposition consists in mixing stoichiometric molar ratio of MAX and PbX_2 into a low boiling point polar solvent such as γ-butyrolactone [26]. This solution is then casted into a film which is annealed at a fixed humidity and temperature to transform the precursor into perovskite crystals. Parameters that can be tuned are the precursor solution solvent, composition and temperature of casting and annealing. Higher efficiencies of PV devices were subsequently obtained by adopting solvent engineering techniques [27]. These protocols involve casting from a mixed-solvent solution that forms intermediate complexes with the precursor slowing down the reaction to form perovskite crystals. The wet film is then treated with a non-polar solvent, in which the precursors are insoluble and thus precipitate out abruptly leading to the formation of a larger number of nuclei and improving the final film coverage. Solvent engineering techniques have helped to effectively separate the film formation step from perovskite crystallization. Another alternative approach with the same aim has led to the development of the two step or sequential deposition technique [28]. This method involves depositing first a thin layer of PbX_2 which is converted to perovskite by dipping or washing with a solution of MAX or by vapour phase treatment. This process is believed to involve the intercalation of MAX ions from the second solution into the interlayers spaces of the crystalline PbX_2.

1.4 Perovskite photovoltaics

Photovoltaic devices using hybrid perovskites as photoactive layers have developed rapidly in the last decade. Kojima et al. were the first to use hybrid perovskites as dyes in liquid electrolyte-based mesoscopic photovoltaic devices [5]. The stability as well as performance of these devices were enormously enhanced by the work of Kim et al. in replacing the liquid electrolyte with a solid state hole transport material [29]. Initially all devices were fabricated using a mesoscopic architecture as shown in figure 2. In this architecture perovskite served as absorber layer with the transport layers being mainly responsible for charge carrier transport and their interfaces with the perovskite aiding in charge carrier separation. However, two key studies showed hybrid perovskites were not only efficient absorbers but also had balanced ambipolar charge transport properties [30][31]. Based on these developments, planar perovskite configurations consisting of solid absorber layers sandwiched between p and n type charge selective films have been fabricated. By changing the perovskite compositions, improving deposition techniques for better morphology and by optimizing the Hole Transporting Material (HTM) layer photovoltaic devices with PCE of 22.1% have been obtained [3].

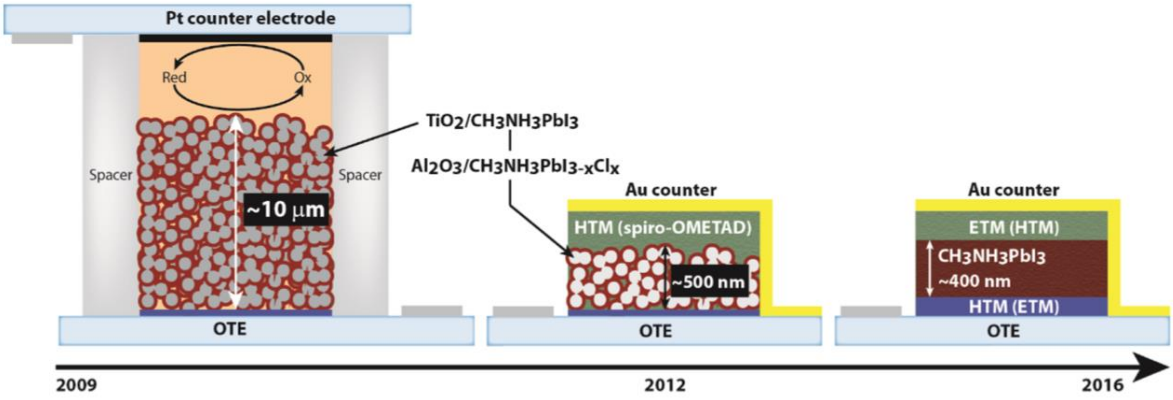

Figure 2: Perovskite solar cell architecture [32].

1.5 Techniques used in study

Non stoichiometric ratios of methylammonium and lead salts has been shown to improve the size of the crystalline domains [30]. The excess organic component however usually requires additional thermal treatment if lead iodide is used as lead precursor. In this study, the protocol developed by Zhang et al. has been adopted [33]. A non halide lead source such as lead acetate or $PbAc_2$ ($Pb(CH_3COO)_2$) helps accelerate the crystal growth kinetics because of the facile removal of CH_3NH_3Ac. This has also been quantified with the observation of lowest activation energies for the precursor-to-perovskite transition in the case of non halide lead salts followed closely by lead chloride and the highest for lead iodide [34]. The perovskite formation mechanism from these non-halide lead sources is hypothesized to proceed via displacement of anions between the two precursors to first form sheet like PbI_2 into which the remaining CH_3NH_3I intercalate as follows [35] [36]:

$$PbAc_2 + 3CH_3NH_3I \rightarrow PbI_2 + 2CH_3NH_3Ac + CH_3NH_3I \rightarrow CH_3NH_3PbI_3$$

The intermediate PbI_2 crystallizes in a rhombohedral structure which consists of layers of face sharing, distorted, octahedra which are held together by weak van der Waals forces [37]. In the case for lead free compositions, it has been suggested that precursors having a similar layered rhombohedral structure will allow direct intercalation of methylammonium iodide [38].

Furthermore, if the metal cation shows a 6-fold coordination with the halide in the precursor compound, it will have to undergo minimal reorganization and subsequently require lower activation energy for the perovksite to form. In this study based on these criteria and their solubility in anhydrous N,N-dimethylformamide $CoBr_2$, $FeBr_2$ and $MnCl_2$ were chosen for the mixed metal perovskite compositions.

It has also been found that the bimolecular charge recombination rate extracted for mixed halide (I-Cl) perovskite is an order of magnitude lower than for triodide materials [15]. Subsequently, the same study calculated charge carrier diffusion lengths that are a factor four larger for these mixed halide perovskite compositions. The role of chlorine has been controversial with studies claiming it acts as a dopant [39] or has a templating effect that leads to the crystallization of less disordered films [40]. However, what has been clear from numerous studies is that the amount of chlorine incorporated in the final film is minimal with the majority of the anion usually facilitating the release of excess organic ions [34].

1.6 Research Areas

Besides the exceptional optoelectronic properties and easy processability, hybrid perovskites have two main limitations. One is the presence of lead in high performing compositions and the other is the chemical instability under ambient conditions. In regards to the stability, great strides have been made in the last few years, moving away from volatile methylammonium and using mixed A site cations containing formamidinium that have greater thermal stability [41]. Furthermore, very recently nanocomposites of different perovskites (2D/3D) obtained using different sized A site cations were also developed that appear to couple the optimum electronic transport properties with the moisture stability offered by monolayer of 2D perovskite at the interface [42]. This unique structure was incorporated in HTM free PV devices that were stable up to 10000 hours in ambient atmosphere and temperature cycling.

However, the issue of toxicity and water solubility of carcinogenic lead and its halide salts [43] has raised questions regarding its use for devices as well as their end of life recycling. It is the focus of numerous research groups and also this study to contribute to the ongoing research effort to identify a non toxic replacement of lead while maintaining optimum optoelectronic properties. To date, substitution of lead is being attempted via two ways; homovalent and heterovalent substitution. Both these approaches have been particularly aided by the easy applicability of semi-empirical geometrical parameters which are elaborated upon in chapter 2. The first method has involved the search for elements with a stable oxidation of +2, while the second method is more complex and requires an equal proportion of mono and trivalent metal cations to balance out the total charge.

Homovalent replacement of lead has been predicted to be possible for a variety of isovalent cations belonging to group 14, alkaline earth metals and transition metals. However most of the experimental studies have focused on the fabrication of tin and germanium based perovskites. These have turned out to be highly unstable in ambient condition and tend to get oxidized easily. This leads to excessive hole density thus resulting in the film behaving as a p-type semiconductor with metal like conductivity. Hybrid germanium perovskite based solar cell were fabricated in 2015 [44] with PCE of 0.20%, but since then no significant improvements have been observed with these compositions. However, in the case of tin there have been significant developments with regards to minimization of the background charge carrier density by optimizing the growth condition. With the help of solvent engineering and a SnF_2-pyrazine additive, formamidinium tin triodide ($FASnI_3$) based PV devices have been fabricated

showing up to 6.22% PCE [45]. Another alternative research line has involved partially replacing lead with other divalent metal cations. Fabricating of (Pb-Sn) perovskites led to the observation of an unexpected anomalous band gap trend [24] in this series of perovskites. This has been employed to obtain perovskites with low band gaps of ~1.2eV and PV devices with PCE upto 17.01% PCE [46]. However, despite the improvements, it has been recently studied that the Sn based perovskites can be even more toxic than Pb [47]. The easy oxidation of Sn (II) to Sn (IV) caused a reaction with the organism resulting in the release of hydroiodic acid that caused significant harm.

1.7 Objectives and Outline

Looking beyond tin and germanium, alternative candidates from alkaline earth and transition metal groups are attracting attention due to their stable divalent oxidation states and compatibility with solution processing. Density Functional Theory (DFT) calculations have found a series of compounds that are predicted to show absorption onsets in the visible region, direct band gaps, dynamically stable perovskite structures [48], as well as reasonably low carrier effective masses [49]. Due to their different ionic sizes compared to lead, they are being incorporated by the partial replacement of lead to attempt the fabrication of mixed metal perovskite absorber layers. Experimental works have been performed to study partial substitution of Pb in perovskite thin films with Sr, Cd, Ca, Hg, Cu, Fe, Mn, Ni, Zn and Co [38] [50-59]. Though substitution of 25% of Pb with Co has been reportedly achieved [59], a more thorough theoretical as well as experimental investigation has been carried out for replacing Pb with Sr [38][55-57]. As previously mentioned in section 1.5, the different crystal structures of the various metal halide precursors appear to play a key role in the solution processability of these perovskites [38]. The layered structure of $SrCl_2$ which crystallizes in a rhombohedral structure has allowed replacement of up to 10% of the Pb to form mixed metal perovskites. While SrI_2, which crystallizes in an orthorhombic structure, has been found to only dope the lead based perovskite in small amounts of 2-5 % possibly due to its more closed and interconnected network structure. Furthermore, it has been found that the incorporation of dopants are made easier when they have a preexisting bond with the desired anion [60][61].

Building on these findings, in this thesis we focus on applying a similar reasoning to attempt substitution of higher amounts of lead with other transition metals and test the suitability of the halide salt for possible integration into the perovskite structure.

Firstly, in chapter 2, geometrical parameters such as the Goldschmidt tolerance factor and the octahedral factor are elaborated upon and applied to test the suitability of the perovskite structure based on three transition metals (Co, Mn, Fe). Furthermore, the theoretical upper limit of mixing Mn with Pb is obtained. Moving on to the experimental results in section 5.1 a reproducible solution process is adopted for depositing high quality Pb-only perovskite thin films and subsequently it's structural and optoelectronic properties are characterized. Furthermore, the recipe is adapted to study the suitability of this method to incorporate the metal cation, in this case only Pb, from two different metal precursor salts. Next in the section 5.2 we proceed to this study's main focus of partially substituting Pb with other selected stable divalent metal cations. After selecting Mn as a suitable candidate, in the section 5.3 increasing amounts of Pb is replaced to experimentally test the perovskite structure's tolerance for such metal-mixing and to compare with theoretical predictions of chapter 2. The section 5.4 focuses on the experiments designed to identify the possible origins of the non-perovskite crystalline structure also being formed and to study the effect of thermal annealing for longer times on the same. In section 5.5 the other precursor compounds are varied to calibrate the growth

conditions for the selected Pb-Mn perovskite composition. Next, in section 5.6 compact thin films of the final perovskite recipe are deposited on PEDOT:PSS, a commonly used HTM, to gain a better understanding of elemental composition and their distribution. Finally, in section 5.7 photovoltaic devices in the p-i-n architecture were fabricated as a concept to test the initial suitability of these mixed metal (Pb:Mn) perovskites.

A variety of tools are used to characterize the thin films fabricated for this thesis. XRD is used to confirm the presence of perovskite and residual crystalline materials. EDX and XPS are used to study the chemical composition of the films. Morphology of the films were observed with Secondary Electron images while the distribution of elements and subsequently phase homogeneity were qualitatively studied using Backscattered Electron (BSE) imaging. Optical properties were studied using UV-VIS absorption and PL spectroscopy and the electronic properties were probed with TRMC technique.

Geometrical Parameters

2.1 Tolerance and Octahedral factor

The perovskite structure is known for its compositional flexibility leading to the large number of known and reported compounds. However most of these perovskites are distorted and do not have the ideal cubic structure [62]. In 1926, Goldschmidt formulated a geometrical parameter, tolerance factor, to evaluate the ionic sizes that a cubic perovskite structure can still accommodate without a different structure forming instead. This can be more easily understood by looking at the perovskite unit cell as shown in figure 3.

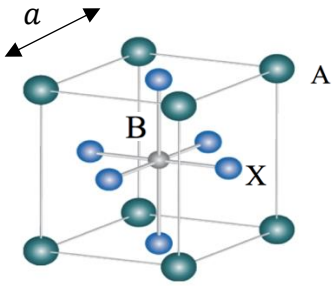

Figure 3: Perovskite unit cell with metal cation (B) at the centre, halide anions (X) at the face centres and organic cations (A) at the edges [62].

If the above structure is considered to be formed by densely packed spheres, the X site anions separate both the A site and B site cations. The lattice constant (a) is determined by the sum of the ionic diameters of the the B site cation and the X site anion. It can also be derived by the diagonal of the plane containing the A site cations and X site anions. This gives the simple relationship [62]:

$$a = 2r_B + 2r_X = \frac{(2r_A + 2r_X)}{\sqrt{2}}$$

Ratio of the two expressions is called the Goldschmidt's tolerance factor (t) and is defined below [64]. It allows the determination of the distortion in the structure and in turn the suitability of the various ions for the perovskite structure as elaborated on in table 1. However, these tolerance ranges are not strictly rigid and exceptions have been found to occur [65].

$$t = \frac{r_A + r_X}{\sqrt{2}(r_B + r_X)}$$

Table 1: Tolerance factor physical meaning.

Tolerance factor	Effect
$t > 1$	Size of A site cation too large to fit inside cavity
$0.9 \leq t \leq 1$	Cubic perovskite structure
$0.80 \leq t \leq 0.89$	Distorted cubic perovskite structure
$t < 0.8$	Size of A site cation too small

This semi-empirical geometrical parameter, combining ideas of dense packing of ions and the early estimates of ionic radii, has been successfully applied to various oxide perovskites. Recently, with the advent of the new field of metal halide perovskites it has been gaining significant attention to help explain the phase stabilization of perovskites as well as in predicting the formation of new compounds. However, since the A site cation is now occupied by a non spherical organic cation, in this study we use an effective radius as calculated by Cheeham et al. [66]:

$$r_{Aeff} = r_{mass} + r_{ion}$$

Where, r_{mass} is the distance between the centre of mass of the molecule and the atom with the largest distance to the centre of mass and r_{ion} is the ionic radius of this atom.

Another recent study has noted that the previously used Shannon radii for the B site metal ions are calculated for oxide and fluoride compounds. However, hybrid perovskite compositions, to date, that have been found applicable for optoelectronic applications are based on the heavier halides (I/Br/Cl). These heavier halides have lower electronegativity resulting in a greater degree of covalency in the metal-anion (B-X) bond which in turn shortens the bond. Travis et al. [67] took this shorter bond into account by modifying the B site cation radii while keeping the anion radius of the halide at its standard Shannon value.

Besides the tolerance factor, another geometrical parameter known as the Octahedral factor (μ) has been increasingly applied to determine the formability of perovskite strucutres. It is based on the size appropriateness of the B site cation to allow successful coordination with 6 anions and is formulated as [65]:

$$\mu = \frac{r_B}{r_X}$$

A lower threshold of 0.41 for this factor has been found in the case of inorganic perovskites, below which all known compositions of ABI_3 adopt non perovskite structures.

Table 2: Radii of A site organic cation used in this thesis.

+1	Effective radii (Å)
Methylammonium ion (MA^+)	2.16

Table 3: Radii of B site metal cation used in this thesis.

+2(VI)	Shannon (ionic)	Modified Radius		
		M-I	M-Br	M-Cl
Pb^{2+}	1.19	1.03	0.98	0.99
Co^{2+}	0.745	0.745	0.745	0.745
Mn^{2+}	0.83	0.72	0.72	0.73
Fe^{2+}	0.78	0.68	0.68	0.67

Table 4: Radii of X site halide anion used in this thesis.

-1 (VI)	Shannon Radius
I^-	2.2
Br^-	1.96
Cl^-	1.85

The two geometrical parameters are initially applied to study the formability of the perovskite structure using three metal cations; Co, Mn and Fe that have recently shown promise as suitable lead substitutes. Focussing on single metal perovskites using the ionic radii in table 2-4, it was observed that the compounds containing the three selected metal cations lie outside the region of formability of the perovskite structure as shown in figure 4 by the dotted lines and shaded region. This instability is primarily due to their smaller +2 ion size compared to Pb, which is even more exaggerated by the shorter bonds with the halides and which hinders the formation of the BX_6 octahedra. However, it is noticeable that the compounds incorporating the smaller chlorine ion shows some promise, especially with an alternate smaller A site organic cation to bring the tolerance factor values within suitable ranges.

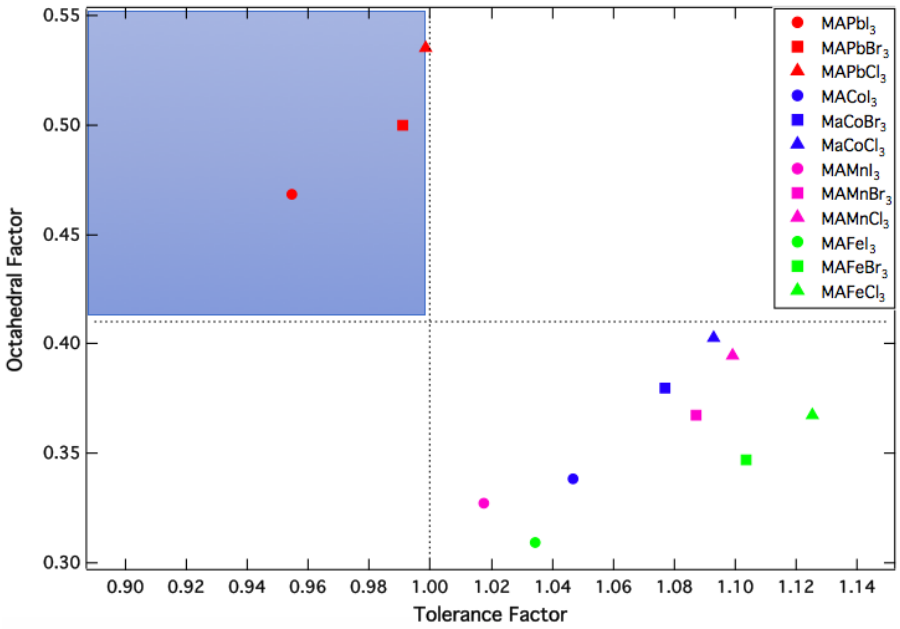

Figure 4: Structural map of ABX_3 compounds.

However, in this study we focus on the effect of alternative B site metal cations, being inspired by the tolerance factor tuning of the A site cation to successfully stabilize the cubic perovskite structure of formadinium lead triiodide ($FAPbI_3$) [68]. Partial replacement of the the larger Pb ion with a smaller Mn ion was explored to obtain an optimum tolerance and octahedral factor. With increasing Pb replacement, the atomic ratio weighted average of the two different metal cation sizes is used to estimate an effective cation size:

$$r_{B,eff} = xr_{Pb} + (1 - x)r_{Mn}$$

where, x is the molar fraction of Pb in the perovskite structure. As seen from figure 5a and 5b, up to 40% replacement of Pb^{2+} with Mn^{2+} should be theoretically possible while still maintaining the perovskite structure.

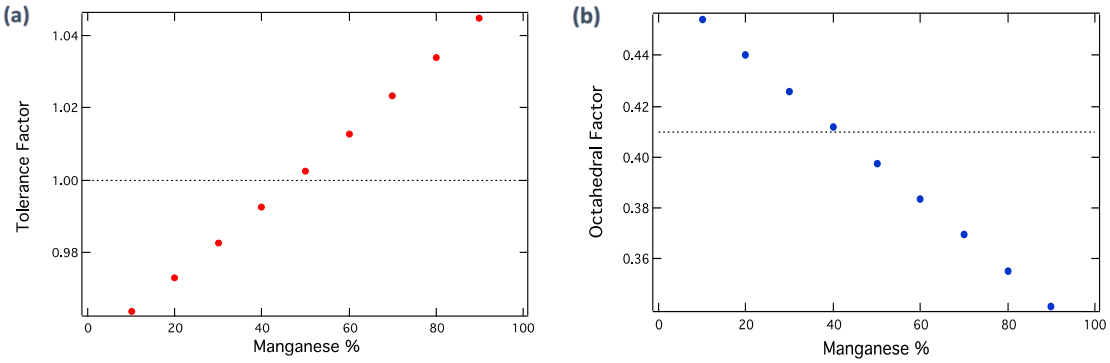

Figure 5: Geometrical parameters for mixed Pb:Mn compounds (a) Effective tolerance factor (b) Effective octahedral factor.

Characterization Techniques

3.1 X-ray Diffraction (XRD)

Diffraction is observed when electromagnetic radiation is directed on periodic structures with geometrical variations on the length scale of the wavelength of the radiation. Since interatomic distances in crystals are about 0.15–0.4 nm, they are comparable to the wavelengths of x-rays having photon energies between 3 and 8 keV [69]. Phenomena such as constructive and destructive interference become observable when such crystalline structures are exposed to x-rays.

2.1.1 Equipment Setup

X-rays in research labs are primarily generated in a sealed tube consisting of a stationary anode coupled with a cathode placed inside a container sealed under high vacuum as shown in figure 6. High energy electrons generated by the cathode, usually a heated tungsten filament, are accelerated towards the metal anode by high electrostatic potentials (30 to 60kV) [70]. On impact the metal target expels electrons from its lower energy levels leaving a vacancy. Intense characteristic X-rays are subsequently emitted from the transition of upper level electrons to fill up the vacancies. However, nearly all of the kinetic energy of the primary electron beam is converted into heat and the anode thus needs constant cooling. The X-rays exit the tube through appropriately shaped beryllium windows allowing them to be focussed for diffraction studies. Copper and cobalt are commonly used anode sources emitting x-rays with characteristic wavelengths of 1.54 and and 1.79 Å respectively.

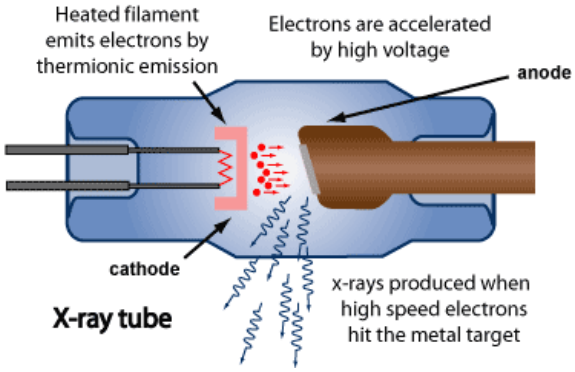

Figure 6: X-ray generating tube [70].

2.1.2 Working Principle

Electrons or the periodic electron density of atoms in a crystal are the primary scattering centres for x-rays. While the nuclei and the electrostatic potential can interact in a similar manner with incoming neutrons and electrons respectively. Only the elastic Thomson scattering is useful for structural investigations since the wavelength of the x-rays is conserved in contrast to the inelastic scattering processes [69]. On getting excited, the electrons in the material oscillates like a hertz dipole at the frequency of the incoming beam, thereby becoming a source for dipole radiation. The scattered waves interact by constructive interference only in specific directions as shown schematically in figure 7 that depend on the crystal structure and is formulated by the Braggs Law:

$$n\lambda = 2dsin\theta$$

where, n is the order of reflection, λ is the wavelength of radiation used, d is the interplanar distance and θ corresponds to the angle between detector and sample. For the most commonly used Bragg-Brentano geometry, both the radiation source and detector move at the same time, and the scattered intensity is plotted as a function of 2θ.

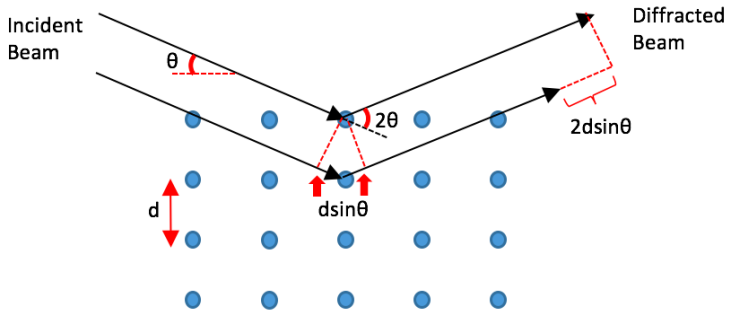

Figure 7: Schematic illustration of Braggs Law.

The position, intensity and shape of the XRD Bragg peaks can be analyzed to obtain various information listed in table 5 [70].

Table 5: Information obtained from powder diffraction pattern.

Pattern component	Crystal structure	Specimen property
Peak position	Unit cell parameters (a, b, c, α, β, γ)	Absorption, Macro strain
Peak intensity	Atomic parameters (x, y, z)	Preferred orientation, Absorption, Porosity
Peak shape	Crystallinity, Disorder, Defects	Grain size, Micro strain

3.2 X-ray Photoelectron Spectroscopy (XPS)

XPS is a powerful surface analysis tool to study physical and chemical phenomena at the surface of a wide range of materials from metals to biomaterials. XPS works on the principle of photoelectric effect in which soft X-rays are used as the photon exciting source. Typical sources include the Mg Kα (1.25 keV) and Al Kα (1.48 keV) that are emitted in a relatively sharp peak of ~1eV thus providing a clean spectrum for analysis purposes [72].

3.2.1 Experimental Setup

X-rays are produced at the Mg/Al anode by bombardment of electrons created at a filament. The X-ray photons are then directed on to the sample, which produces photoelectrons that are detected after analysis in the electron energy analyser as indicated in the figure 8 [72]. In the commonly used electrostatic analyser a potential is applied across two concentric plates that produces different deflections in the electron paths.

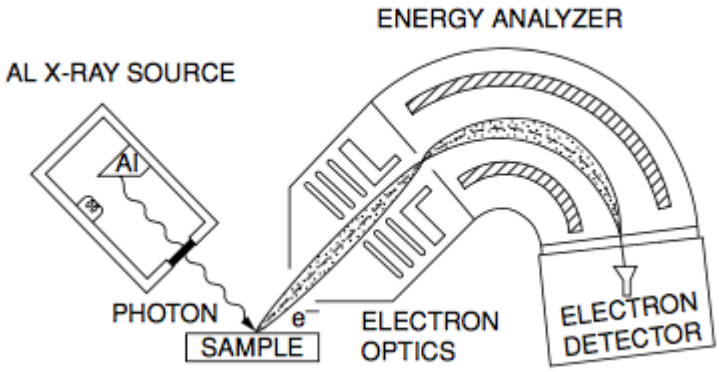

Figure 8: Experimental setup for XPS [72].

3.2.2 Basic Principle

The basic process of interest involves absorption of a monoenergetic x-ray photon of known energy and subsequently the ejection of an electron, the photoelectron, whose kinetic energy is measured. Comparison of the measured energy to a standard reference, the spectrometer work function, can be related to the binding energy of the photoelectron in the target atom. This process is schematically shown in figure 9.

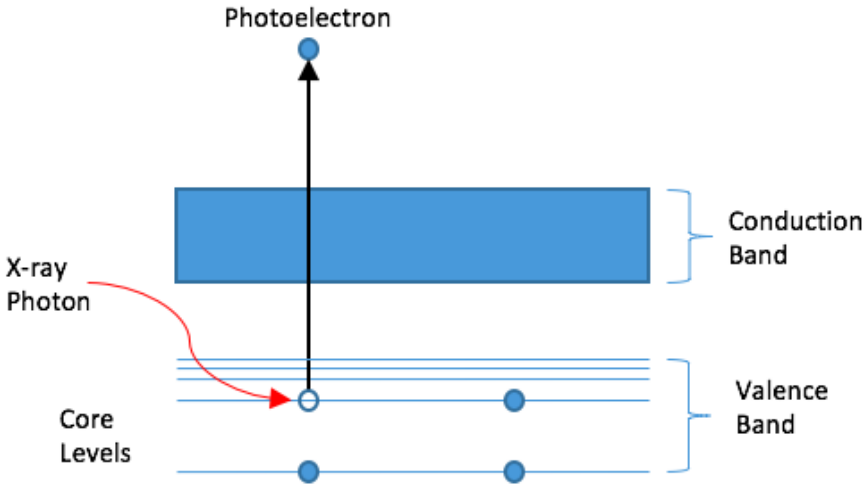

Figure 9: Inner shell electron being emitted by excitation from an X-ray photon.

By conservation of energy it is given that:

$$E_{Photon} = E_k + E_B$$

Where E_{Photon} is the energy of the x-ray photon, E_K is the measured kinetic energy of the ejected electron and the E_B is the characteristic binding energy which is calculated.

These binding energies are characteristic for specific shells of different atoms and can be used for elemental identification provided the electrons don't suffer energy loss while leaving the sample. Even though path length of x-rays is of the order of micrometers, the inelastic mean free path of the ejected electrons is only a few angstroms. Furthermore, the electrons can undergo kinetic energy loss due to a variety of reasons such as plasmon and phonon excitations

and the emission of Auger electrons or fluorescent x-ray photons. The distance that electrons can travel within the sample without suffering any energy loss is limited to a few monolayers beneath the surface giving the XPS a surface sensitivity of ~10nm.

2.2.3 Analysis

A typical XPS spectrum is shown in figure 10 where the number of ejected electrons is plotted against the binding energy. It consists of sharp peaks with extended long tails with the former corresponding to energies of characteristic electrons while the latter correspond to electrons that have undergone energy loss on their outward path. Elemental composition can be found by comparing the spectrum to known databases. Binding energy of core electrons is dependent on the species to which the atom is bonded, this can result in a "chemical shift" of the peak due to various reasons such as oxidation states, electronegativity, molecular environment, lattice sites etc. [72]. Depth profiles of elemental composition can also be observed by removing surface layers via sputtering using an inert gas such as Argon. A new XPS analysis is carried out after each etching step to give information for a series of depths.

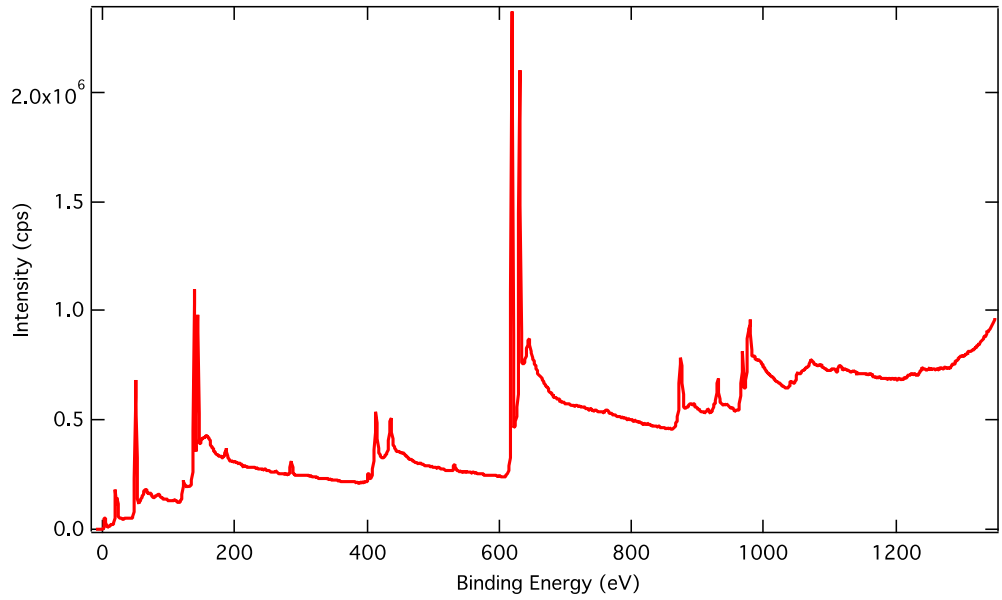

Figure 10: XPS spectra for a $MAPbI_3$ film.

3.3 Scanning Electron Microscopy (SEM)

SEM uses a focused beam of high-energy electrons to generate a variety of signals at the surface of solid materials as shown in figure 11. The signals generated from electron-sample interactions reveal information about the sample such as external morphology, composition, and crystalline structure and orientation of the materials.

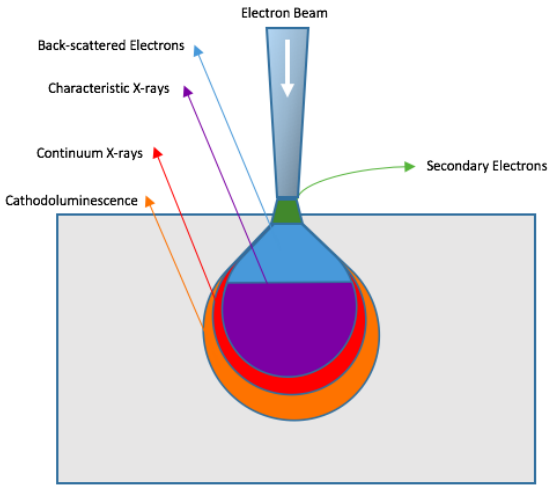

Figure 11: Signals emitted from different parts of the interaction volume.

3.3.1 Experimental Setup

The electron beam in an SEM is generated from a tungsten filament, LaB_6 or Schottky emitter [73]. It has a typical diameter of 10 nm which determines the minimum resolution of an SEM image. This beam after entering the specimen chamber, strikes the specimen at a single location. Within this interaction volume, as shown in figure 11, both elastic and inelastic scattering may take place generating various signals from backscattered electrons, secondary electrons, characteristic and continuum x-rays, and cathodoluminescent radiation that can be detected as shown in figure 12. The magnitude of these signals are then measured with the respective detectors, allowing the determination of certain properties at that single location. The beam can then be moved across the sample in the X and Y direction via deflection by electro magnetic coils.

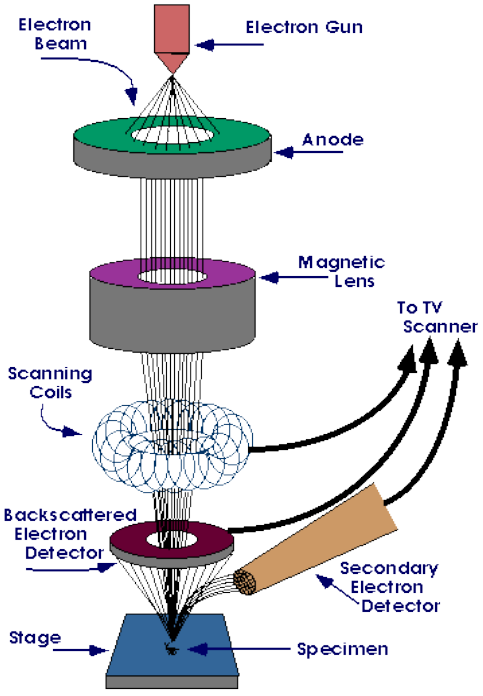

Figure 12: Schematic representation of the experimental setup for SEM [74].

3.3.2 Scattering of electrons

In an SEM the primary electron beam undergoes both elastic as well inelastic scattering, with the former interaction due to collisions with the atomic nuclei while the latter due to interaction with the atomic electrons. In both situations most interactions have deflections lower than 90° which results in forward inelastic scattering of the primary beam coupled with subsequent reduction of its kinetic energy. However, a small fraction of the primary electrons can be elastically deflected at angles larger than 90°, allowing them to leave the sample without a significant loss of kinetic energy. The volume of sample containing these scattered electrons is called the interaction volume and has been shown previously in figure 11.

3.3.3 Secondary Electron Images

Secondary electrons are produced as a result of inelastic interactions between energetic primary beam electrons and weakly bound valence or conduction band atomic electrons. A small fraction of the energy of the primary electrons is used to break the secondary electron away from the atom and that secondary electron is emitted with a non-zero kinetic energy in the order of 100 eV due to which they quickly come to rest within 1-2 nm [75]. Only the secondary electrons created near the surface are close enough to escape into the vacuum. Secondary electron images are thus mainly a property of the surface structure and display topographical contrast.

3.3.4 Backscattered Electron Images

Elastic scattering involves only a small energy loss, consequently the back scattered electrons escape from the sample with energies similar or just below that of the primary beam. This allows the secondary and backscattered electrons to be easily distinguished based on their kinetic energy. This higher energy also allows back scattered electron signal to come from much deeper in the sample as shown in figure 11. For primary beam energies above 3 kV, this depth is 10-100 nm [74]. The cross-section for high-angle elastic scattering is proportional to Z^2, where Z is the atomic number, thus allowing significant atomic-number contrast in back scattered imaging mode. While secondary electron images just reflect the surface topography, back scattered images show contrast due to variations in chemical composition of a specimen.

3.3.5 Energy Dispersive X-ray spectroscopy

When primary electrons inelastically collide with an inner-shell electron and lead to its ejection the atom is left in an excited state. Subsequent relaxation results in an electron transition from an outer shell to fill the vacancy in the inner shell. This transition involves a release of energy either in in the form of x-rays or an ejected (Auger) electron. The energy of the emitted x-rays is characteristic of different atomic elements as they are related to differences of energy between sharply defined levels of the atom. Furthermore, they are of the order of 100-1000 eV that allows them to escape from 1-2 µm inside the sample. Elemental mapping can also be performed when these characteristic x-ray signals are used to control the scanned-image intensity [75].

3.4 UV-Vis Absorption Spectroscopy

When light impinges on matter, it can be scattered (elastically or inelastically), absorbed, or transmitted. These interactions depend on physical, chemical, and structural properties of the matter besides depending on the intensity and energy of the incoming photons [76]. Spectrophotometry is one of the most popular type of spectroscopies that measure the intensity of transmitted and reflected light.

3.4.1 Experimental Setup

In a spectrophotometer as shown schematically in figure 13, electromagnetic radiation is generated by a stable light source over both UV and visible ranges. This radiation is then split into specific wavelengths by a monochromator and is then allowed to pass through both the sample as well as a reference. Finally, a photodiode analyses the transmitted radiation intensity. Furthermore, the reflected light from each surface can also be collected using a specially designed mirror or integrating sphere [77].

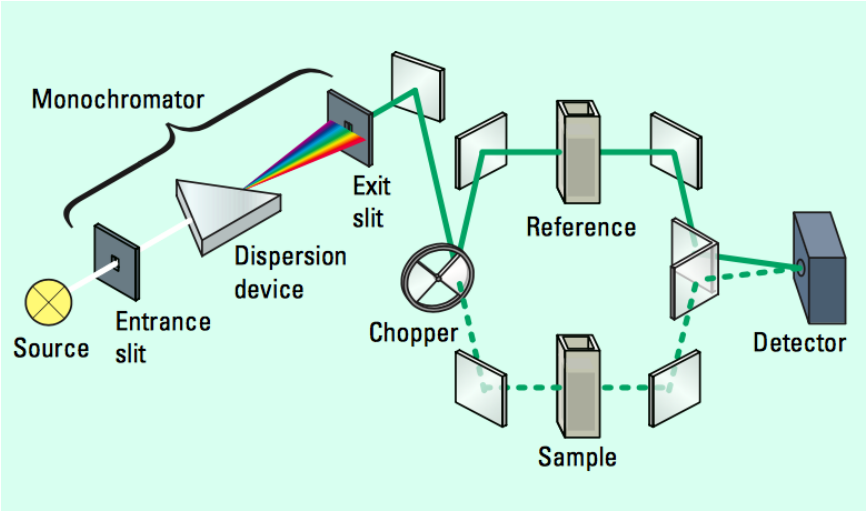

Figure 13: Schematic representation of experimental setup for absorption spectroscopy [78].

3.4.2 Basic Principle

Depending on the energy of the photons, different excitations are generated in the matter. Photons in the UV and visible region of the spectrum, are more likely to interact with the electrons of the outer shells promoting them to more energetic levels or create excitons, while infrared photons are more likely to interact with lattice and molecular vibrations and rotations, creating phonons [76]. The minimum energy needed to excite an electron from the valence band maximum to the conduction band minimum is the band gap energy of the material as shown in figure 14.

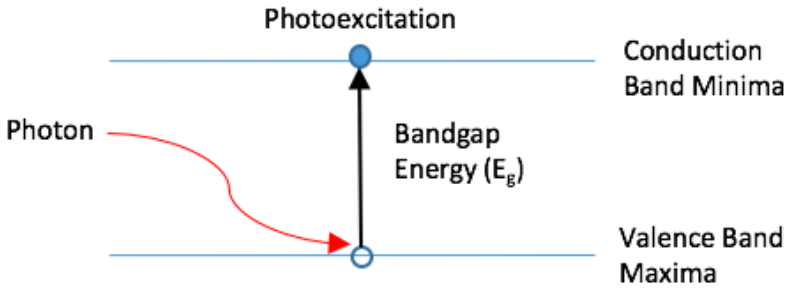

Figure 14: Excitation of electron by absorption of photon with energy more than E_g.

When light passes through a material and assuming there is no reflection, the amount of light absorbed is the difference between the incident radiation (I_o) and the transmitted radiation (I). This amount of light absorbed is expressed as either transmittance or absorbance. The Bouger-Lamber-Beer law forms the mathematical-physical basis for this measurement [76].

$$A_b = \log\left(\frac{I_O}{I}\right) = \log\left(\frac{100}{\%T}\right) = \alpha z$$

Where, A_b is the absorbance, T is the transmittance, α is the absorption coefficient and z is the path length. If the diffuse and specular reflected light is also collected using an integrating sphere [76], the absorptance of the material can be calculated as follows [80]:

$$A = 1 - (T + R)$$

where A is the absorptance, T is the transmittance and R is the absolute reflectance.

3.5 Photoluminescence (PL)

Photoluminescence is a non destructive technique for the analysis of semiconductors providing information on their electronic properties. It is particularly suited for the detection of shallow-level impurities and can also be applied to specific deep-level impurities as long as the recombination of the electron and hole is radiative.

3.5.1 Steady state Photoluminescence

Steady state photoluminescence consists of exciting the sample with a laser having energy larger than the band gap, generating electron-hole pairs which recombine by one of several mechanisms. The photons which are emitted by radiative recombination and are able to leave the sample are focussed onto either a dispersive or a Fourier transform spectrometer and then a detector as shown in figure 15 [81]. The sample can also be placed in a cryostat and cooled to temperatures near liquid helium. Low temperature measurements are desirable to minimize thermally activated non-radiative recombination processes and thermal line broadening.

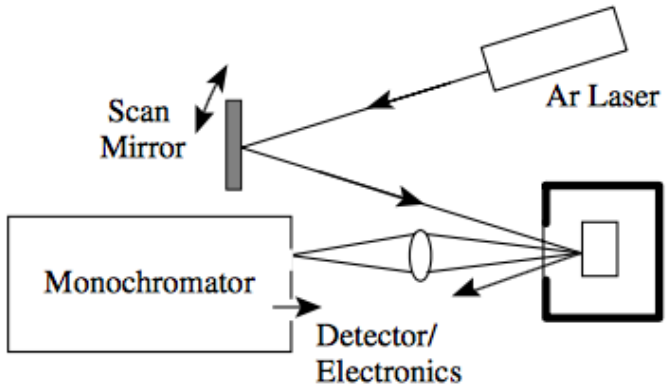

Figure 15: Schematic representation of the PL experimental setup [81].

Following the fundamental absorption process of a direct band gap material described previously, the carriers relax to the lowest excited level before dropping down to the ground state by emitting a photon as shown schematically in figure 16. Such radiative recombination can occur via different ways such as band-to-band transition, exciton collapse or from localized defect energy levels [82]. The emission spectrum shows a fingerprint sharp peak related to the band gap or defect energies. The intensity of the photoluminescence peak and its dependence on the level of photoexcitation and temperature is directly related to the dominant

recombination process with the peak width being a representative of the energy distribution of the PL emitting states.

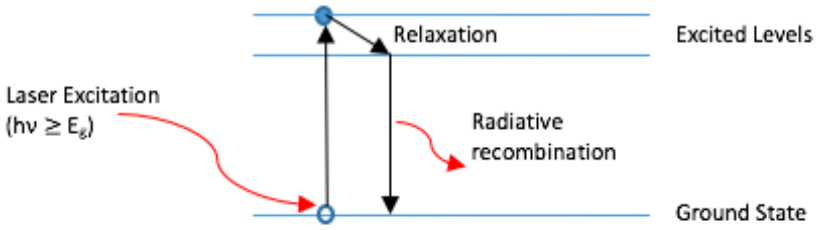

Figure 16: Emission of luminescent photon due to radiative recombination.

3.5.2 Time resolved Photoluminescence (TRPL)

Time resolved Photoluminescence (TRPL) is commonly carried out using Time Correlated Single Photon Counting (TCSPC) which is an effective method to probe the dynamics of the various recombination processes.

It is a digital counting technique that is based on the assumption that probability of detecting a single photon at a particular time t is proportional to the photoluminescence intensity obviating the need to measure it [83] [84]. Production of an excitation light pulse starts the timer and the detection of the first fluorescent photon from the sample stops it shown in figure 17. The emission process is probabilistic in nature and the difference in time between these two signals is output to a histogram, consisting of time bins with a width of Δt. All signals arriving within t+Δt go into a specific bin.

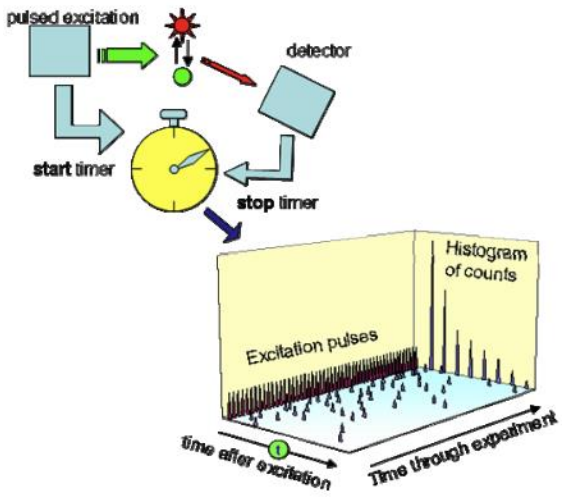

Figure 17: Schematic representation of experimental setup for TRPL using TCSPC [85].

3.6 Time resolved Microwave Conductivity

TRMC is an electrodeless AC technique to probe the photocarrier dynamics and carrier transport in weakly conducting, thin photoactive materials [86]. It is particularly suited for studying local charge carrier motion without the hindrance of domain boundaries or energetic barriers affecting the measured values [87]. Furthermore, being an electrode less technique

obviates the need for ohmic contacts and eliminates the effects due to the active layer – electrode interfaces.

3.6.1 Experimental Setup

TRMC is a pump probe technique, in which the sample is optically excited by a short laser pulse and the change in conductance is probed with monochromatic X-band microwaves (8-12 GHz) as shown in figure 18. The interaction of the electric field of the microwave radiation with the mobile charge carriers will result in a decrease of its amplitude and/or a change of its phase. Extent of the attenuation and the phase shift depends on the change in real and imaginary conductance.

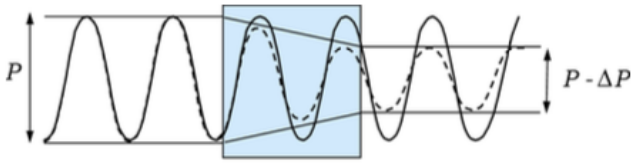

Figure 18: Attenuation of microwave radiation through a conducting medium [86].

The experimental setup primarily involves four parts as shown in figure 19. X-band microwaves with powers up to 100 mW are generated using a Gunn diode mounted in a tuneable resonant cavity. The visible range photoexcitation source is a 3-5 ns pulse of a Nd:YAG laser. Furthermore, incident light intensity on the sample can be tuned over several order of magnitude of fluence (10^{11} - 10^{15} photons/cm^2) using neutral density filters. In the reflection mode of operation, a circulator is needed which guides the waves into the sample and guides the reflected waves to the detector.

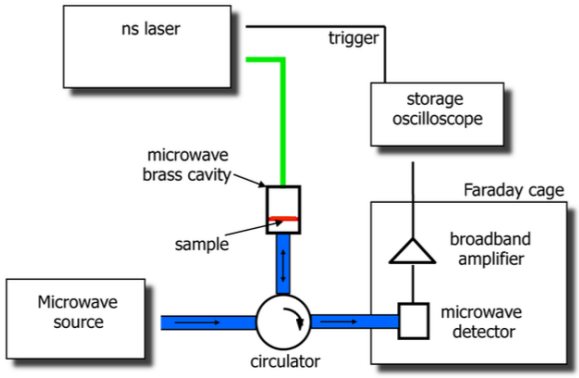

Figure 19: Schematic representation of the TRMC setup [86].

3.6.2 Analysis

Microwave measurements can be carried out in either an open cell or cavity. The cavity length matches with the length of one full oscillation of the resonant frequency of the x-band microwave. By placing the sample at the positon of the electric field maximum, the sensitivity of the instrument is optimized. The normalized change in microwave power (ΔP/P) absorbed by the sample can then be related to the change in photo-conductance (ΔG) by [86]:

$$\frac{\Delta P(t)}{P} = -K\Delta G(t)$$

where, K is the sensitivity factor of the cavity and depends on dimension of the cavity, quality of the cavity walls and the dielectric properties of the sample being measured.

The product of the photogeneration yield and the sum of the electron and hole motilities can be calculated from the maximum value of the photo-conductance:

$$\eta \sum \mu = \frac{\Delta G_{max}}{I_0 \beta e F_A}$$

Where, η is the photogeneration yield, *i. e.* the ratio between the number of the photogenerated free charge carriers and the number of incident photons, I_0 is the number of photons per unit are per pulse and F_A is the fraction of light absorbed by the sample at the excitation wavelength. From a trace of ΔG versus time as shown in figure 20, it can be observed that directly after excitation by a laser pulse, the value of ΔG increases to a maximum due to generation of free mobile charge carriers. Since no electrodes are present, decrease of the photo-conductance can be only due to recombination and/or trapping of the charge carriers, providing information also about the lifetime of photogenerated carriers.

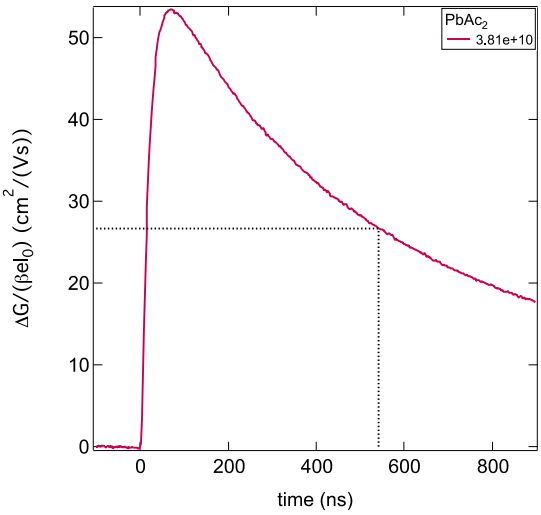

Figure 20: Photoconductance as a function of time for a $CH_3NH_3PbI_3$ film measured at a laser intensity of 3.81 * 10^{10} photons/cm^2.

Experimental Methods

4.1 Synthesis Methods

Hybrid perovskites in this master thesis were synthesized by solution based methods. Due to the unknown stability of mixed metal perovskites, they were synthesized and stored inside a nitrogen glovebox. All chemicals except methylammonium iodide were obtained from Sigma Aldrich.

4.1.1 Precursor Synthesis:

Methylammonium iodide was synthesized by reacting equimolar amounts of hydroiodic acid (HI) (57 wt% in water) with methylamine (CH_3NH_2) (33 wt %in ethanol) in an ice bath for two hours. The precipitate of the solution was collected by rotary evaporation at 50°C for 4 hours. This precipitate was then washed with diethyl ether by pump air filtration before being dried under vacuum for at least 24 hours.

4.1.2 Thin film deposition:

Precursors were weighted inside the glovebox and dissolved in anhydrous N,N-dimethylformamide (DMF). The solutions were then magnetically stirred on a hotplate for 20 minutes at 70°C to ensure complete dissolution of precursors following which they were allowed to cool down to room temperature before deposition. Quartz substrates were cleaned using O_2 plasma, to remove any organic contaminants as well as render the surface hydrophilic. FTO coated glass substrates required thorough ultrasonic solvent cleaning with surfactant, acetone and ethanol followed by 30 minutes of UV/Ozone treatment. Subsequently, spin coating of the perovksite solution was done using optimized process parameters to obtain a wet film on the substrates. Finally, a thermal treatment at 100°C was carried out for different specified times to remove the residual solvents, allow sublimation of byproducts, crystallize the perovskite as well as enable thin film growth.

For the standard reference, precursor solutions were prepared by mixing 3:1 (by moles) of CH_3NH_3I and $PbAc_2$ in anhydrous N,N-dimethylformamide. Subsequently, varying amounts of $PbAc_2$ were replaced with other metal salts such as $PbCl_2$, $CoBr_2$, $FeBr_2$ and $MnCl_2$. For the bilayer of perovskite/Hole Transport Material (HTM), FTO coated glass substrates were first coated by a water dispersion of PEDOT:PSS via spin casting through a 0.4µm filter. This was followed by thermal annealing at 120°C for 20 minutes before moving the samples in the glovebox for the deposition of the perovskite layer.

4.2 Sample preparation and experimental methods

4.2.1 X-ray Diffraction (XRD)

Perovskite thin films were prepared in a glovebox on quartz substrate following the procedure described in the synthesis methods. The sample was then placed in a custom shaped air tight dome inside the nitrogen glovebox so as to avoid contact with air.

X-ray diffraction measurements were performed using a Bruker D8 Advance diffractometer in the Bragg-Brentano Geometry. Monochromatic Cobalt Kα source with a wavelength (λ) of 1.7889 Å was operated at 40 kV and 40 mA. Experimental data were obtained for 2θ from 5 to 60° with a step size of 0.0196°, time per step of 0.2s and a divergence slit of 0.300 mm.

Furthermore, XRD patterns were subsequently compared to patterns from the ICSD database whenever available.

4.2.2 X-ray Photoelectron Spectroscopy (XPS)

For XPS measurements, perovskite thin films were deposited on PEDOT coated glass substrates as described in the synthesis methods. Sample was prepared inside the glovebox but briefly exposed to air while they were loaded into the instrument.

XPS measurements were performed with a Thermo Scientific K-Alpha X-ray Photoelectron Spectrometer (XPS) system, using a monochromatic Al Kα source emitting a 400 μm beam when operated at 12 kV and 3 mA. Wide scans were acquired at analyser pass energy of 200 eV, while narrow scans with higher resolution were performed at a pass energy of 50 eV. The analysis chamber pressure is maintained around 1×10^{-7} torr during data acquisition and the data was processed using Avantage software. The binding energy (BE) scale was internally referenced to the C 1s peak (284.8 eV).

4.2.3 Scanning Electron Microscopy (SEM)

Perovskite thin films were prepared in a glovebox on quartz substrate following the procedure described in the synthesis methods. The samples were mounted on a flat holder for top view images and on an inclined 45° holder for cross section imaging.

SEM images were taken with JEOL-JSM-610LA microscope using 10 kV voltage energy and 10 mm working distance for the top view images and 5 mm working distance for cross section images. Each sample was measured with various magnifications in the different imaging modes. Magnifications of x1000 and x3000 were used in secondary electron mode while x200 and x750 were adopted in backscatterd mode. Elemental compositions and map analysis images were obtained with EDX with primary electron voltage of 20 kV and magnifications around ×1000.

4.2.4 UV-Vis Absorption spectroscopy

Perovskite thin films were prepared in a glovebox on quartz substrates using the procedure described in the synthesis methods. The samples were then placed in a custom shaped metallic holder consisting of a window that allows light in and an o-ring lining so as to avoid contact with ambient air after its loaded and closed inside the glovebox.

The samples were measured with a PerkinElmer UV/VIS/NIR Lambda 1050S spectrometer containing 150mm Spectralon integrating sphere. InGaAs and PMT detectors were used for detection in the near infrared (NIR) and in the ultraviolet-visible (UV-VIS) spectra respectively. Lambda 1050S has Deuterium and Tungsten Halogen light sources. The perovskite thin films were measured between wavelengths of 250 and 900 nm.

4.2.5 Photoluminescence (PL)

Perovskite thin films were prepared in a glovebox on quartz substrates using the procedure described in the synthesis methods. The samples were then placed in the same custom shaped metallic holder used for absorption spectroscopy.

PL measurements were carried out using an Edinburgh LifeSpec spectrometer equipped with a Single-Photon counter. The perovskite films were excited at 405 nm with a picosecond pulsed diode laser. A neutral density filter was used to prevent light below wavelengths of 450 nm from reaching the detector. PL emission spectra for all the perovskite samples were obtained

between wavelengths of 650 and 900 nm. Pl lifetimes were tracked using TSPC method at the maximum emission wavelength.

4.2.6 Time Resolved Microwave Conductivity (TRMC)

Perovskite thin films were prepared in a glovebox on quartz substrates using the procedure described in the synthesis methods. Samples to be measured were loaded in the glovebox's N_2 atmosphere into a microwave cavity. This cell consists of a microwave waveguide that conducts the microwave to the sample and a grated window covered by quartz that allows the entry of the exciting optical signal.

Photoexcitation of the sample is achieved with a laser that emits pulses with a 3 ns full width half maximum at a tunable wavelength which was fixed in this thesis project to 450 nm. Microwaves with an alternating field with a frequency of approximately 8.4 GHz are used to probe the electronic properties of the sample.

Results and Discussions

5.1 Lead Only perovskite

Thin films of $MAPbI_3$ were first synthesized using a non halide lead source ($PbAc_2$) via the procedure developed by Zhang et al. [33] as described previously in the experimental methods. Furthermore, to check the viability of this processing method to incorporate the metal cation (Pb) from two separate metal salts, mixing lead precursors [88] [89] ($PbAc_2$+$PbCl_2$) was also attempted. Both the thin films were fabricated by spin coating and thermally annealed for 15 minutes at 100°C.

The structural characteristics of the $MAPbI_3$ from acetate source ($PbAc_2$) as well as from mixed source ($PbAc_2$+$PbCl_2$) were studied using XRD. Figure 21 shows the the pattern for $MAPbI_3$ obtained from lead acetate, while figure 22 shows $MAPbI_3$ obtained from the mixed lead sources. Both the thin films have the characteristic peaks of the tetragonal phase of the perovskite crystal, especially since the single source perovskite film's diffractogram contains the (211) peak which is inconsistent with the cubic phase [90]. The film fabricated using mixed lead sources shows stronger diffraction peaks for the (110) and the (220) lattice planes in line with previously published results that Cl incorporation favors preferential growth along (110) direction [88]. When the (110) reflection's full width half maxima are compared, as shown in Table 5.1, lead acetate films however show lower FWHM and larger crystallite sizes. In both the films there is residual unreacted PbI_2 which can be identified by its characteristic (001) reflection at 14.71º. Also noticeable is the lack of any peaks that could be attributed to the formation of $MAPbCl_3$ in the perovskite film derived from mixed lead sources, which is comparable with previously reported literature data [91].

Table 6: Full-width-half-maximum (FWHM) of the (110) facet and the calculated crystallite size using Scherrer equation.

Film	(110) Peak 2theta	FWHM	Crystallite Size (Å)
$PbAc_2$	16.461	0.081	1271
$PbAc_2$:$PbCl_2$ (4:1)	16.42	0.089	1170

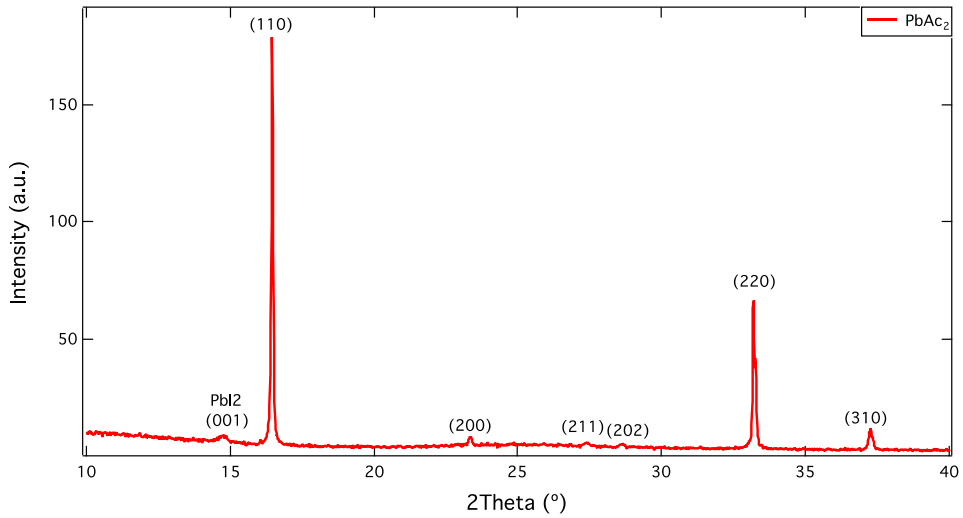

Figure 21: XRD diffractogram of perovskite from $PbAc_2$.

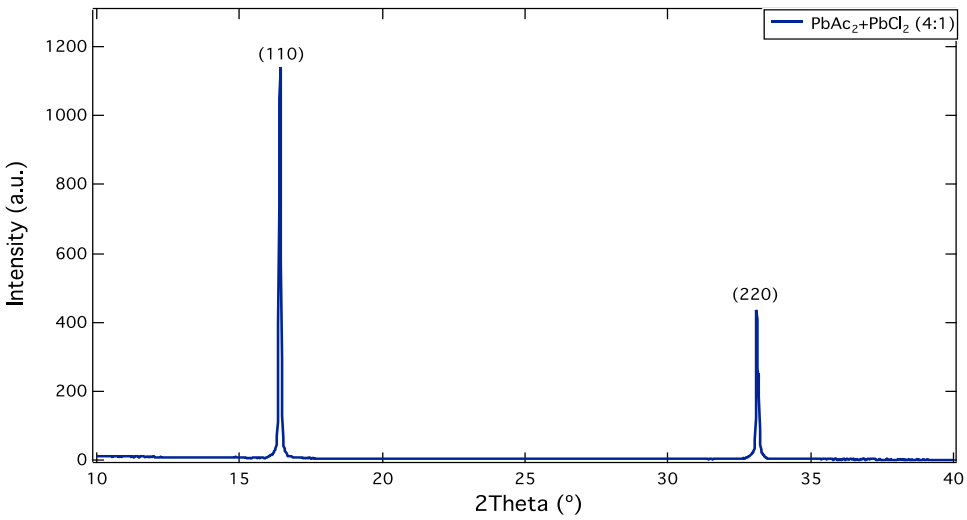

Figure 22: XRD diffractogram of perovskite from mixed lead source ($PbAc_2$ +$PbCl_2$).

Optical properties of the perovskite films obtained from single ($PbAc_2$) and mixed lead sources ($PbAc_2$+$PbCl_2$) were characterized by means of UV-Vis absorption and photoluminescence spectroscopy, as shown in figure 23 (a) and (b) respectively. It is observed that the overall absorption spectrum is similar over the visible region, with the film from mixed lead source showing slightly higher absorption from 550 to 780 nm. This can be due to either better crystallinity, improved surface coverage or thicker films as chlorine has been found to induce both vertical as well as lateral grain growth and reduction in pinhole area [88] [89]. Both the films show another absorption onset at around 505 nm which has been previously attributed to PbI_2 remaining in the film [92]. The PL emission peak is slightly enhanced and blue shifted by ~10 nm in the film obtained from mixed lead sources. This might be due to morphology effects or passivation of non-radiative defects due to the the presence of Cl or an increase in bandgap due to actual incorporation of Cl in perovskite structure [93]. However, in our case we can confirm that there is no change in the bandgap since there is no shift in the UV-VIS absorption onset.

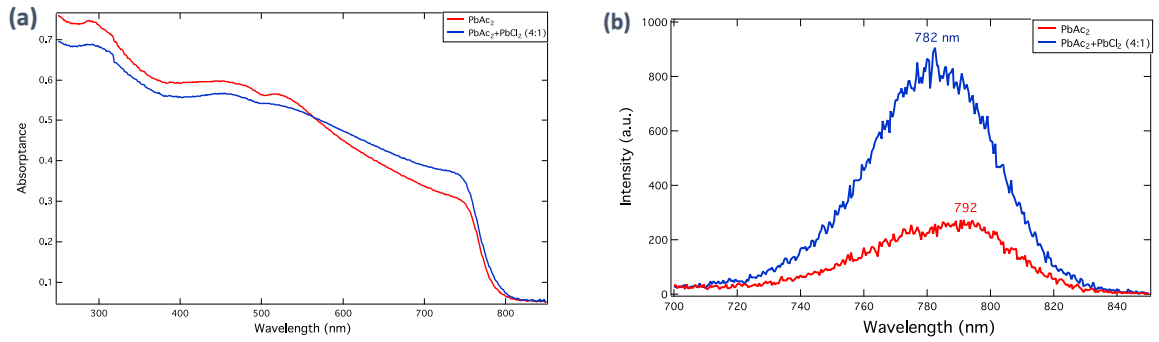

Figure 23: Optical properties of perovskite films from single ($PbAc_2$) and mixed lead sources ($PbAc_2$ +$PbCl_2$) (a) UV-Vis absorption spectra (b) PL emission spectra.

TRPL has also been measured as shown in figure 24. It is clearly observable that the film obtained using mixed lead sources has slower PL decays. Long PL lifetimes and charge carrier diffusion lengths have been shown for $MAPbI_3$ obtained by this method [94] and hypothesized to be due to possible doping effects of chlorine [39].

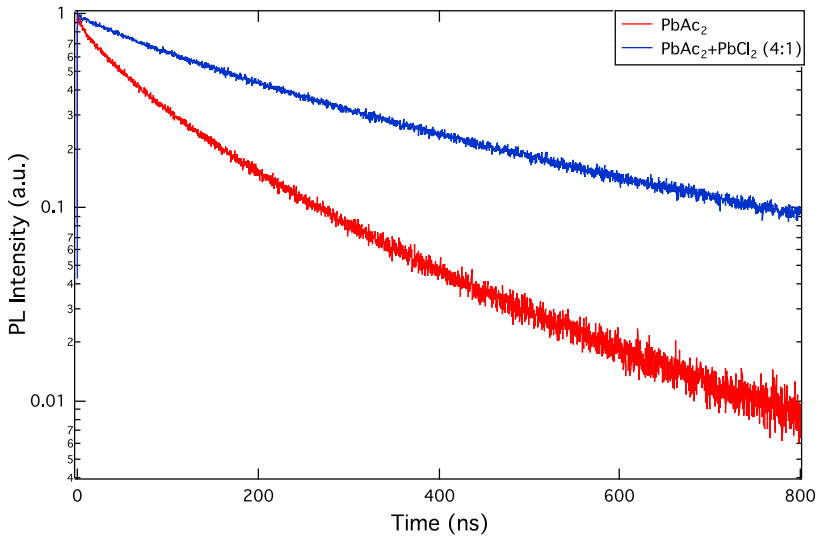

Figure 24: PL decay curves for perovskite films from single ($PbAc_2$) and mixed lead sources ($PbAc_2$ +$PbCl_2$).

Next, TRMC measurements were made to gain a better understanding of charge carrier dynamics in these two films. The films were excited at 450 nm using a pulsed laser whose fluence was varied between ~ $4*10^9$ to $4*10^{11}$ photons cm^{-2} per pulse and the traces of the photoconductance were plotted versus time as shown in figure 25 (a) and (b) for the single ($PbAc_2$) and mixed lead source ($PbAc_2$+$PbCl_2$) based perovskite respectively. In both the films the photoconductance ΔG is a similar function of time consisting of an initial rise, due to generation of mobile charge carriers, followed by a decay caused by a decrease of charge carrier concentration either due to trapping or recombination.

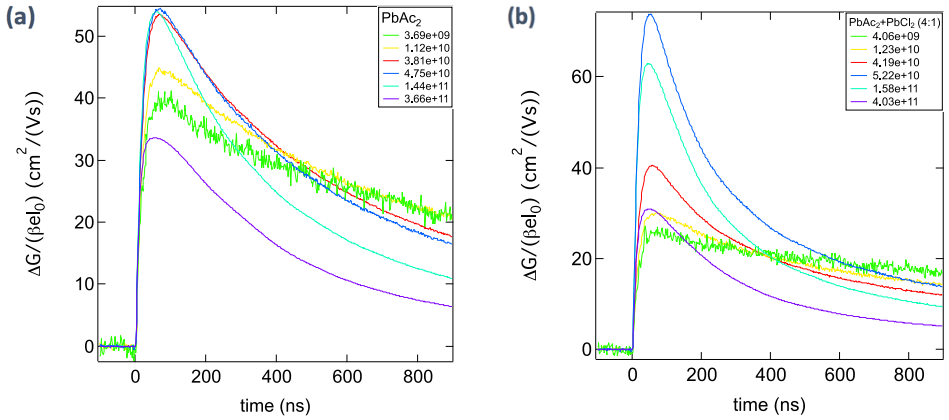

Figure 25: Photoconductance as a function of time for perovskite films (a) from single ($PbAc_2$) (b) from mixed lead sources ($PbAc_2$+$PbCl_2$).

The product of the yield of free charges and their mobilities is calculated from the maximum value of the photoconductance, and it is traced with respect to intensity of the laser pulse in figure 26 (a). It is observed that in both cases the peak signal initially increases with laser intensities before dropping. This is because at low charge carrier concentrations immobilization due to presence of traps dominates, and only when these are passivated do the charge carriers undergo second order recombination. The half lifetimes *i.e* time required for the signal to drop to half its value is plotted for the samples in figure 26 (b). It is observed that at high laser intensities, when the traps have been passivated and the charge carriers are primarily undergoing second order recombination during the pulse, the lifetime almost becomes constant.

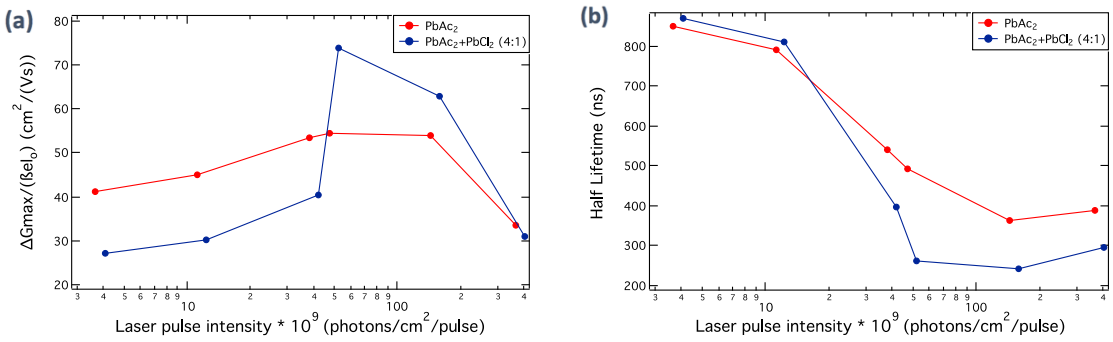

Figure 26: Electronic properties as a function of laser intensity of perovskite films obtained from single ($PbAc_2$) and from mixed lead sources ($PbAc_2$+$PbCl_2$) (a) Maximum value of photoconductance (b) Half lifetimes.

The morphology of the two films was studied using SEM in secondary electron imaging mode as shown in figure 27 (a) and (b). It is noticeable that the grain sizes of the perovskite film obtained from mixed lead sources are significantly larger but at the same time the coverage on quartz substrate coverage is lower due to the presence large interconnected pinholes. $PbAc_2$ was chosen as a suitable lead precursor as it allowed easy crystallization of high quality $MAPbI_3$ with short annealing times of 15 minutes and furthermore it showed suitable tolerance of a secondary metal salt precursor.

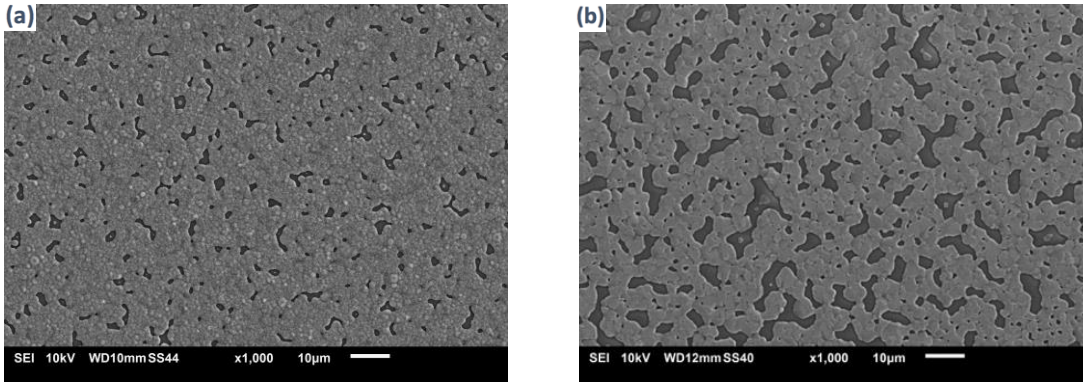

Figure 27: Secondary electron images of perovskite films obtained from (a) $PbAc_2$ precursor and (b) from mixed lead sources ($PbAc_2$+$PbCl_2$).

5.2 Initial Screening of mixed metal perovskite

Perovskite thin films were synthesized by substituting 20 molar % of lead acetate with the selected divalent metal precursors ($CoBr_2$, $FeBr_2$, $MnCl_2$) and TRMC measurements were obtained as shown in figure 28 (a) (b) and (c). The thin films were fabricated by spin coating, keeping deposition parameters the same as before, and thermally annealed for 15 minutes at 100°C.

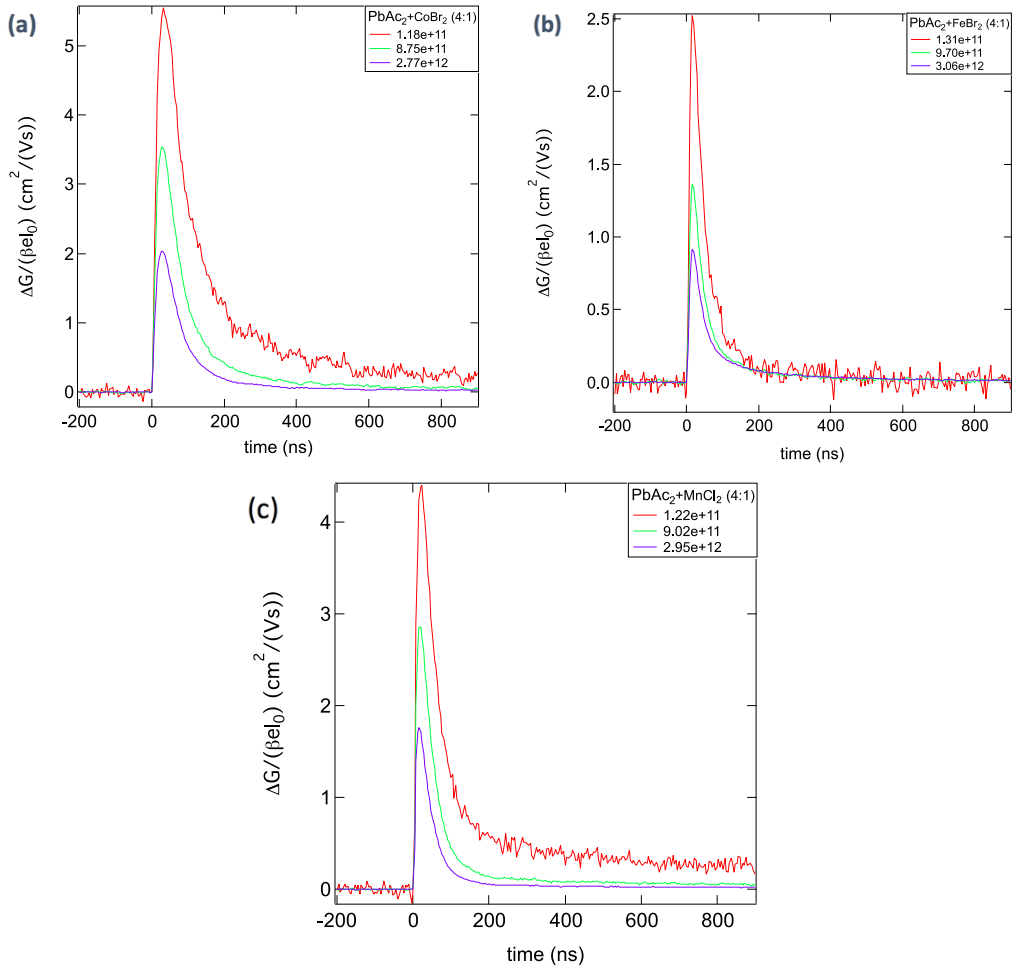

Figure 28: Photoconductance as a function of time for mixed metal perovskite compositions (a) $PbAc_2$+$CoBr_2$ (b) $PbAc_2$+$FeBr_2$ (c)$PbAc_2$+$MnCl_2$.

Laser pulse fluences were varied between ~$1*10^{11}$ to ~$2*10^{12}$ photons cm^{-2} per pulse. The maximum value of the photoconductance, as seen in figure 29 (a), decreases with laser intensity signifying the occurrence of second order recombination during the pulse. The half times are relatively constant as seen in figure 29 (b). Though $CoBr_2$ incorporated films showed slightly higher values at the same laser intensities, manganese was chosen for the next experiments as cobalt is known to be toxic to humans leading to adverse neurological conditions [95].

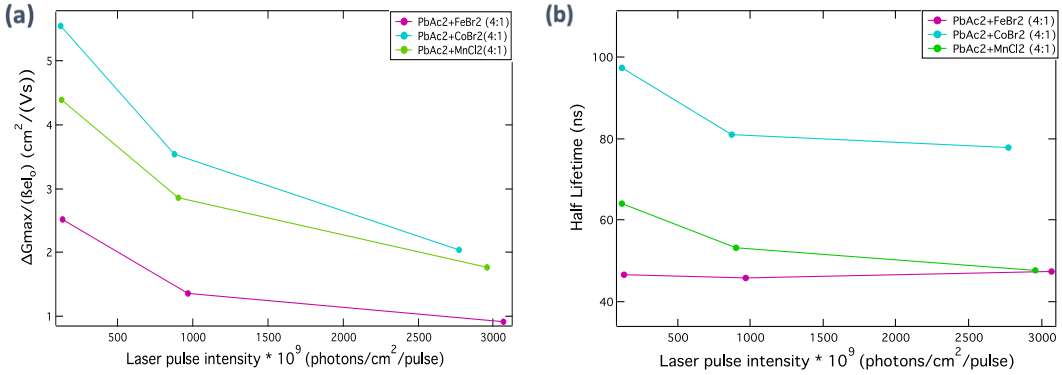

Figure 29: Electronic properties as a function of laser intensity for mixed metal perovskite compositions (a) Maximum value of photoconductance (b) Half lifetime.

5.3 Replacing lead with manganese

Manganese was selected as a viable candidate for partial substitution of lead. In order to verify how much manganese can be incorporated in the perovskite structure, 0 to 50 molar % of $PbAc_2$ was progressively replaced with $MnCl_2$ in the initial precursor solution. To maintain similar growth conditions, the molar ratio of the organic precursor to the total amount of metal salt was maintained at 3:1, however films were now thermally annealed at 100°C for a longer time of 30 minutes.

XRD diffractograms of the various perovskite films are plotted in figure 30. It is observed that the tetragonal phase of the pure lead based perovskite is maintained in the mixed metal compositions. Position of the (110) reflection and the corresponding Full Width Half Maximum (FWHM) along with the calculated average crystallite sizes are listed in table 7. However due to dependence of crystallite sizes on film thickness, peak broadening due to crystal straining [59], FWHM is used as a qualitative tool for comparing crystallinity. With increasing $MnCl_2$ inclusion, there is no discernable trend in the peak positions but it is observed that the FWHM increases and subsequently crystallinity of the perovskite film decreases. With inclusion of 30 molar % of $MnCl_2$, new reflections at 9.98°, 20.008°, 30.171° and 40.531° also appear. After comparing the results shown in figure 30 to the XRD patterns of the precursor powders and other simulated compounds as shown in appendix A, it was concluded that the new reflections appearing at 30 molar % of $MnCl_2$ are not due to unreacted precursors but might be a secondary crystalline material phase. Upon further inclusion of $MnCl_2$ the intensity of these new reflections increased along with that of the (110) (200) and (220) peaks of the tetragonal perovskite phase. From these results we conclude that until the addition of 20 molar % of $MnCl_2$, a single perovskite phase forms. Furthermore, inclusion of 60 and 70 molar % of $MnCl_2$ was attempted (see appendix A), however it led to a highly unstable material in line with a previous study where this compound was synthesized using different precursors [52].

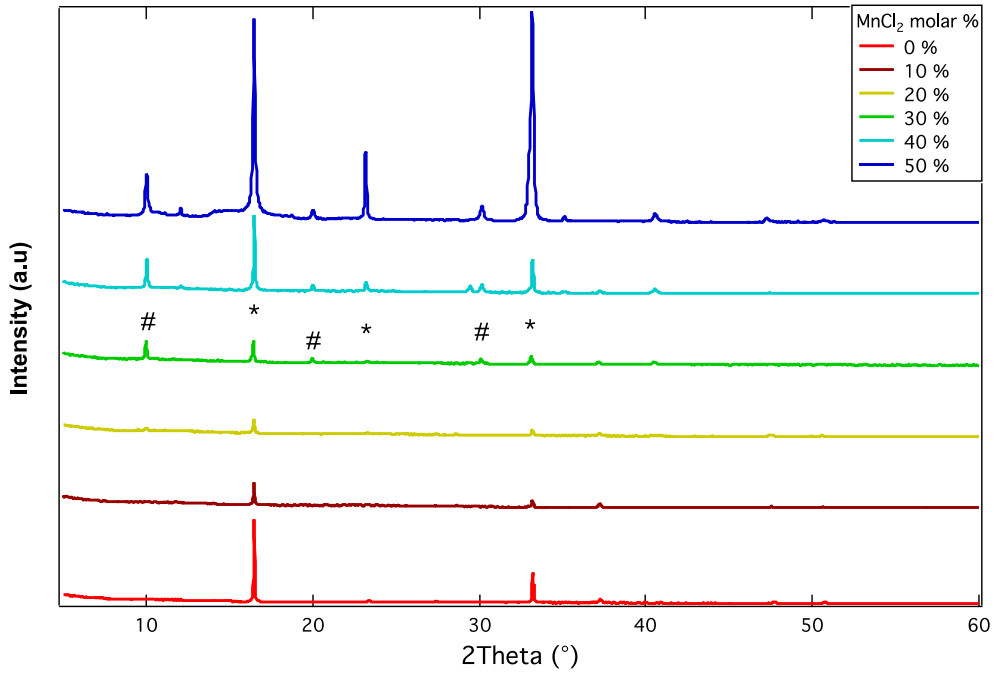

Figure 30: XRD diffractogram of perovskite films with increasing amount of $MnCl_2$, with (*) for identified tetragonal perovskite reflections and (#) for new unidentified reflections.

Table 7: Full-width-half-maximum (FWHM) of the (110) facet and the calculated crystallite size using Scherrer equation.

$MnCl_2$ molar %	(110) Peak 2theta (°)	FWHM	Crystallite Size (Å)
0	16.461	0.081	1271
10	16.443	0.079	1303
20	16.441	0.098	1051.5
30	16.447	0.109	953.2
40	16.464	0.094	1100.8
50	16.449	0.134	772.8

Optical properties of the various films were studied using UV-VIS absorption and PL emission spectroscopy as shown in figure 31 (a) and (b) respectively. The absorption spectra for the different mixed metal compositions are relatively similar with an onset around 800 nm. However, beginning at 40 molar % inclusion of $MnCl_2$ an additional absorption peak is observed at 364 nm. From the PL emission spectra, it can be observed that all the compositions show a detectable peak with a possible indication that $MnCl_2$ addition possibly enhances the emission, though this may also be caused due to other reason such as morphology effects.

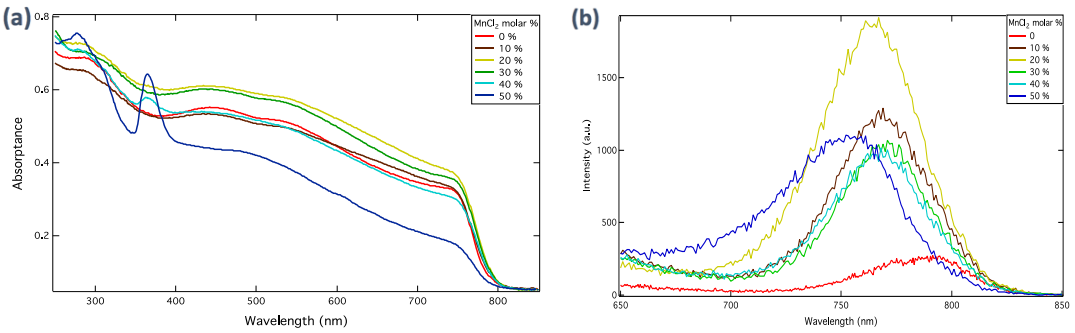

Figure 31: Optical properties of perovskite films containing increasing amounts of $MnCl_2$ (a) UV-Vis absorption spectra (b) PL emission spectra.

In figure 32, the peak emission wavelengths are plotted against molar % of $MnCl_2$ and it is observed that there are two distinct blue shifts. Lead only perovskite films show a peak wavelength of 792 nm and then with addition of $MnCl_2$ till 40 molar % the peak is shifted to and maintained at around 770 nm while at 50 molar %, the peak gets broader and shifts to 752 nm. This might be due to the effect of chlorine from the $MnCl_2$, similar to what is observed in section 5.1 for perovskites obtained from mixed lead sources ($PbAc_2$+$PbCl_2$), or it might be due to the substitution of lead by manganese.

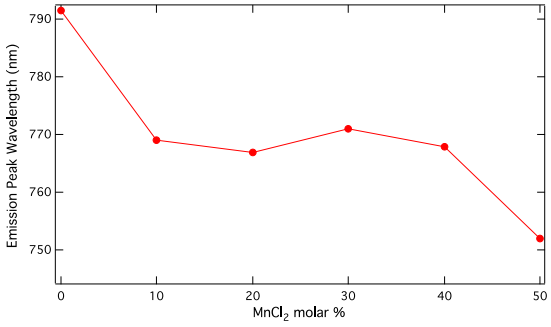

Figure 32: PL emission peak wavelength for perovskite films containing increasing amounts of $MnCl_2$.

The PL decay was tracked using single photon counting as shown in figure 33. It was observed that the decay becomes faster for increased $MnCl_2$ addition, until 50 molar % at which the lifetime becomes slightly longer and shows a different trend.

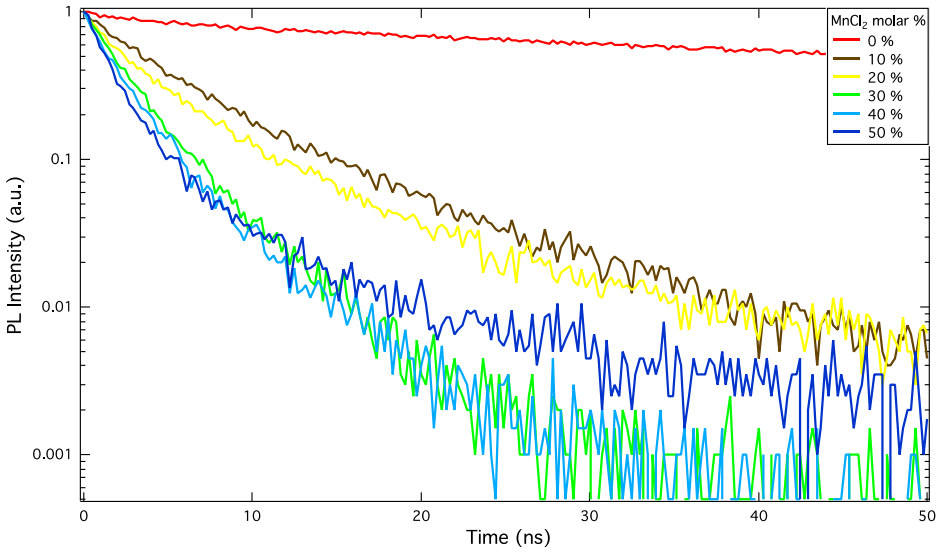

Figure 33: PL decay curves for perovskite films containing increasing amounts of $MnCl_2$.

Charge carrier dynamics of the various films were studied using TRMC measurements as shown in figures 34 (a) - (f). Only for the 0 and 10 molar % of $MnCl_2$ inclusion the ΔG_{max} decreases with increase in laser intensity, indicating that second order recombination is occurring during the pulse in these cases while with any more addition traps are being created.

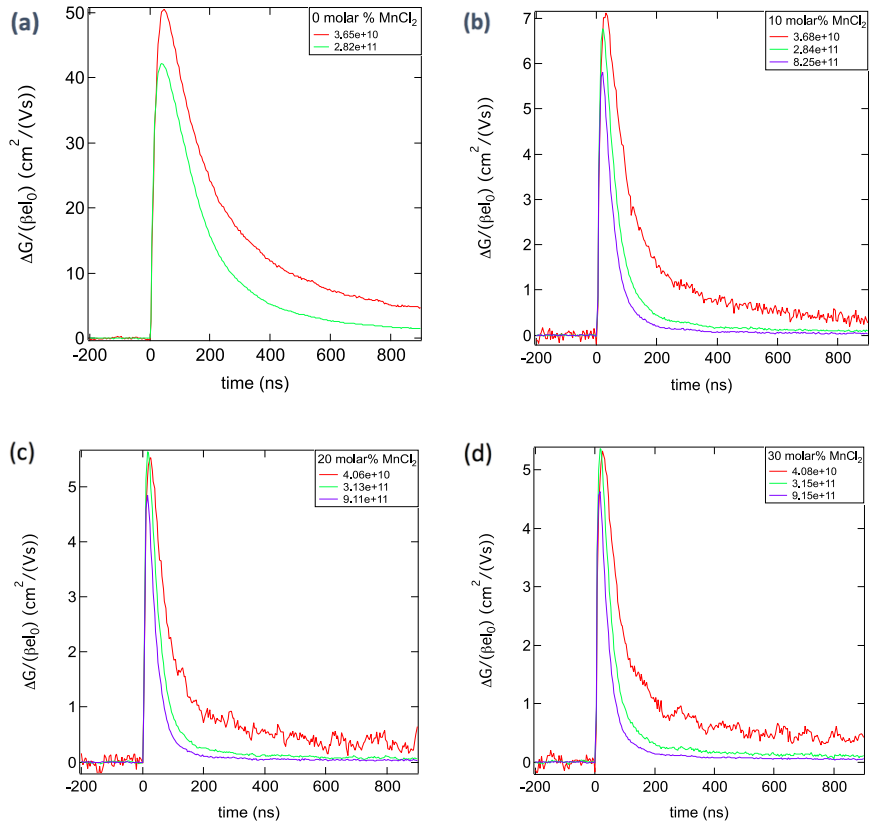

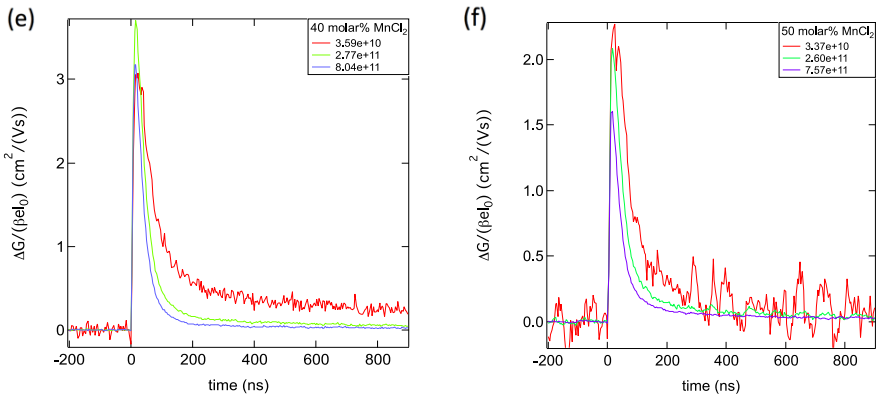

Figure 34: Photoconductance as a function of time for perovskite films containing increased amounts of $MnCl_2$ (a) 0 % (b) 10 % (c) 20% (d) 30 % (e) 40 % (f) 50 %.

The maximum change in photoconductance drops upon addition of $MnCl_2$ as can be see in figure 35. A drop in ΔG_{max} is related directly to a drop in $\eta\Sigma\mu$, as described earlier in section 4. Since we do not see an excitonic peak in our absorption spectra we can assume that all the absorbed photons generate free charges ($\eta = 1$) and that most of the drop in photoconductance can be related to a decrease in the mobilities of the charge carriers.

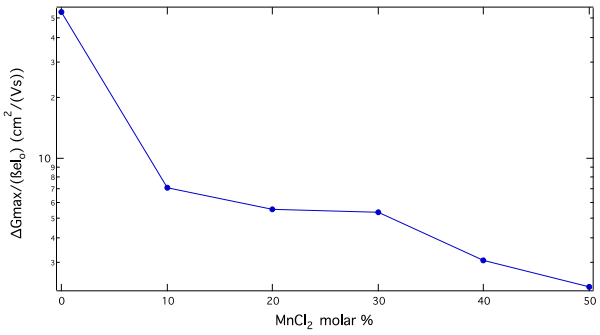

Figure 35: Maximum change in photoconductance for perovskite films containing increasing amounts of $MnCl_2$ for the incident laser intensity ~4 * 10^{10} photons/cm^2.

SEM was used to study the various thin films and the backscattered electron images obtained are shown in figure 36 (a) – (f). Since BSE images allow significant atomic number contrast, it can be hypothesized that the brighter regions contain elements with higher atomic number. It is observable that adding more than 30 molar % of $MnCl_2$ results in noticeable segregation of elements with dark and bright regions distributed throughout the film. It was also observed that the films consisting of 40 and 50 molar % $MnCl_2$ were sensitive to air and/or electron bombardment, as they appeared lighter after the imaging. EDX spot analysis was also performed to study whether the stoichiometry of the solution is maintained in the deposited thin film. The Mn:Pb atomic ratios are listed in table 8. Furthermore, compositional maps of all the elements were made over a section of the thin film to observe the homogeneity of their distribution and can be seen in the appendix B. Since, EDX receives signals from the bulk of the film, atleast near the quartz interface it can be asserted that the ratio between the metal cations are well preserved and in line with the stoichiometry of the perovskite solution.

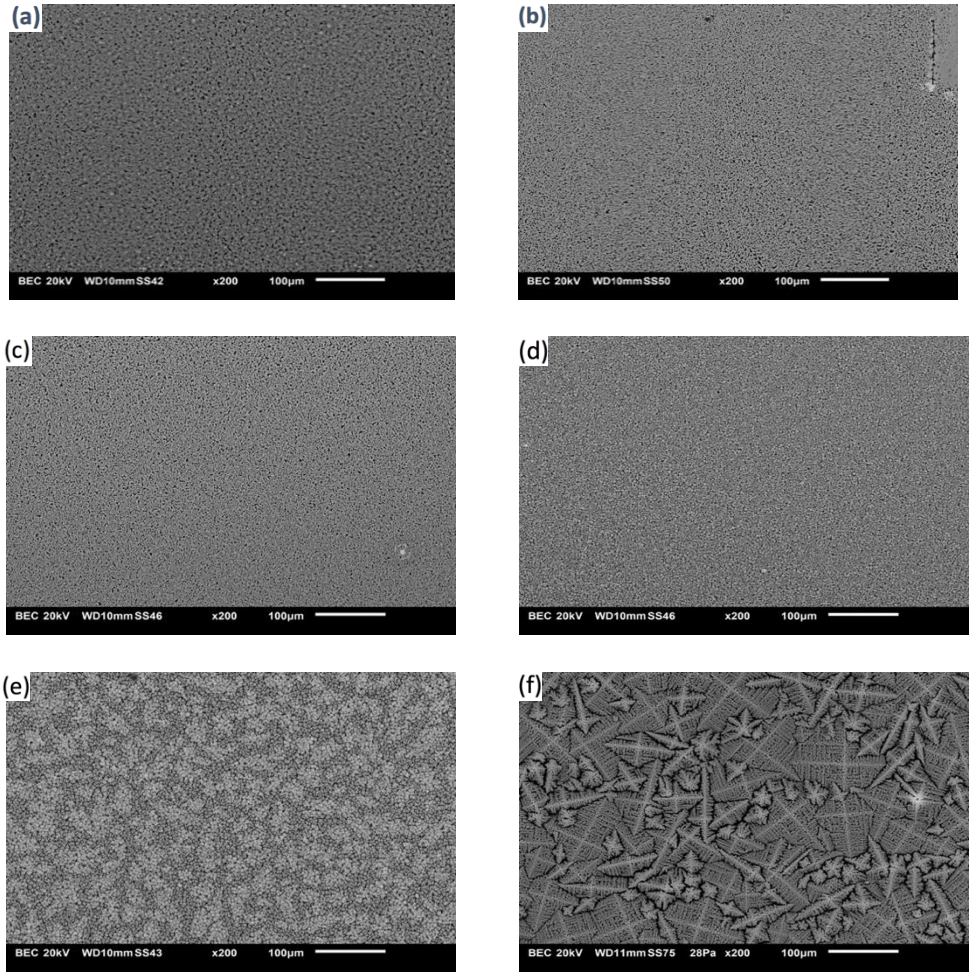

Figure 36: Backscattered electron images of perovskite films containing increasing molar % of $MnCl_2$ (a) 0 % (b) 10 % (c) 20% (d) 30 % (e) 40 % (f) 50 %.

Table 8: Relative atomic ratio of metal ions in thin films from EDX spot analysis.

Molar % of $MnCl_2$	Metal	
	Mn	Pb
0 %	0	1
10 %	0.09	1
20 %	0.19	1
30 %	0.26	1
40 %	0.46	1
50 %	1.07	1

5.4 Non-perovskite phase

From the previous results it was concluded that the limit of $MnCl_2$ addition in to the perovskite mixture is around 30 molar %. Increasing the amount of $MnCl_2$ in the precursor solution results in thin films with unidentified XRD reflections, an additional absorption feature, lower values of photoconductance and visible segregation of phases in backscattered electron images. In this section, the effect of increased thermal treatment time on the properties of the final perovskite

film was studied and attempts were also made to ascertain the composition of the non perovskite phase. Three types of perovskite films were prepared in which 30 molar % of $PbAc_2$ was replaced by $MnCl_2$, $MnBr_2$ and $PbCl_2$ respectively. All the films were prepared by the previously discussed synthesis method however the thermal annealing time was varied between 30, 60 and 120 minutes.

XRD measurements were carried out for the three types of thin films as shown in figure 37 (a) – (c). It is observable that the XRD reflection at 9.98° appears only with $MnCl_2$ replacement, furthermore with increased annealing time it reduces in intensity before disappearing entirely after 120 minutes. In the case of replacement with $MnBr_2$, new XRD reflections appear that also cannot be easily attributed to any of the precursors or intermediate perovskite structures as shown in appendix A. From the XRD diffractograms, it can be hypothesized that the intermediate structure in focus is due to the presence of both Cl and Mn, because other sources of Cl ($PbCl_2$) and Mn ($MnBr_2$) don't result in the same XRD peaks.

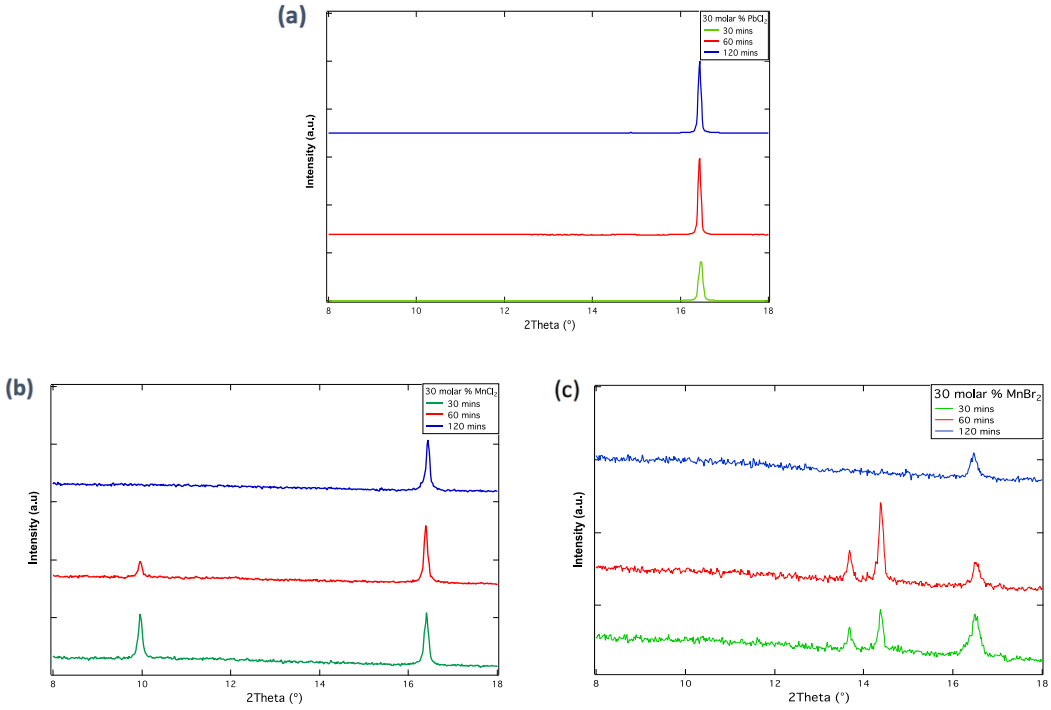

Figure 37: XRD diffractograms with increasing annealing times of perovskite films synthesized using (a) 30 molar % $PbCl_2$ (b) 30 molar % $MnCl_2$ (c) 30 molar % $MnBr_2$.

The optical properties were then studied using UV-VIS absorption spectroscopy as shown in figure 38. It is observed that the typical sharp onset and shape of the absorption spectrum is similar in the case of $PbCl_2$ and $MnCl_2$ addition but only partially observed after 120 minutes of annealing in the case of $MnBr_2$ inclusion. Both the perovskites films that were fabricated from precursor solutions containing 30 molar % of a Mn salt show additional absorption features within the wavelength range 360 to 380 nm that disappears after 120 minutes of annealing.

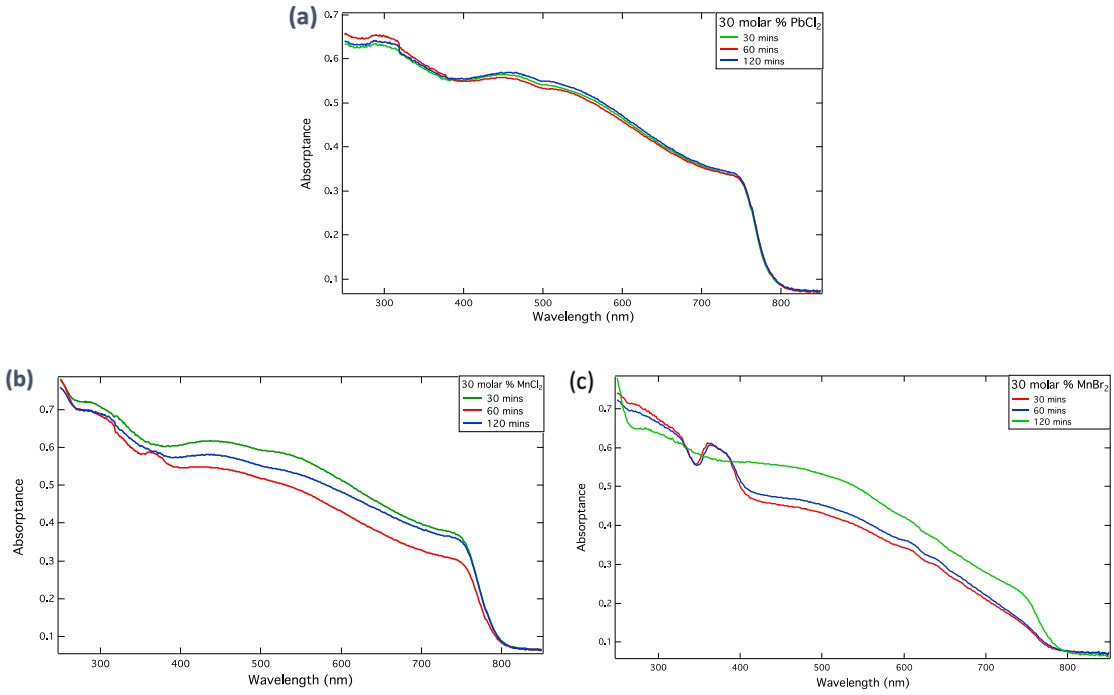

Figure 38: UV-VIS absorption spectra with increasing annealing times of perovskite films synthesized using (a) 30 molar % $PbCl_2$ (b) 30 molar % $MnCl_2$ (c) 30 molar % $MnBr_2$.

TRMC measurements were carried out for all three types of perovskite films and the max photoconductance (ΔG_{max}) was plotted versus the laser intensity as seen in figure 39. A general observation is that the films synthesized from a Mn salt ($MnCl_2$ or $MnBr_2$) show the highest signal after annealing for 120 minutes, while the perovskite film with 30 molar % of $PbCl_2$ achieves its maximum already after 60 minutes.

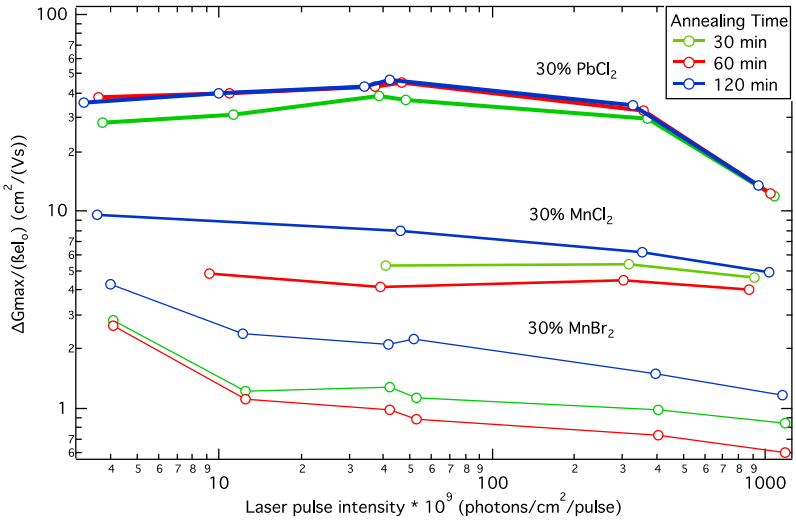

Figure 39: Maximum value of photoconductance as a function of laser intensity for increasing annealing of perovskite films synthesized using (a) 30 molar % $PbCl_2$ (b) 30 molar % $MnCl_2$ (c) 30 molar % $MnBr_2$.

SEM images were taken for all the three types of perovskite films however the films containing 30 molar % of $MnBr_2$ showed excessive phase segregation (appendix C) and were not studied further.

The backscattered images of the perovskite films synthesized using $PbCl_2$ and $MnCl_2$ are shown in figure 40 and 41 respectively. Both the types of films show similar contrast in images with a largely homogenous phase composition. One interesting observation is the effect of

thermal treatment on the amount of chlorine remaining in the film as shown in table 9. In the films synthesized using $PbCl_2$, Cl is undetectable already after 30 minutes of annealing. However significant amount of Cl remaining in the Mn based film hints at its affinity to incorporate Cl into the perovskite structure in contrast to the low concentration said to be allowed in $MAPbI_3$ [39]. With longer annealing time, and comparing with the XRD results shown in figure 37 (b) Cl might be also helping facilitate the removal of the non-perovskite phase and subsequently being removed from the mixed-metal perovskite structure.

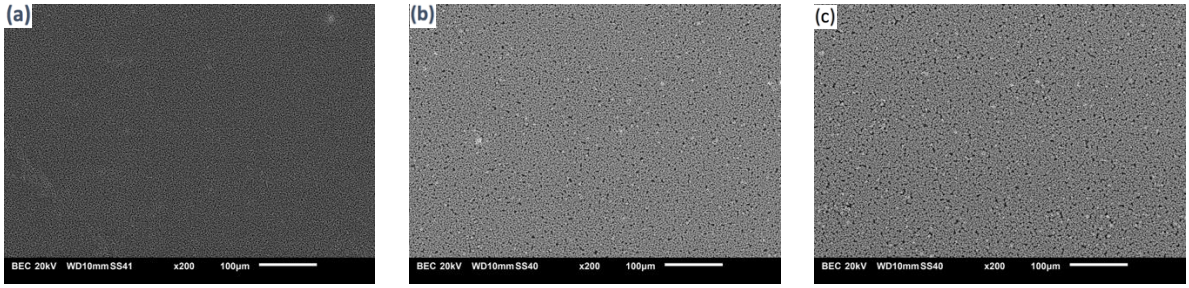

Figure 40: Backscattered electron images of perovksite films containing 30 molar % of $PbCl_2$ with increasing annealing times (a) 30 minutes (b) 60 minutes (c) 120 minutes.

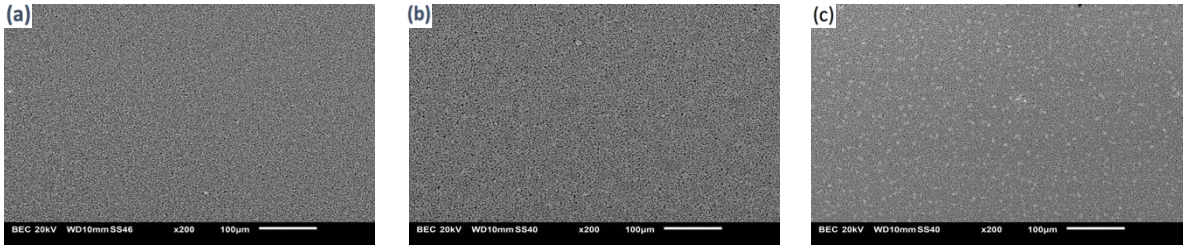

Figure 41: Backscattered electron images of perovksite films synthesized using 30 molar % of $MnCl_2$ with increasing annealing times (a) 30 minutes (b) 60 minutes (c) 120 minutes.

Table 9: Table: Atomic % of Chlorine with respect to iodine using EDX elemental spot analysis.

Film	Relative ratio (Cl/I)		
	30 minutes	60 minutes	120 minutes
30 molar % $PbCl_2$	Not detected	Not detected	Not detected
30 molar % $MnCl_2$	0.088	0.058	Not detected

5.5 Process optimization

Having found the upper threshold for $MnCl_2$ inclusion as well as the minimum annealing time required to remove the non-perovskite crystalline phase, focus is now shifted to the optimization of the other precursors in the perovskite solution, specifically the choice of the lead salt and the organic compound concentration. Indications obtained from results in previous sections that chlorine, a smaller halide, is possibly getting incorporated in such mixed metal perovskite compositions, it is expected that optimized iodine and chloride mixing may lead to a more desirable tolerance and octahedral factor [59] [65]. Furthermore, the enhanced PL properties (emission and lifetime) of lead only perovskite films using mixed lead sources ($PbAc_2$+$PbCl_2$) motivated using such a combination for the mixed metal perovskites. Next the molar ratio of the organic precursor to the metal salts was also varied between 3:1 to 2:1 to find the optimum amount of excess organic ions for mixed metal perovskites.

5.5.1 Variation of Lead precursor

The $MnCl_2$ concentration is fixed at 30 molar % and the lead source is varied between $PbAc_2$ and $PbCl_2$ as shown in table 10. The thin films were fabricated as described in the synthesis methods and thermal annealing is carried out for 120 minutes at 100ºC.

Table 10: Relative molar ratios of the inorganic precursors.

Notation	Molar %		
	$MnCl_2$	$PbAc_2$	$PbCl_2$
1-0	30	70	0
8-1	30	62	8
1-1	30	35	35
1-8	30	8	62
0-1	30	0	70

XRD measurements for the various films are shown in figure 42. It is observed that the intermediate XRD peaks previously removed after annealing for 120 minutes, reappear when $PbCl_2$ is more than 50 % of the Pb source and also the (200) peak of the tetragonal perovskite phase at 23.1° gets enhanced. Furthermore, for the 1-8 and 0-1 films extra reflections appear at 29.4° and 10.65°. Furthermore, texturing of the film along the (110) direction is much increased as the intensity of the peaks obtained for 8-1 are a factor of two more than the 1-0 films.

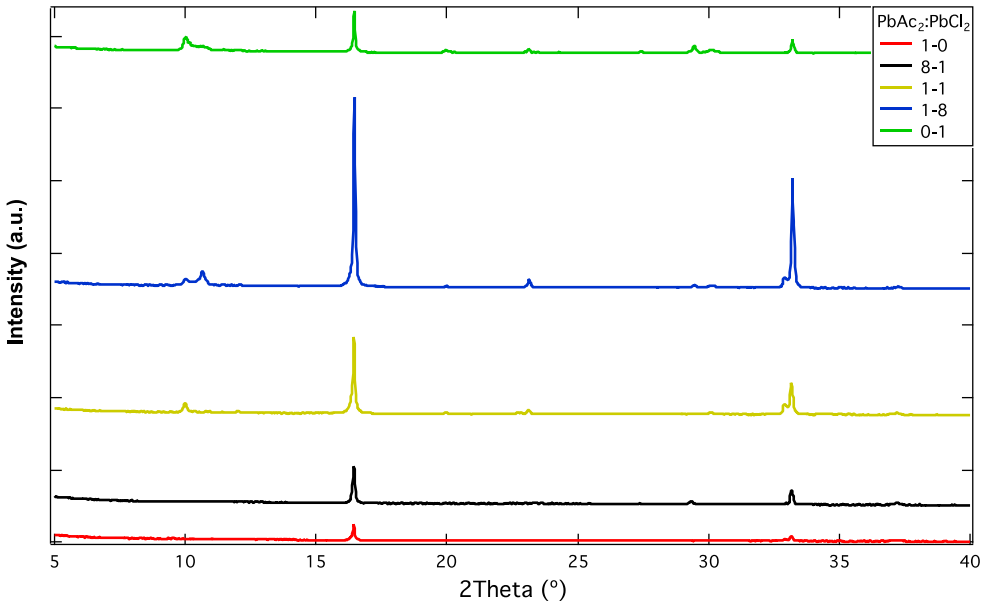

Figure 42: XRD diffractogram of perovskite films containing various ratios of mixed lead sources.

To better understand these new materials two ratios (1-8 and 0-1) were selected and each film type was annealed for 30, 60 and 120 minutes. The XRD measurements are shown in figure 43 (a) and (b). In the case of the 8-1 films, the intensity of the XRD peaks of the non-perovskite phase ($2\theta = 9.98°$) is much reduced already after 30 minutes of annealing compared to the sample fabricated without $PbCl_2$ (1-0) as seen previously in section 5.3. Interestingly, after 30 minutes of annealing the diffraction peak of (004) is visible at 32.93°, however with further annealing orientation of the perovskite structure along (110) and (220) is preferred. For the 0-1 films, the XRD peaks of the non-perovskite phase ($2\theta = 9.98°$) does not appear until they

have been annealed for 120 minutes in contrast to all the films studied till now. On the other hand, new peaks attributed to the (100) plane of $MAPbCl_3$ at 18.45° [91] is observed along with a more distinct (200) peak of $MAPbI_3$ at 23.1°. Furthermore, three more reflections are observed especially after 30 minutes of annealing at 34.81°, 14.35°, and 11.48° but they could not be indexed.

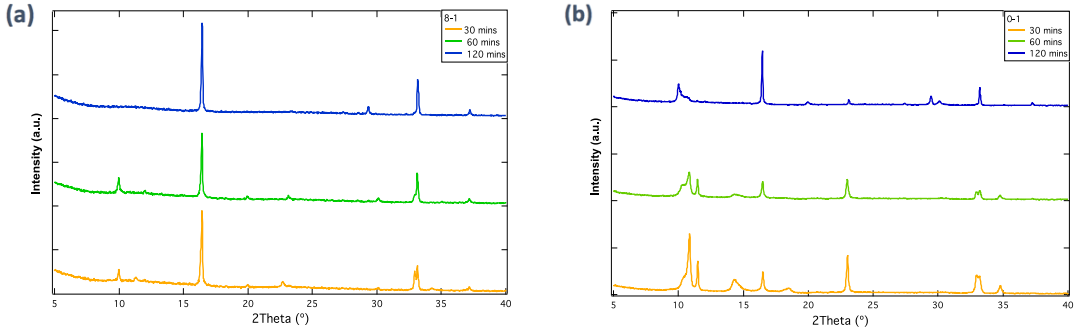

Figure 43: XRD diffractograms with increasing annealing time of perovskite films from mixed lead sources (a) $PbAc_2$ +$PbCl_2$ (8-1) (b) $PbAc_2$ +$PbCl_2$ (0-1).

Absorptance spectra of the various films types are shown in figure 44. It is apparent that the 1-0 and 8-1 films have a similar spectral shape. With further increase of $PbCl_2$ content there is a uniform decrease in absorption in the wavelength range of 500 to 800 nm and also a reappearance of the absorption feature at 365 nm.

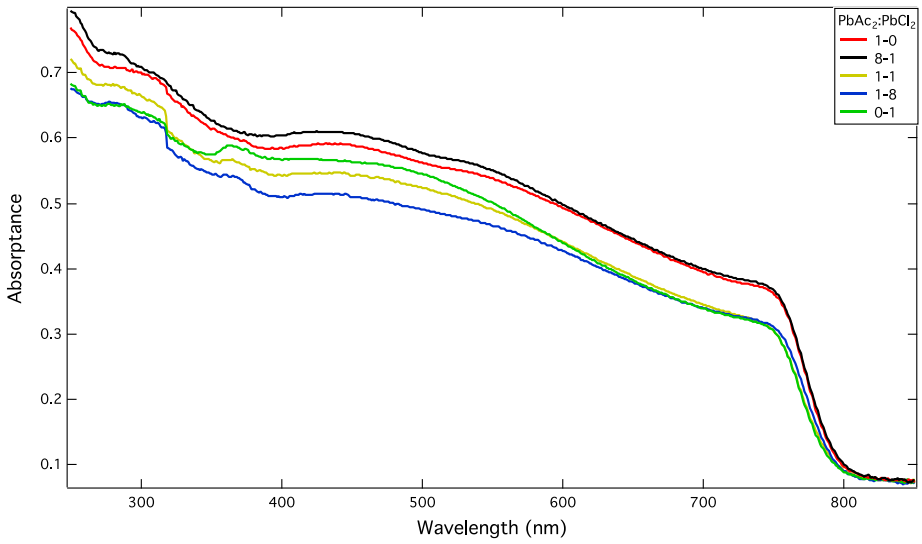

Figure 44: UV-VIS absorption spectra of perovskite films containing various ratios of mixed lead sources.

As in the case of the XRD measurements, 8-1 and 0-1 are selected due to their characteristic differences and their absorption spectral shape is tracked with increasing annealing times as shown in figure 45 (a) and (b). While the 8-1 films attain the characteristic perovskite absorption onset and spectral shape already after 30 minutes of annealing, the 0-1 films require at least 120 minutes of thermal treatment. Furthermore, though the absorption feature at 365 nm appears for both types of films, it disappears in the case of 8-1 after 120 minutes of annealing. Interestingly when compared to the spectral shape of the 1-0 films changing with annealing time, in section 5.4, this absorption feature appears to be more enhanced for both the films though the XRD reflections attributed to the non-perovskite phase is more subdued.

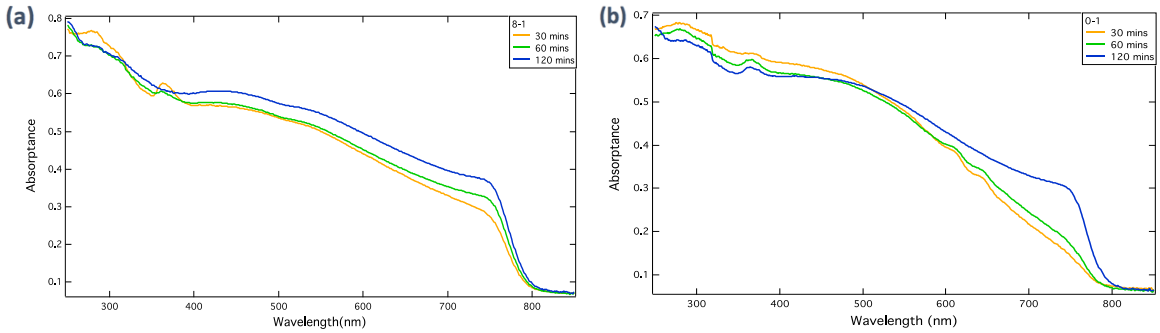

Figure 45: UV-VIS absorption spectra with increasing annealing time of perovskite films from mixed lead sources (a) $PbAc_2$ +$PbCl_2$ (8-1) (b) $PbAc_2$ +$PbCl_2$ (0-1).

PL emission spectra for the various films were also gathered as shown in figure 46. One of the noticeable features is the absence of any emission in the pure lead acetate (1-0) films after 120 minutes of annealing. However, with a minimal addition of $PbCl_2$ (8-1) PL is enhanced. Furthermore, till the 8-1 films the peak emission wavelength is maintained around 770 nm but for the pure $PbCl_2$ it blue shifts to 760 nm.

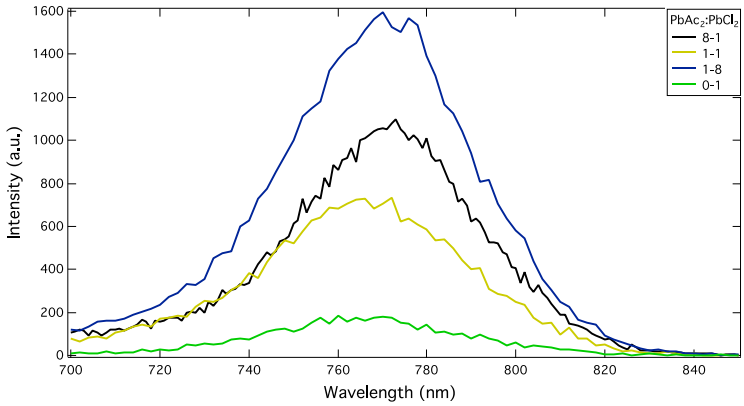

Figure 46: PL emission spectra of perovskite films fabricated from various ratios of mixed lead sources.

The PL emission of 8-1 and 0-1 films is measured for increasing annealing times as shown in figure 47 (a) and (b) respectively. The peak wavelength in the case of the 8-1 films after 30 minutes is at 768 nm before red shifting to 773 nm. While for the 0-1 films after 30 minutes it emits at a wavelength of 758 nm before red shifting slightly to 760 nm. Furthermore, in both cases with annealing time, the intensity of the peaks decreases.

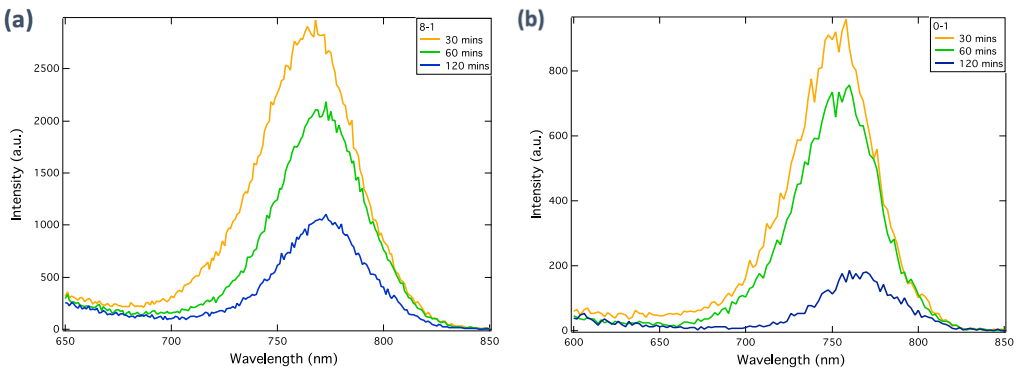

Figure 47: PL emission spectra with increasing annealing time of perovskite films from mixed lead sources (a) $PbAc_2$ +$PbCl_2$ (8-1) (b) $PbAc_2$ +$PbCl_2$ (0-1).

PL lifetimes of the various films were measured using single photon counting method as shown in figure 48. All the films except the 0-1 show a quick decay.

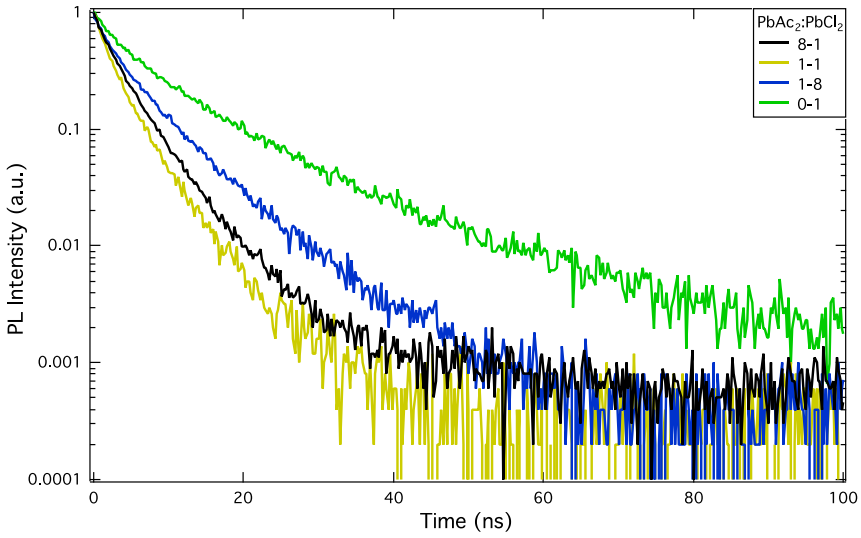

Figure 48: PL decay curves of perovskite films containing various ratios of mixed lead sources.

Furthermore, when the TRPL decay lifetimes are measured for different annealing times. In the case of the 8-1 films there is no discernible trend with all of the signal disappearing within ~80 ns. While for 0-1 films the TRPL signal initially shows much slower decay but becomes faster with longer annealing times.

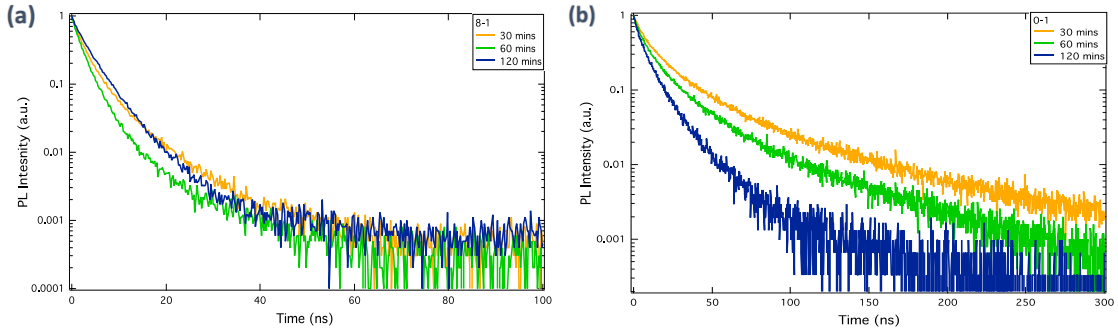

Figure 49: PL decay curves with increasing annealing time of perovskite films from mixed lead sources (a) $PbAc_2$ +$PbCl_2$ (8-1) (b) $PbAc_2$ +$PbCl_2$ (0-1).

TRMC peak signal and half lifetime for a specific laser intensity (2.79 * 10^{10} photons cm^{-2} per pulse) is compared for the various film as shown in figure 50. Furthermore, their dependence on annealing times is also plotted for the 8-1 and 0-1 films. Interestingly, the films fabricated using only $PbCl_2$ as the lead source have relatively high ΔG_{max} and long half lifetimes already after 30 minutes of annealing suggesting that the presence of $MAPbCl_3$ along with the pure iodide based perovksite does not hinder charge transport dramatically. While the 8-1 films show the highest ΔG_{max} and half lifetimes only after 120 minutes of annealing. Possibly

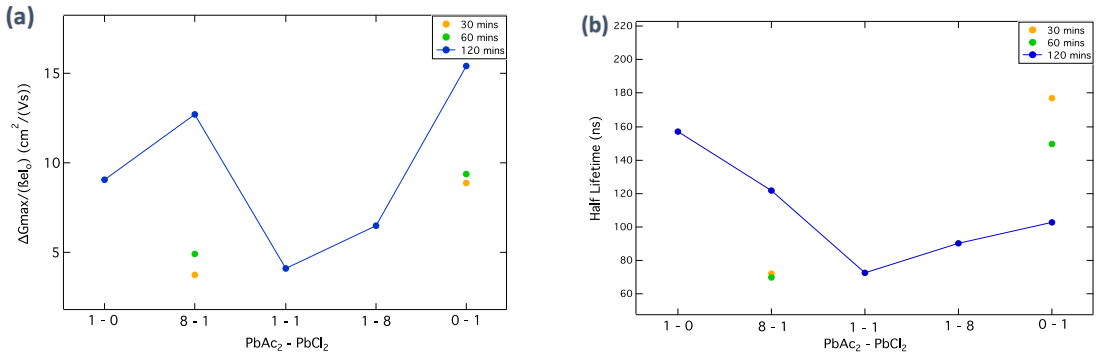

Figure 50: Electronic properties of perovskite films containing various ratios of mixed lead sources (a) Maximum value of photoconductance (b) Half lifetimes.

Backscattered electron images of all the films after 120 minutes of annealing were taken using SEM as shown in figure 51. The 1-0 and 8-1 films look similar with a slightly enlarged grain sizes in the latter. Elemental analysis results using EDX spot analysis are listed in table 11 and also the results obtained for 0-1 films in section 5. are incorporated. Interestingly there is a significant amount of Cl in the 8-1 films but no extra XRD reflections due to the non perovskite phase, this helps confirming the previous assertion that Cl can also be incorporated in small amounts in the mixed metal (Pb:Mn) perovskite structure besides helping in the removal of the non perovskite phase. There is a limit to this Cl incorporation however as with further increasing the amount of Cl, it appears that there is segregation of material phases and a noticeable change in morphology. It is observed that for the 1-8 films there is significant difference in Cl content inside the brighter spots compared to the rest of the film with both values mentioned in the table.

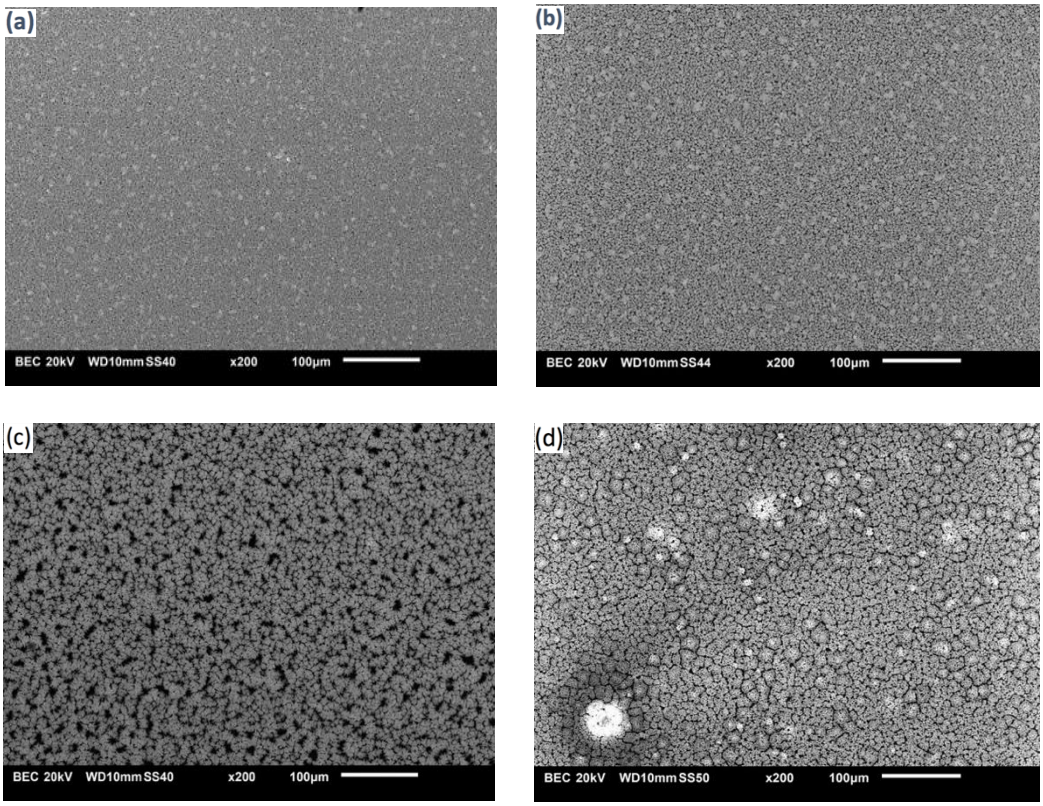

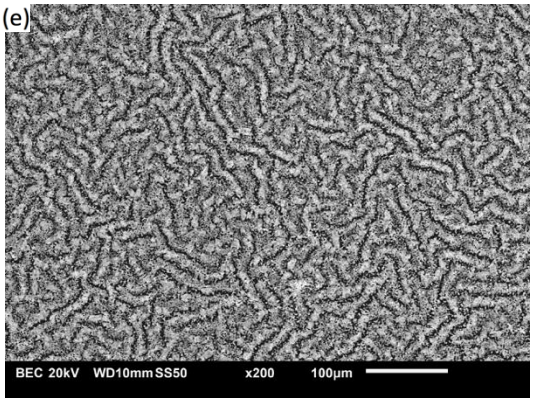

Figure 51: Backscattered electron images of perovskite films containing various ratios of mixed lead sources (a) $PbAc_2$:$PbCl_2$ (1-0) (b) $PbAc_2$:$PbCl_2$ (8-1) (c) $PbAc_2$:$PbCl_2$ (1-1) (d) $PbAc_2$:$PbCl_2$ (1-8) (e) $PbAc_2$:$PbCl_2$ (0-1).

Table 11: Relative atomic ratio of halide ions in the films from EDX spot analysis.

Film ($PbAc_2$:$PbCl_2$)	Halide (Cl/I)		
	Annealing time (mins)		
	30	60	120
1-0	0.088	0.058	0
8-1	0.32	0.19	0.083
1-1	-	-	0.138
1-8	-	-	0.09 (0.25)
0-1	-	-	0.133

5.5.2 Variation of organic precursor

From the previous section it appears that the residual Cl does not significantly hinder the electronic properties of the films but on the other hand it might be helping to enhance the PL emission peak intensities. In this section the amount of the organic compound MAI was varied with respect to the metal salts between relative molar ratios of 3:1, 2.5:1 and 2:1. The metal salt composition was split between a mixed lead sources of $PbAc_2$ and $PbCl_2$ (8-1) and $MnCl_2$ which was kept constant at 30 molar % of the total as in the previous section.

XRD measurements are carried out for the three types of films as shown in figure 52. In the case of the 2:1 films, the characteristic 110 peak of the PbI_2 at 14.7° increases in intensity as the annealing time is increased. This allowed us to set a lower threshold for the concentration of MAI as it appears that for the 2:1 films the amount of MAI is not enough to react completely with the metal cations to form the perovskite. The 2.5:1 and the 3:1 films show a similar set of reflections, however it is observed in the case of the former that already after 60 minutes of annealing the XRD peak of the non-perovskite phase at 9.98° disappears.

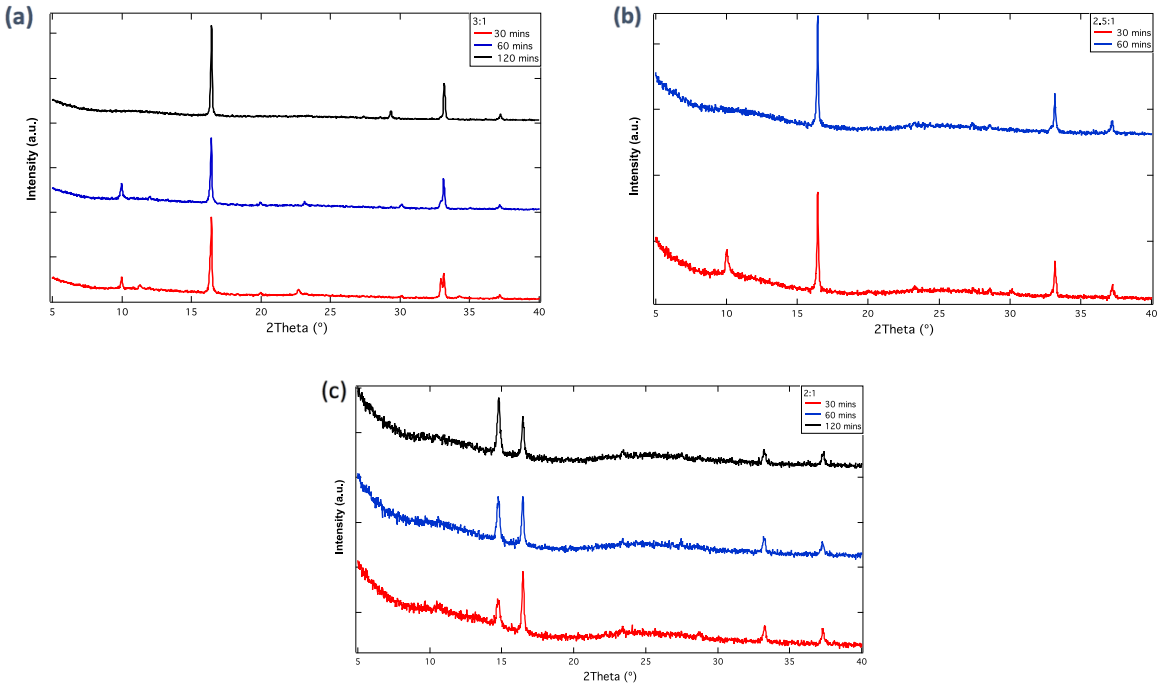

Figure 52: XRD diffractogram of perovskite films synthesized using various molar ratios of MAI:metal salts (a) 3:1 (b) 2.5:1 (c) 2:1.

Absorption of the films was studied for different annealing times using UV-VIS spectroscopy as shown in figure 53 (a) – (c). The 2.5:1 films have a sharp absorption already after 30 minutes of annealing with minimal change with further thermal treatment. Furthermore, the absorption feature at 365 nm is much lowered when compared to the 3:1 films. The 2:1 films on the other hand show a more subdued absorption edge compared to the other two types of films. However, they show increased absorption in the 300 – 500 nm wavelength range and an additional onset at ~510 nm characteristic of residual PbI_2 in the film [92].

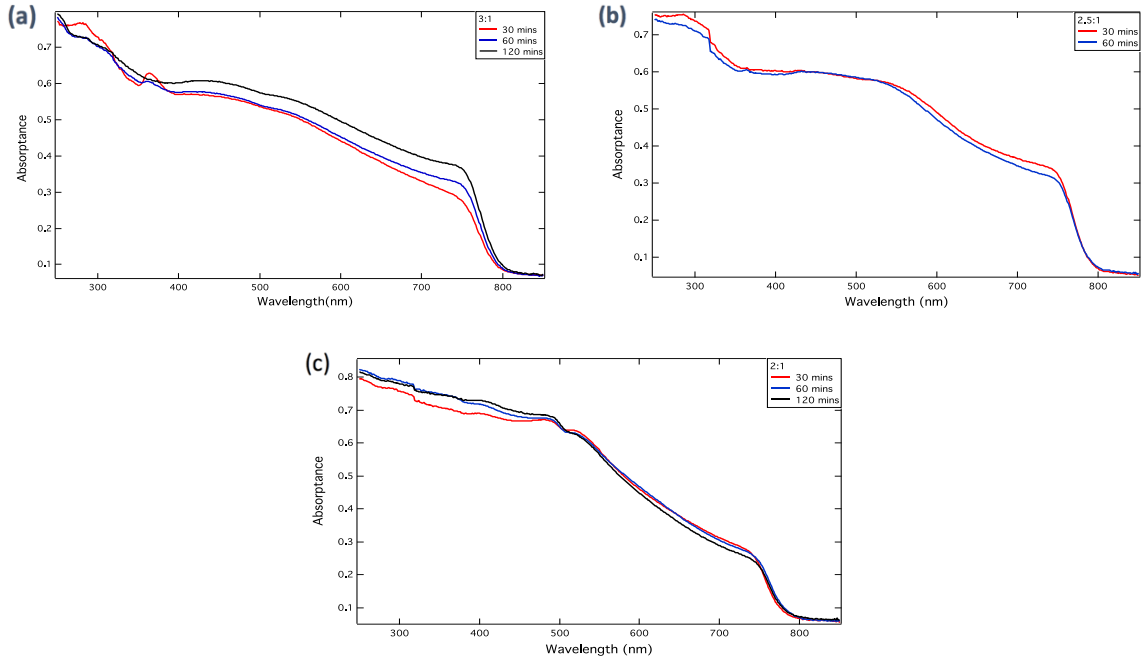

Figure 53: UV-VIS absorption spectra of perovskite films synthesized using various molar ratios of MAI:metal salts (a) 3:1 (b) 2.5:1 (c) 2:1.

PL emission peaks of the various films are shown in figure 54 (a) – (c). In all the three types of films there is a small red shift with annealing time. In the case of 3:1 as previously described after 120 minutes of annealing, the emission peak shifts to 773 nm. While for the 2.5:1 films the emission peak emits at a wavelength of 762 nm after thermal annealing for 30 minutes before shifting to 766 nm for 60 minutes of annealing. Finally, in the case of the 2:1 films it emits at around 774 nm after 30 minutes of annealing before red shifting to 778 nm for the longer annealing times. Furthermore, it is interesting to note that the PL intensity for 2.5:1 films do not get quenched with increased annealing time as has been typical in all the films in this study.

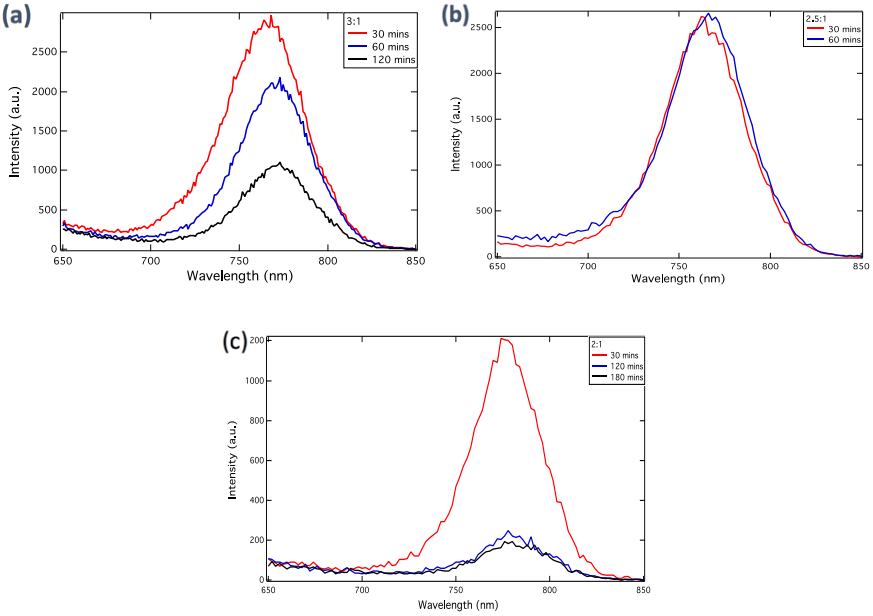

Figure 54: PL emission spectra of perovskite films synthesized using various molar ratios of MAI:metal salts (a) 3:1 (b) 2.5:1 (c) 2:1.

TRPL data was obtained using single photon counting method and the logarithmic PL intensity is plotted as a function of time as shown in figure 55 (a) – (c). The 3:1 films show relatively fast decay with all the signal disappearing within ~100 ns. The PL lifetime is significantly improved in the case of the 2.5:1 films showing a much slower decay with time. The TRPL signal of the 2:1 films show a distinctly different nature of decay with time possibly due to residual PbI_2 in the films.

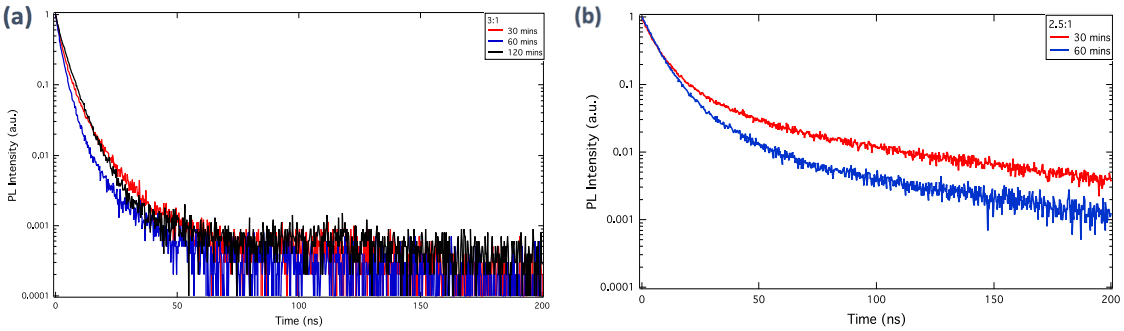

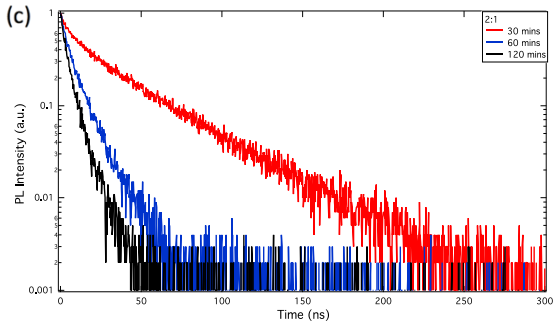

Figure 55: PL decay curves of perovskite films synthesized using various molar ratios of MAI:metal salts (a) 3:1 (b) 2.5:1 (c) 2:1.

TRMC measurements were taken for all the films and the traces for the optimum annealing times for each ratio are plotted in figure 56. The 3:1 and 2.5:1 films give similar ΔG_{max} and the decay of the signal with time is also comparable.

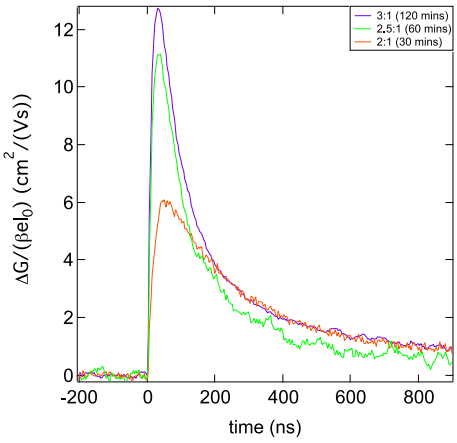

Figure 56: Photoconductance as a function of time for perovskite films synthesized using various molar ratios of MAI:metal salts.

Furthermore, the decay of the photoconductance signal with time was studied for a series of laser intensities in the case of the 2.5:1 films annealed for 60 minutes as shown in figure 57. It is observed that the ΔG_{max} progressively decreases with increasing intensity thus indicating that during the pulse recombination is of second order.

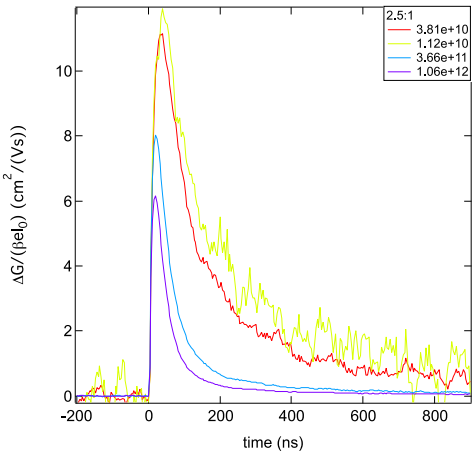

Figure 57: Photoconductance as a function of time for perovskite films synthesized using molar ratio of 2.5:1 (MAI:metal salts) at various laser intensities.

Finally, it is concluded that when mixed metal perovskite thin films are fabricated using organic compounds and metal salts maintained at an optimum ratio of 2.5:1, they show a relatively more intense PL emission peak, longer PL lifetime while requiring shorter annealing time to remove the non perovskite phase.

5.6 Film Fabrication on PEDOT:PSS

5.6.1 SEM imaging

Mixed metal (Pb:Mn) perovskite thin films with the optimized composition obtained in section 5.5 were deposited on PEDOT:PSS using solution based processes as described in the chapter 3. Secondary electron images seen in figure 58 (a) and (b), were obtained using SEM and analysed to optimize spin coating parameters. Increasing the acceleration and speed of spin coating to 2000 RPM allowed the fabrication of compact thin films with high surface coverage, while increasing the speed any further led to rougher films and large number of pin holes.

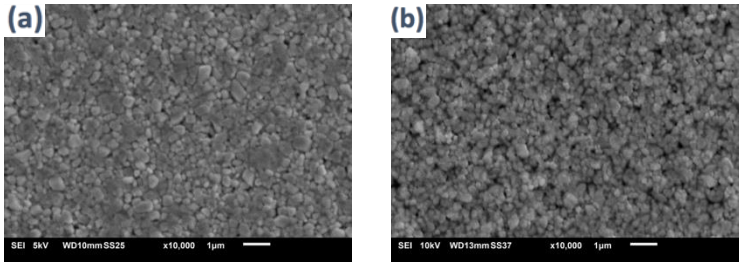

Figure 58: SEM images of mixed metal (Pb:Mn) perovskites on PEDOT:PSS spin coated at speeds (a) 2000 RPM (b) 3000 RPM.

Furthermore, commonly used techniques such as mixed-solvent (DMF+DMSO) [27] deposition and anti-solvent washing were attempted to study their effects on the morphology of these mixed metal perovskites thin films. As can be seen in figure 59 (a), DMSO appeared to destroy the film at any ratio with DMF. Amongst all the different anti solvents such as chlorobenzeme (CB), toluene, anisol [97][98] only CB washing led to a change in morphology, yielding a broader distribution of grain sizes with a few up to 1 µm in length.

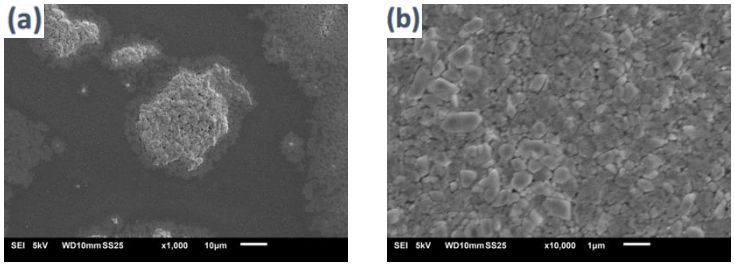

Figure 59: Techniques to improve film morphology of mixed metal (Pb:Mn) perovskites (a) mixed-solvent (DMF:DMSO) (b) chlorobenzene washing.

Cross-section SEM was coupled with EDX elemental mapping to study distribution of Mn and Pb atoms with depth. The edge of the thin film that can be seen in figure 60, was imaged and the Pb, Mn and Si elemental maps were obtained as shown in figure 61 (a) – (c). It can be observed both the metals are homogeneously distributed.

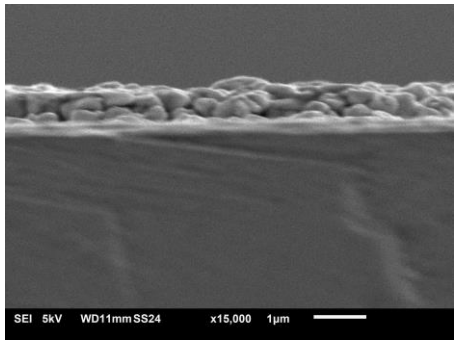

Figure 60: Cross-section SEM image of optimally deposited mixed metal (Pb:Mn) perovskite on PEDOT:PSS.

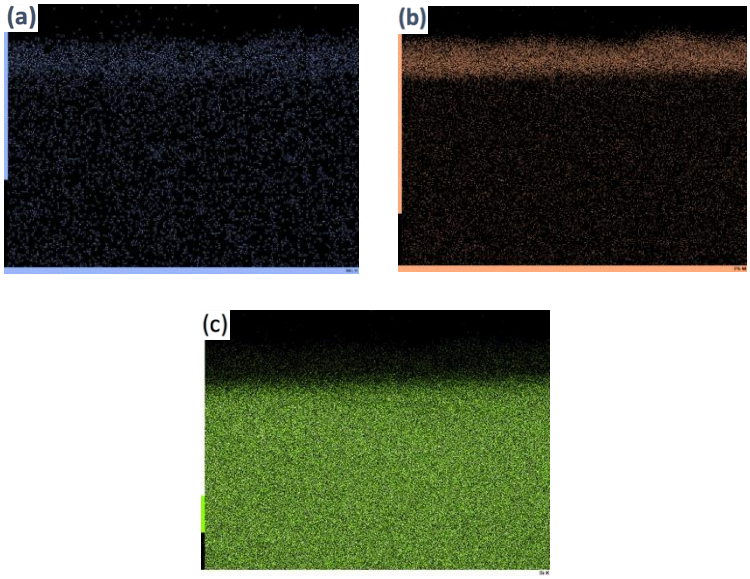

Figure 61: EDX elemental mapping of the cross-section shown in figure 60 (a) manganese (b) lead (c) silicon.

5.6.2 XPS

EDX acquires signal from the bulk of the sample. Elemental analysis of the surface was performed using XPS. We characterized films obtained from three different compositions as described in table 12. All the films were deposited on PEDOT:PSS using similar spin coating conditions.

Table 12: Types of perovskite films fabricated on PEDOT:PSS for XPS analysis.

Film notation	Perovskite solution stoichiometry	Thermal annealing (min)
Pb only	$3MAI + 0.8PbAc_2 + 0.2PbCl_2$	15
$PbAc_2 + MnCl_2$	$3MAI + 0.7PbAc_2 + 0.3MnCl_2$	120
$PbAc_2 + PbCl_2 + MnCl_2$	$2.5MAI + 0.7(8PbAc_2 + PbCl_2) + 0.3MnCl_2$	60

Figure shows the surface spectra of the three films and it can be observed that the core levels of Pb $4f_{7/2}$ and Pb $4f_{5/2}$ at 138.65 eV and 143.63 are present in all three. This is in line which is with the values reported for Pb interacting with I^- [55].

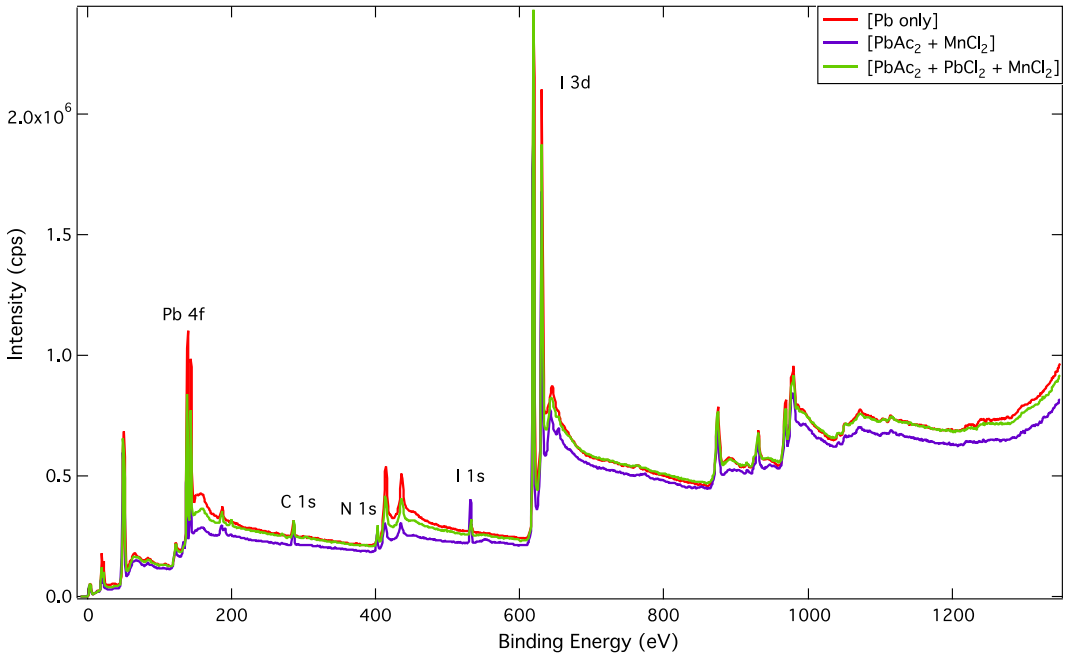

Figure 62: XPS survey scan for the various perovskite compositions.

Figure 63 focusses on the I $3d_{3/2}$ and I $3d_{5/2}$ peaks as well as a broad peak in which the signals of Mn 2p and Pb 4p overlap. There is a shift towards lower BE for the I 3d peaks with incorporation of Mn. This suggests small changes in the oxidation state of the I as previously observed for Sr [54] and might be due to possibly different interactions between Mn^{2+} and I^- as compared to between Pb^{2+} and I^-.

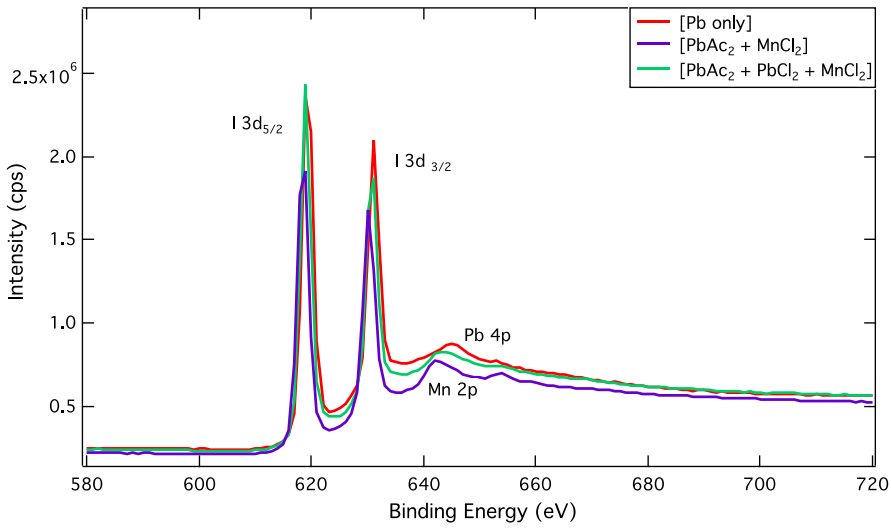

Figure 63: XPS spectra for I 3d for the various perovskite compositions.

Both films synthesized using $MnCl_2$ were then analysed with depth profiling and figure 64 shows regions of the spectra where the presence of manganese stands out. The peak is asymmetrical, the Mn 2p peak overlaps with Pb 4f signals making the relative contributions of the two elements hard to quantify. Qualitatively it can be concluded that there is significant amount of Mn distributed throughout both the films. The Mn $2p_{1/2}$ peak becomes more definite for larger etching time, *i. e.* for signal coming from deeper regions of the samples, suggesting that there is a concentration gradient of manganese in the vertical direction.

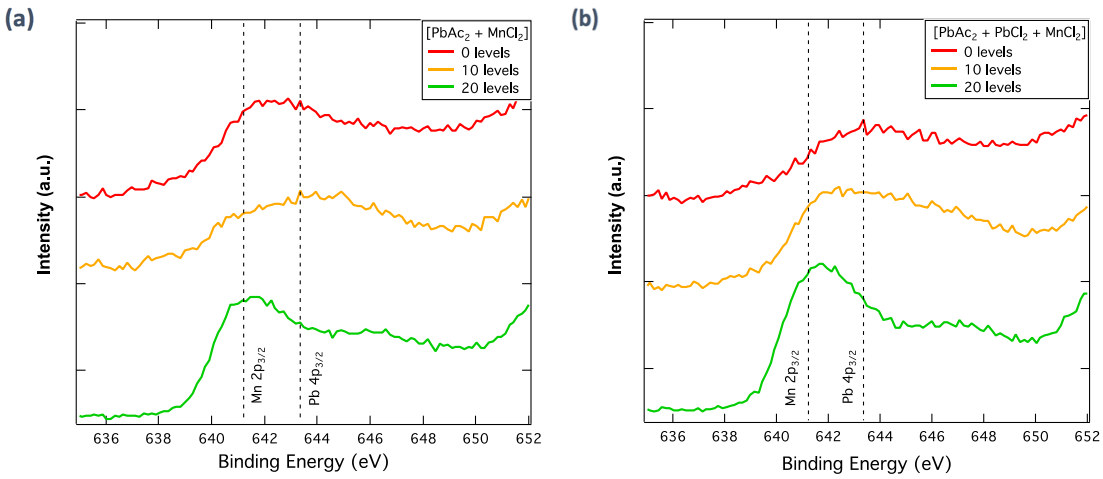

Figure 64: XPS spectra for Mn 2p and Pb 4p after 0,10 and 20 levels of etching films synthesized using $MnCl_2$.

Figure 65 (a) and (b) focusses on the Cl 2p peaks of the XPS spectra obtained for the films synthesized using MnCl2. The thin film without $PbCl_2$ shows only marginal amount of chlorine in line with the EDX results of section 5.4. Interestingly, we observed chlorine in significant amounts when $PbCl_2$ is added to the perovskite solution, with the concentration increasing further with depth. This high concentration of chlorine at the substrate interface suggests that it plays a key role in the initiation of the nucleation process and possibly modulates the perovskite crystallization kinetics as has been also observed in other binary metal compositions [57] [96]. This further corroborates the assertion that with manganese in the structure chlorine can also be incorporated in greater amounts.

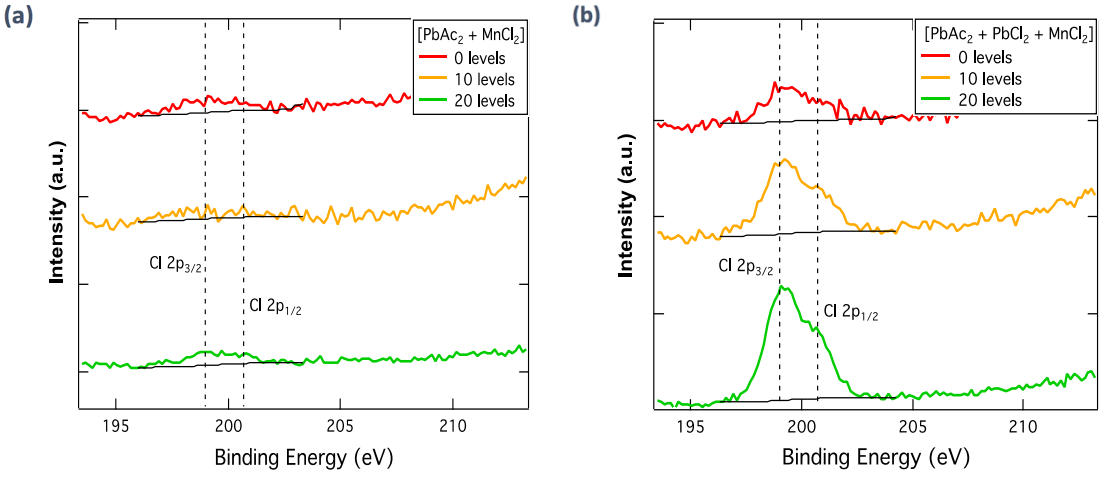

Figure 65: : XPS spectra for Cl 2p after 0,10 and 20 levels of etching films synthesized using $MnCl_2$.

The XPS data confirm that manganese is present in the sample analysed, corroborating the EDX data. Nevertheless, the data collected so far do not allow to quantify how much manganese is incorporated in the perovskite, nor whether Mn atoms replace Pb in the B sites of the lattice or are present as impurities (e. g. interstitials). This will be the subject of further investigation on the mixed Pb:Mn blends.

5.7 Solar Cell Performance

After having optimized a mixed metal (Pb-Mn) composition and deposited compact thin films on PEDOT:PSS, photovoltaic devices were fabricated as a proof of concept in the p-i-n architecture as shown in figure 66 in collaboration with TU Eindhoven. After UV-Ozone cleaning of the ITO coated glass substrates the individual layers were deposited as described in table 14.

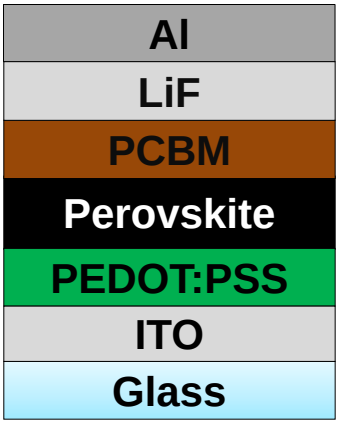

Figure 66: Photovoltaic devices with p-i-n architecture.

Table 13: Details of individual layer of photovoltaic device.

Type of layer	**Composition**	**Deposition Technique**	**Parameters**
HTM	PEDOT:PSS in water	Spin coating	1000 RPM (60 sec) 120°C (20 min)
Perovskite	30.2 mg/ml $MnCl_2$ + 186 mg/ml $PbAc_2$ + 17.2 mg/ml $PbCl_2$ + 317.9 mg/ml in DMF	Spin coating	2000 RPM (45 sec) 100°C (60 min)
ETM	20 mg/ ml PCBM in CB	Spin coating	500 RPM (60 sec)
Top electrode	1 nm LiF + 100 nm Al	Thermal Evaporation	-

A photo of one set of devices taken from the glass slide is shown in figure 67. The active area of each individual cell is 0.13 cm^2. A few films were taken out after the perovskite deposition for SEM imaging in secondary electron mode as shown in figure 68 (a) and (b). The films show a similar morphology to what was previously obtained though the coverage is poor with a significant number of pinholes which might affect the device performance.

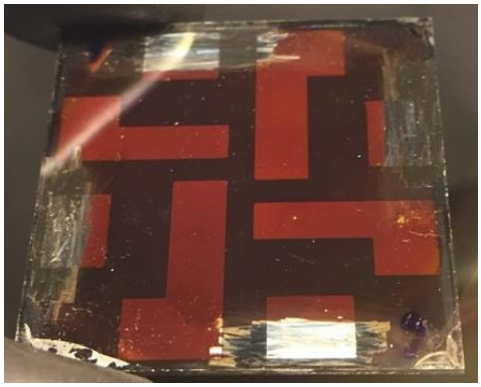

Figure 67: Optical image from the glass side of photovoltaic device.

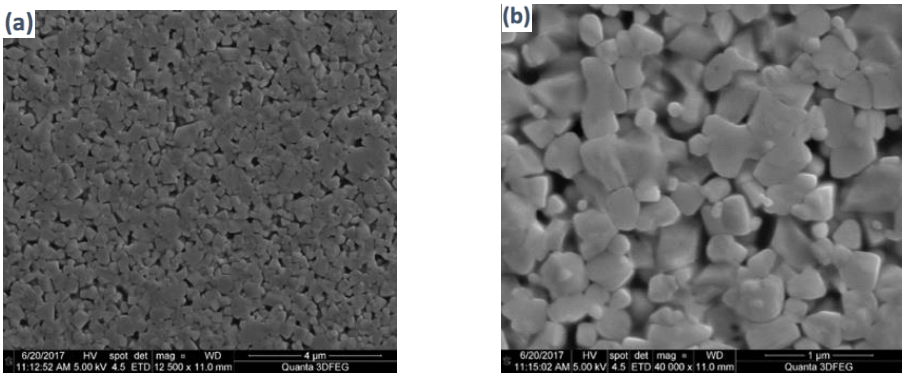

Figure 68: SEM image of mixed metal (Pb:Mn) perovskite on PEDOT:PSS at TU Eindhoven.

JV curves for the best performing device are shown in figure 69, for both forward biased and reverse biased conditions. The PV parameters are listed in table 14. Despite the low short circuit current densities (J_{sc}), the reasonably high open circuit potential (V_{oc}) is promising and indicative of its resistance to "self doping" which has been common in Sn and Ge based perovskite compositions [99]. Furthermore, compared to previous reports on Mn^{2+} substitution [52] higher performance is reported in this thesis along with higher lead substitution. The lower Fill Factor (FF) can be due to both internal and interfacial resistance between this mixed metal perovskite absorber and transport layers. This can be reduced with better film fabrication techniques such as chlorobenzene washing as previously shown as well as further optimization of the transport layers for this new composition. It is also observed that there is some hysteresis in these mixed metal compositions but to a lesser extent compared to what is commonly observed in the prototypical lead only perovskite devices [100].

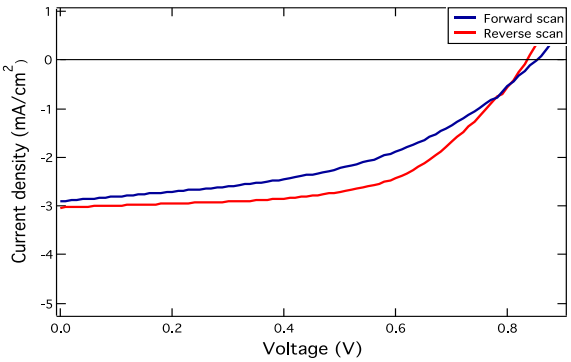

Figure 69: J-V curves for optimized mixed metal perovskite (Pb:Mn) composition based PV devices.

Table 14: PV parameters for best performing PV device.

Scan direction	J_{sc}	V_{oc}	FF	PCE
Forward	2.90	0.85	0.46	1.14
Reverse	3.03	0.83	0.58	1.45

The same device was selected for External Quantum Efficiency (EQE) measurements whose results are shown in figure 70. The integrated short circuit density without any light bias is higher than that obtained using a 520 nm bias, indicating that a significant number of free charge carriers are lost due to second order recombination before they could be collected by the transport layers.

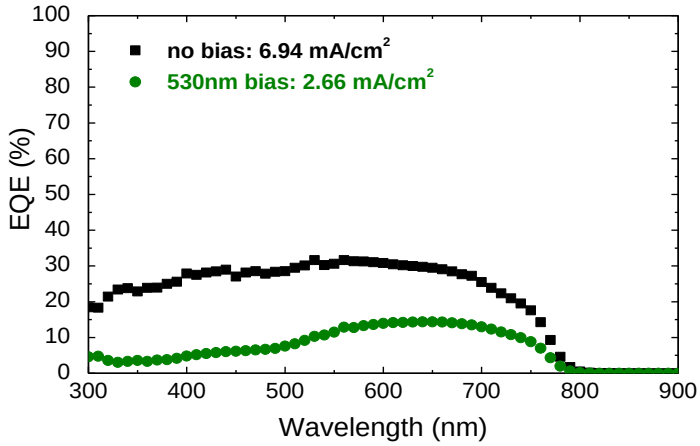

Figure 70: EQE spectrum for best performing PV device.

The photovoltaic device fabricated using the mixed metal composition serves as a proof of concept opening up further areas of research to optimize their deposition technique as well as to study and improve their interface with the transport layers.

Conclusion and outlook

6.1 Conclusion

In this thesis a reproducible lead perovskite solution processing protocol was successfully adapted for substitution of lead with alternate metal precursors. Manganese was selected as a suitable metal cation to coexist with lead in the perovskite structure and an upper limit for metal mixing was fixed with the help of geometrical parameters. This threshold was experimentally verified to be 30 % by substituting lead acetate with manganese chloride, beyond which noticeable phase segregation occurs. A secondary non-perovskite crystalline phase was also observed that was only removed with extended thermal annealing treatment. Efforts were made to figure out its composition and it was concluded that its related to the presence of three ions, methylammonium, manganese and chlorine. Subsequently an optimum ratio was found between the organic compound and the metal salts to reduce the annealing time in half and also obtain much longer PL lifetimes. It was also found that unlike lead only perovskite, significant amount of chlorine can be incorporated in these mixed metal compositions even after 120 minutes of thermal treatment. This suggests that manganese has an affinity towards a smaller anion such as chlorine. Furthermore, an enhanced presence of chlorine near the substrate suggests that it also might play a key role in the initiation of nucleation in such mixed metal (Pb:Mn) compositions. Finally, solar cells were made with these mixed metal perovskites and devices with up to 1.45% PCE were obtained, which were mainly limited by a low short circuit current and fill factor.

6.2 Outlook

Quantitative proof of the amount of manganese in the final thin film was not obtained in this thesis. Characterization using Transmission Electron Microscopy (TEM) would be highly useful to obtain this information as well as ascertain the exact position of the Mn ions in the the perovskite structure, if it is actually substituting lead.

Other manganese precursors such as $MnAc_2$ and MnI_2 would be interesting alternatives and a similar study could be done to observe to what extent Mn could be incorporated in those cases. Another alternative method of fabricating iodide based mixed metal perovskites could be via halide exchange. As these Mn:Pb compositions show an affinity to retain smaller halides in the structure, Mn:Pb bromide based perovskites might be easier to synthesize as it would lead to a more suitable octahedral factor. Subsequently, via halide exchange with iodine, compositions showing suitable band gaps for single junction photovoltaics could be obtained.

This thesis was focussed on studying the change in properties of the most well understood methylammonium based peorvskites with lead substitutions. Recently alternative cations such as formamidinium and caesium have shown better performance as well as stability in lead-only perovskites, and could prove to have the same beneficial effects for mixed metal compositions. Caesium with its small ionic size of 1.81 Å could be especially useful for tuning the tolerance factor, possibly allowing greater substitution of Pb.

Finally, the only a single PV device presented in this thesis proved the possibility of employing the Mn:Pb compound in working devices. As in the case of lead perovskites, further device optimization could result in great improvements of the performance. In particular, better film fabrication techniques, such as chlorobenzene washing, can push grain growth and increase the

surface coverage. Also, characterization of the band edges of these mixed metal compositions will open up the possibilities for a better choice of transport layers and allow better collection of free charge carriers.

Bibliography

[1] "Renewables 2017 Global Status Report", 2017.

[2] P. Rupnowski and B. Sopori, "Strength of silicon wafers: fracture mechanics approach", *International Journal of Fracture*, vol. 155, no. 1, pp. 67-74, 2009.

[3] M. Green, A. Ho-Baillie and H. Snaith, "The emergence of perovskite solar cells", *Nature Photonics*, vol. 8, no. 7, pp. 506-514, 2014.

[4] O. Eindhoven, "World record for roll-to-roll produced perovskite-based solar cells by Solliance - E52", *E52*, 2017. [Online]. Available: https://e52.nl/en/world-record-for-roll-to-roll-produced-perovskite-based-solar-cells-by-solliance/. [Accessed: 10- Mar- 2017].

[5] A. Kojima, K. Teshima, Y. Shirai and T. Miyasaka, "Organometal Halide Perovskites as Visible-Light Sensitizers for Photovoltaic Cells", *Journal of the American Chemical Society*, vol. 131, no. 17, pp. 6050-6051, 2009.

[6] W. Yang, B. Park, E. Jung, N. Jeon, Y. Kim, D. Lee, S. Shin, J. Seo, E. Kim, J. Noh and S. Seok, "Iodide management in formamidinium-lead-halide–based perovskite layers for efficient solar cells", *Science*, vol. 356, no. 6345, pp. 1376-1379, 2017.

[7] K. Bush, A. Palmstrom, Z. Yu, M. Boccard, R. Cheacharoen, J. Mailoa, D. McMeekin, R. Hoye, C. Bailie, T. Leijtens, I. Peters, M. Minichetti, N. Rolston, R. Prasanna, S. Sofia, D. Harwood, W. Ma, F. Moghadam, H. Snaith, T. Buonassisi, Z. Holman, S. Bent and M. McGehee, "23.6%-efficient monolithic perovskite/silicon tandem solar cells with improved stability", *Nature Energy*, vol. 2, no. 4, p. 17009, 2017.

[8] G. Eperon, D. Bryant, J. Troughton, S. Stranks, M. Johnston, T. Watson, D. Worsley and H. Snaith, "Efficient, Semitransparent Neutral-Colored Solar Cells Based on Microstructured Formamidinium Lead Trihalide Perovskite", *The Journal of Physical Chemistry Letters*, vol. 6, no. 1, pp. 129-138, 2015.

[9] A. Cannavale, G. Eperon, P. Cossari, A. Abate, H. Snaith and G. Gigli, "Perovskite photovoltachromic cells for building integration", *Energy Environ. Sci.*, vol. 8, no. 5, pp. 1578-1584, 2015.

[10] T. Sum and N. Mathews, "Advancements in perovskite solar cells: photophysics behind the photovoltaics", *Energy Environ. Sci.*, vol. 7, no. 8, pp. 2518-2534, 2014.

[11] B. Saparov and D. Mitzi, "Organic–Inorganic Perovskites: Structural Versatility for Functional Materials Design", *Chemical Reviews*, vol. 116, no. 7, pp. 4558-4596, 2016.

[12] S. De Wolf, J. Holovsky, S. Moon, P. Löper, B. Niesen, M. Ledinsky, F. Haug, J. Yum and C. Ballif, "Organometallic Halide Perovskites: Sharp Optical Absorption Edge and Its Relation to Photovoltaic Performance", *The Journal of Physical Chemistry Letters*, vol. 5, no. 6, pp. 1035-1039, 2014.

[13] A. Miyata, A. Mitioglu, P. Plochocka, O. Portugall, J. Wang, S. Stranks, H. Snaith and R. Nicholas, "Direct measurement of the exciton binding energy and effective masses for charge carriers in organic–inorganic tri-halide perovskites", *Nature Physics*, vol. 11, no. 7, pp. 582-587, 2015.

[14] Y. Yamada, T. Nakamura, M. Endo, A. Wakamiya, and Y. Kanemitsu, “Photoelectronic Responses in Solution-Processed Perovskite CH3NH3PbI3 Solar Cells Studied by Photoluminescence and Photoabsorption Spectroscopy,” IEEE Journal of Photovoltaics, vol. 5, no. 1, pp. 401–405, 2015.

[15] C. Wehrenfennig, G. Eperon, M. Johnston, H. Snaith and L. Herz, "High Charge Carrier Mobilities and Lifetimes in Organolead Trihalide Perovskites", *Advanced Materials*, vol. 26, no. 10, pp. 1584-1589, 2013.

[16] J. Moser, "Perovskite photovoltaics: Slow recombination unveiled", *Nature Materials*, vol. 16, no. 1, pp. 4-6, 2016.
[17] T. Wang, B. Daiber, J. Frost, S. Mann, E. Garnett, A. Walsh and B. Ehrler, "Indirect to direct bandgap transition in methylammonium lead halide perovskite", *Energy Environ. Sci.*, vol. 10, no. 2, pp. 509-515, 2017.
[18] E. Hutter, M. Gélvez-Rueda, A. Osherov, V. Bulović, F. Grozema, S. Stranks and T. Savenije, "Direct–indirect character of the bandgap in methylammonium lead iodide perovskite", *Nature Materials*, vol. 16, no. 1, pp. 115-120, 2016.
[19] L. Herz, "Charge-Carrier Mobilities in Metal Halide Perovskites: Fundamental Mechanisms and Limits", *ACS Energy Letters*, vol. 2, no. 7, pp. 1539-1548, 2017.
[20] L. Herz, "Charge-Carrier Dynamics in Organic-Inorganic Metal Halide Perovskites", *Annual Review of Physical Chemistry*, vol. 67, no. 1, pp. 65-89, 2016.
[21] A. Amat, E. Mosconi, E. Ronca, C. Quarti, P. Umari, M. Nazeeruddin, M. Grätzel and F. De Angelis, "Cation-Induced Band-Gap Tuning in Organohalide Perovskites: Interplay of Spin–Orbit Coupling and Octahedra Tilting", *Nano Letters*, vol. 14, no. 6, pp. 3608-3616, 2014.
[22] N. Jeon, J. Noh, W. Yang, Y. Kim, S. Ryu, J. Seo and S. Seok, "Compositional engineering of perovskite materials for high-performance solar cells", *Nature*, vol. 517, no. 7535, pp. 476-480, 2015.
[23] K. Butler, J. Frost and A. Walsh, "Band alignment of the hybrid halide perovskites $CH_3NH_3PbCl_3$, $CH_3NH_3PbBr_3$ and $CH_3NH_3PbI_3$", *Mater. Horiz.*, vol. 2, no. 2, pp. 228-231, 2015.
[24] F. Hao, C. Stoumpos, R. Chang and M. Kanatzidis, "Anomalous Band Gap Behavior in Mixed Sn and Pb Perovskites Enables Broadening of Absorption Spectrum in Solar Cells", *Journal of the American Chemical Society*, vol. 136, no. 22, pp. 8094-8099, 2014.
[25] S. Stranks and H. Snaith, "Metal-halide perovskites for photovoltaic and light-emitting devices", *Nature Nanotechnology*, vol. 10, no. 5, pp. 391-402, 2015.
[26] J. Heo, S. Im, J. Noh, T. Mandal, C. Lim, J. Chang, Y. Lee, H. Kim, A. Sarkar, M. Nazeeruddin, M. Grätzel and S. Seok, "Efficient inorganic–organic hybrid heterojunction solar cells containing perovskite compound and polymeric hole conductors", *Nature Photonics*, vol. 7, no. 6, pp. 486-491, 2013.
[27] N. Jeon, J. Noh, Y. Kim, W. Yang, S. Ryu and S. Seok, "Solvent engineering for high-performance inorganic–organic hybrid perovskite solar cells", *Nature Materials*, vol. 13, no. 9, pp. 897-903, 2014.
[28] J. Burschka, N. Pellet, S. Moon, R. Humphry-Baker, P. Gao, M. Nazeeruddin and M. Grätzel, "Sequential deposition as a route to high-performance perovskite-sensitized solar cells", *Nature*, vol. 499, no. 7458, pp. 316-319, 2013.
[29] H. Kim, C. Lee, J. Im, K. Lee, T. Moehl, A. Marchioro, S. Moon, R. Humphry-Baker, J. Yum, J. Moser, M. Grätzel and N. Park, "Lead Iodide Perovskite Sensitized All-Solid-State Submicron Thin Film Mesoscopic Solar Cell with Efficiency Exceeding 9%", *Scientific Reports*, vol. 2, no. 1, 2012.
[30] M. Lee, J. Teuscher, T. Miyasaka, T. Murakami and H. Snaith, "Efficient Hybrid Solar Cells Based on Meso-Superstructured Organometal Halide Perovskites", *Science*, vol. 338, no. 6107, pp. 643-647, 2012.
[31] L. Etgar, P. Gao, Z. Xue, Q. Peng, A. Chandiran, B. Liu, M. Nazeeruddin and M. Grätzel, "Mesoscopic $CH_3NH_3PbI_3/TiO_2$ Heterojunction Solar Cells", *Journal of the American Chemical Society*, vol. 134, no. 42, pp. 17396-17399, 2012.
[32] J. Manser, J. Christians and P. Kamat, "Intriguing Optoelectronic Properties of Metal Halide Perovskites", *Chemical Reviews*, vol. 116, no. 21, pp. 12956-13008, 2016.

[33] W. Zhang, M. Saliba, D. Moore, S. Pathak, M. Hörantner, T. Stergiopoulos, S. Stranks, G. Eperon, J. Alexander-Webber, A. Abate, A. Sadhanala, S. Yao, Y. Chen, R. Friend, L. Estroff, U. Wiesner and H. Snaith, "Ultrasmooth organic–inorganic perovskite thin-film formation and crystallization for efficient planar heterojunction solar cells", *Nature Communications*, vol. 6, p. 6142, 2015.

[34] D. Moore, H. Sai, K. Tan, D. Smilgies, W. Zhang, H. Snaith, U. Wiesner and L. Estroff, "Crystallization Kinetics of Organic–Inorganic Trihalide Perovskites and the Role of the Lead Anion in Crystal Growth", *Journal of the American Chemical Society*, vol. 137, no. 6, pp. 2350-2358, 2015.

[35] G. Balaji, P. Joshi, H. Abbas, L. Zhang, R. Kottokkaran, M. Samiee, M. Noack and V. Dalal, "CH3NH3PbI3 from non-iodide lead salts for perovskite solar cells via the formation of PbI2", *Phys. Chem. Chem. Phys.*, vol. 17, no. 16, pp. 10369-10372, 2015.

[36] T. Hsieh, T. Wei, K. Wu, M. Ikegami and T. Miyasaka, "Efficient perovskite solar cells fabricated using an aqueous lead nitrate precursor", *Chem. Commun.*, vol. 51, no. 68, pp. 13294-13297, 2015.

[37] P. Beckmann, "A review of polytypism in lead iodide", *Crystal Research and Technology*, vol. 45, no. 5, pp. 455-460, 2010.

[38] T. Jacobsson, M. Pazoki, A. Hagfeldt and T. Edvinsson, "Goldschmidt's Rules and Strontium Replacement in Lead Halogen Perovskite Solar Cells: Theory and Preliminary Experiments on CH3NH3SrI3", *The Journal of Physical Chemistry C*, vol. 119, no. 46, pp. 25673-25683, 2015.

[39] S. Colella, E. Mosconi, P. Fedeli, A. Listorti, F. Gazza, F. Orlandi, P. Ferro, T. Besagni, A. Rizzo, G. Calestani, G. Gigli, F. De Angelis and R. Mosca, "MAPbI3-xClxMixed Halide Perovskite for Hybrid Solar Cells: The Role of Chloride as Dopant on the Transport and Structural Properties", *Chemistry of Materials*, vol. 25, no. 22, pp. 4613-4618, 2013.

[40] S. Luo and W. Daoud, "Crystal Structure Formation of CH3NH3PbI3-xClx Perovskite", *Materials*, vol. 9, no. 3, p. 123, 2016.

[41] W. Qiu, A. Ray, M. Jaysankar, T. Merckx, J. Bastos, D. Cheyns, R. Gehlhaar, J. Poortmans and P. Heremans, "An Interdiffusion Method for Highly Performing Cesium/Formamidinium Double Cation Perovskites", *Advanced Functional Materials*, vol. 27, no. 28, p. 1700920, 2017.

[42] G. Grancini, C. Roldán-Carmona, I. Zimmermann, E. Mosconi, X. Lee, D. Martineau, S. Narbey, F. Oswald, F. De Angelis, M. Graetzel and M. Nazeeruddin, "One-Year stable perovskite solar cells by 2D/3D interface engineering", *Nature Communications*, vol. 8, p. 15684, 2017.

[43] H. Clever and F. Johnston, "The solubility of some sparingly soluble lead salts: An evaluation of the solubility in water and aqueous electrolyte solution", *Journal of Physical and Chemical Reference Data*, vol. 9, no. 3, pp. 751-784, 1980.

[44] T. Krishnamoorthy, H. Ding, C. Yan, W. Leong, T. Baikie, Z. Zhang, M. Sherburne, S. Li, M. Asta, N. Mathews and S. Mhaisalkar, "Lead-free germanium iodide perovskite materials for photovoltaic applications", *J. Mater. Chem. A*, vol. 3, no. 47, pp. 23829-23832, 2015.

[45] W. Liao, D. Zhao, Y. Yu, C. Grice, C. Wang, A. Cimaroli, P. Schulz, W. Meng, K. Zhu, R. Xiong and Y. Yan, "Lead-Free Inverted Planar Formamidinium Tin Triiodide Perovskite Solar Cells Achieving Power Conversion Efficiencies up to 6.22%", *Advanced Materials*, vol. 28, no. 42, pp. 9333-9340, 2016.

[46] D. Zhao, Y. Yu, C. Wang, W. Liao, N. Shrestha, C. Grice, A. Cimaroli, L. Guan, R. Ellingson, K. Zhu, X. Zhao, R. Xiong and Y. Yan, "Low-bandgap mixed tin–lead

iodide perovskite absorbers with long carrier lifetimes for all-perovskite tandem solar cells", *Nature Energy*, vol. 2, no. 4, p. 17018, 2017.

[47] A. Babayigit, D. Duy Thanh, A. Ethirajan, J. Manca, M. Muller, H. Boyen and B. Conings, "Assessing the toxicity of Pb- and Sn-based perovskite solar cells in model organism Danio rerio", *Scientific Reports*, vol. 6, no. 1, 2016.

[48] M. Filip and F. Giustino, "Computational Screening of Homovalent Lead Substitution in Organic–Inorganic Halide Perovskites", *The Journal of Physical Chemistry C*, vol. 120, no. 1, pp. 166-173, 2016.

[49] "Identification of Potential Replacement Materials for Lead in CH3NH3PbI3 using First Principle Calculations", arXiv, 2017.

[50] [1]J. Navas, A. Sánchez-Coronilla, J. Gallardo, N. Cruz Hernández, J. Piñero, R. Alcántara, C. Fernández-Lorenzo, D. De los Santos, T. Aguilar and J. Martín-Calleja, "New insights into organic–inorganic hybrid perovskite $CH_3NH_3PbI_3$ nanoparticles. An experimental and theoretical study of doping in Pb2+ sites with Sn2+, Sr2+, Cd2+ and Ca^{2+}", *Nanoscale*, vol. 7, no. 14, pp. 6216-6229, 2015.

[51] L. Frolova, D. Anokhin, K. Gerasimov, N. Dremova and P. Troshin, "Exploring the Effects of the Pb^{2+} Substitution in $MAPbI_3$ on the Photovoltaic Performance of the Hybrid Perovskite Solar Cells", *The Journal of Physical Chemistry Letters*, vol. 7, no. 21, pp. 4353-4357, 2016.

[52] P. Singh, P. Rana, P. Dhingra and P. Kar, "Towards toxicity removal in lead based perovskite solar cells by compositional gradient using manganese chloride", *J. Mater. Chem. C*, vol. 4, no. 15, pp. 3101-3105, 2016.

[53] "Photovoltaic properties of Cu-doped $CH_3NH_3PbI_3$ with perovskite structure", in *AIP Conference Proceedings 1807*, 2017.

[54] J. Poindexter, R. Hoye, L. Nienhaus, R. Kurchin, A. Morishige, E. Looney, A. Osherov, J. Correa-Baena, B. Lai, V. Bulović, V. Stevanović, M. Bawendi and T. Buonassisi, "High Tolerance to Iron Contamination in Lead Halide Perovskite Solar Cells", *ACS Nano*, vol. 11, no. 7, pp. 7101-7109, 2017.

[55] X. Shai, L. Zuo, P. Sun, P. Liao, W. Huang, E. Yao, H. Li, S. Liu, Y. Shen, Y. Yang and M. Wang, "Efficient planar perovskite solar cells using halide Sr-substituted Pb perovskite", *Nano Energy*, vol. 36, pp. 213-222, 2017.

[56] D. Pérez-del-Rey, D. Forgács, E. Hutter, T. Savenije, D. Nordlund, P. Schulz, J. Berry, M. Sessolo and H. Bolink, "Strontium Insertion in Methylammonium Lead Iodide: Long Charge Carrier Lifetime and High Fill-Factor Solar Cells", *Advanced Materials*, vol. 28, no. 44, pp. 9839-9845, 2016.

[57] H. Zhang, H. Wang, S. Williams, D. Xiong, W. Zhang, C. Chueh, W. Chen and A. Jen, "$SrCl_2$ Derived Perovskite Facilitating a High Efficiency of 16% in Hole-Conductor-Free Fully Printable Mesoscopic Perovskite Solar Cells", *Advanced Materials*, vol. 29, no. 15, p. 1606608, 2017.

[58] M. Klug, A. Osherov, A. Haghighirad, S. Stranks, P. Brown, S. Bai, J. Wang, X. Dang, V. Bulović, H. Snaith and A. Belcher, "Tailoring metal halide perovskites through metal substitution: influence on photovoltaic and material properties", *Energy Environ. Sci.*, vol. 10, no. 1, pp. 236-246, 2017.

[59] M. Sampson, J. Park, R. Schaller, M. Chan and A. Martinson, "Transition metal-substituted lead halide perovskite absorbers", *J. Mater. Chem. A*, vol. 5, no. 7, pp. 3578-3588, 2017.

[60] S. Das Adhikari, S. Dutta, A. Dutta, A. Guria and N. Pradhan, "Chemically Tailoring the Dopant Emission in Manganese-Doped $CsPbCl_3$ Perovskite Nanocrystals", *Angewandte Chemie*, vol. 129, no. 30, pp. 8872-8876, 2017.

[61] W. Liu, Q. Lin, H. Li, K. Wu, I. Robel, J. Pietryga and V. Klimov, "Mn2+-Doped

Lead Halide Perovskite Nanocrystals with Dual-Color Emission Controlled by Halide Content", *Journal of the American Chemical Society*, vol. 138, no. 45, pp. 14954-14961, 2016.
[62] "Crystallography and Chemistry of Perovskites", arXiv, 2017.
[63] "File:Perovskite unit cell.png - Wikimedia Commons", Commons.wikimedia.org, 2017. [Online]. Available: https://commons.wikimedia.org/wiki/File:Perovskite_unit_cell.png. [Accessed: 05- Jun- 2017].
[64] V. Goldschmidt, "Die Gesetze der Krystallochemie", *Die Naturwissenschaften*, vol. 14, no. 21, pp. 477-485, 1926.
[65] C. Li, X. Lu, W. Ding, L. Feng, Y. Gao and Z. Guo, "Formability ofABX3(X= F, Cl, Br, I) halide perovskites", *Acta Crystallographica Section B Structural Science*, vol. 64, no. 6, pp. 702-707, 2008.
[66] G. Kieslich, S. Sun and A. Cheetham, "Solid-state principles applied to organic–inorganic perovskites: new tricks for an old dog", *Chem. Sci.*, vol. 5, no. 12, pp. 4712-4715, 2014.
[67] W. Travis, E. Glover, H. Bronstein, D. Scanlon and R. Palgrave, "On the application of the tolerance factor to inorganic and hybrid halide perovskites: a revised system", Chem. Sci., vol. 7, no. 7, pp. 4548-4556, 2016.
[68] Z. Li, M. Yang, J. Park, S. Wei, J. Berry and K. Zhu, "Stabilizing Perovskite Structures by Tuning Tolerance Factor: Formation of Formamidinium and Cesium Lead Iodide Solid-State Alloys", *Chemistry of Materials*, vol. 28, no. 1, pp. 284-292, 2016.
[69] M. Birkholz, P. Fewster and C. Genzel, Thin film analysis by X-ray scattering. Weinheim: Wiley-VCH, 2009.
[70] V. Pecharsky and P. Zavalij, Fundamentals of powder diffraction and structural characterization of materials. New York: Springer, 2009.
[71] "X-rays", *ARPANSA*, 2017. [Online]. Available: https://www.arpansa.gov.au/understanding-radiation/what-is-radiation/ionising-radiation/x-ray. [Accessed: 06- May- 2017].
[72] T. Alford, L. Feldman and J. Mayer, Fundamentals of nanoscale film analysis. New York, NY: Springer, 2007.
[73] J. Goldstein, D. Newbury, P. Echlin, D. Joy, C. Lyman, E. Lifshin, L. Sawyer and J. Michael, Scanning Electron Microscopy and X-ray Microanalysis. Boston, MA: Springer US, 2003.
[74] "Microscopy - Lessons" Blendspace, 2017. [Online]. Available: https://www.tes.com/lessons/zskxzxDIXx53uw/microscopy. [Accessed: 04- Apr- 2017].
[75] R. Egerton, Physical principles of electron microscopy. New York, NY: Springer, 2008.
[76] M. Sardela, Practical materials characterization. New York, NY: Springer, 2014
[77] H. Perkampus, UV-VIS Spectroscopy and Its Applications. Berlin, Heidelberg: Springer Berlin Heidelberg, 1992.
[78] Owen, T. (2000). Fundamentals of modern UV-visible spectroscopy. [Waldbronn]: Agilent Technologies.
[79] "Integrating Sphere Theory and applications", Labsphere, 2017.
[80] F. Padera, "UV/Vis Spectroscopy", Perkin Elmer, 2017.
[81] D. Schroder, Semiconductor material and device characterization. Hoboken: IEEE Press, 2006.
[82] S. Perkowitz, Optical characterization of semiconductors. London [u.a.]: Acad. Press,

1994.
[83] "Macro Photoluminescence and Electroluminescence", Horiba Scientific, 2005.
[84] M. Wahl, Time-Correlated Single Photon Counting. PicoQuant GmbH, 2015
[85] A practical guide to time-resolved luminescence lifetime determination using dedicated Time-Correlated Single-Photon Counting systems. Glasgow: HORIBA Jobin Yvon IBH Ltd.
[86] T. Savenije, A. Ferguson, N. Kopidakis and G. Rumbles, "Revealing the Dynamics of Charge Carriers in Polymer:Fullerene Blends Using Photoinduced Time-Resolved Microwave Conductivity", The Journal of Physical Chemistry C, vol. 117, no. 46, pp. 24085-24103, 2013.
[87] L. Herz, "Charge-Carrier Mobilities in Metal Halide Perovskites: Fundamental Mechanisms and Limits", ACS Energy Letters, vol. 2, no. 7, pp. 1539-1548, 2017.
[88] J. Qing, H. Chandran, Y. Cheng, X. Liu, H. Li, S. Tsang, M. Lo and C. Lee, "Chlorine Incorporation for Enhanced Performance of Planar Perovskite Solar Cell Based on Lead Acetate Precursor", ACS Applied Materials & Interfaces, vol. 7, no. 41, pp. 23110-23116, 2015.
[89] W. Qiu, T. Merckx, M. Jaysankar, C. Masse de la Huerta, L. Rakocevic, W. Zhang, U. Paetzold, R. Gehlhaar, L. Froyen, J. Poortmans, D. Cheyns, H. Snaith and P. Heremans, "Pinhole-free perovskite films for efficient solar modules", Energy Environ. Sci., vol. 9, no. 2, pp. 484-489, 2016.
[90] Q. Wang, M. Lyu, M. Zhang, J. Yun, H. Chen and L. Wang, "Transition from the Tetragonal to Cubic Phase of Organohalide Perovskite: The Role of Chlorine in Crystal Formation of $CH_3NH_3PbI_3$ on TiO_2 Substrates", The Journal of Physical Chemistry Letters, vol. 6, no. 21, pp. 4379-4384, 2015.
[91] L. Fan, Y. Ding, J. Luo, B. Shi, X. Yao, C. Wei, D. Zhang, G. Wang, Y. Sheng, Y. Chen, A. Hagfeldt, Y. Zhao and X. Zhang, "Elucidating the role of chlorine in perovskite solar cells", J. Mater. Chem. A, vol. 5, no. 16, pp. 7423-7432, 2017.
[92] T. Zhang, M. Yang, Y. Zhao and K. Zhu, "Controllable Sequential Deposition of Planar $CH_3NH_3PbI_3$Perovskite Films via Adjustable Volume Expansion", Nano Letters, vol. 15, no. 6, pp. 3959-3963, 2015
[93] P. Gao, M. Grätzel and M. Nazeeruddin, "Organohalide lead perovskites for photovoltaic applications", Energy Environ. Sci., vol. 7, no. 8, pp. 2448-2463, 2014.
[94] S. Stranks, G. Eperon, G. Grancini, C. Menelaou, M. Alcocer, T. Leijtens, L. Herz, A. Petrozza and H. Snaith, "Electron-Hole Diffusion Lengths Exceeding 1 Micrometer in an Organometal Trihalide Perovskite Absorber", Science, vol. 342, no. 6156, pp. 341-344, 2013.
[95] L. Leyssens, B. Vinck, C. Van Der Straeten, F. Wuyts and L. Maes, "Cobalt toxicity in humans—A review of the potential sources and systemic health effects", Toxicology, vol. 387, pp. 43-56, 2017.
[96] F. Zuo, S. Williams, P. Liang, C. Chueh, C. Liao and A. Jen, "Binary-Metal Perovskites Toward High-Performance Planar-Heterojunction Hybrid Solar Cells", *Advanced Materials*, vol. 26, no. 37, pp. 6454-6460, 2014.
[97] S. Paek, P. Schouwink, E. Athanasopoulou, K. Cho, G. Grancini, Y. Lee, Y. Zhang, F. Stellacci, M. Nazeeruddin and P. Gao, "From Nano- to Micrometer Scale: The Role of Antisolvent Treatment on High Performance Perovskite Solar Cells", *Chemistry of Materials*, vol. 29, no. 8, pp. 3490-3498, 2017.
[98] G. Eperon, T. Leijtens, K. Bush, R. Prasanna, T. Green, J. Wang, D. McMeekin, G. Volonakis, R. Milot, R. May, A. Palmstrom, D. Slotcavage, R. Belisle, J. Patel, E. Parrott, R. Sutton, W. Ma, F. Moghadam, B. Conings, A. Babayigit, H. Boyen, S. Bent, F. Giustino, L. Herz, M. Johnston, M. McGehee and H. Snaith, "Perovskite-

perovskite tandem photovoltaics with optimized band gaps", *Science*, vol. 354, no. 6314, pp. 861-865, 2016.

[99] S. Hoefler, G. Trimmel and T. Rath, "Progress on lead-free metal halide perovskites for photovoltaic applications: a review", *Monatshefte für Chemie - Chemical Monthly*, vol. 148, no. 5, pp. 795-826, 2017.

[100] H. Snaith, A. Abate, J. Ball, G. Eperon, T. Leijtens, N. Noel, S. Stranks, J. Wang, K. Wojciechowski and W. Zhang, "Anomalous Hysteresis in Perovskite Solar Cells", *The Journal of Physical Chemistry Letters*, vol. 5, no. 9, pp. 1511-1515, 2014.

Appendix A

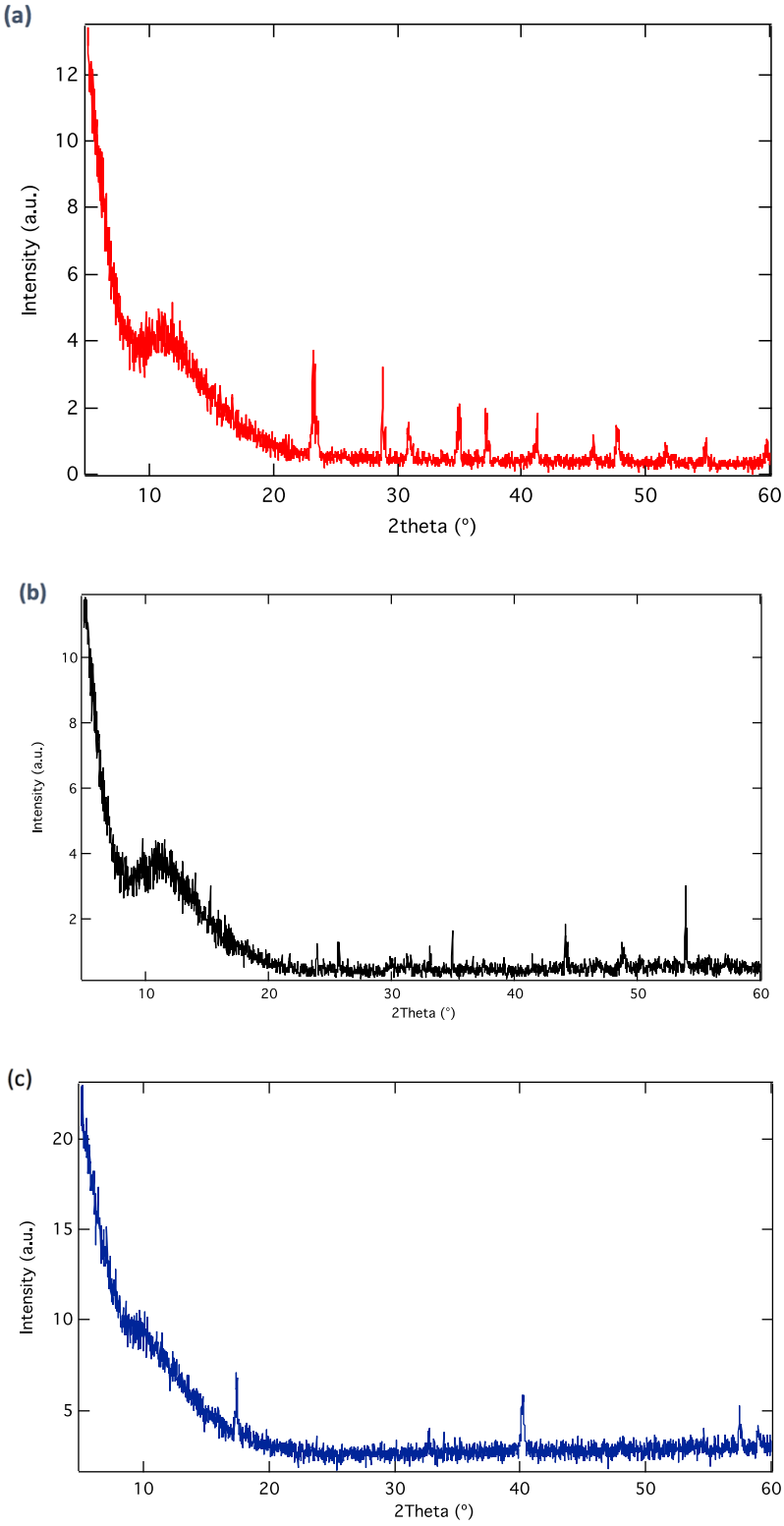

Figure 71: XRD diffractograms of precursor powder sealed in air tight holder inside nitrogen environment (a) MAI (b) $PbAc_2$ (c) $MnCl_2$

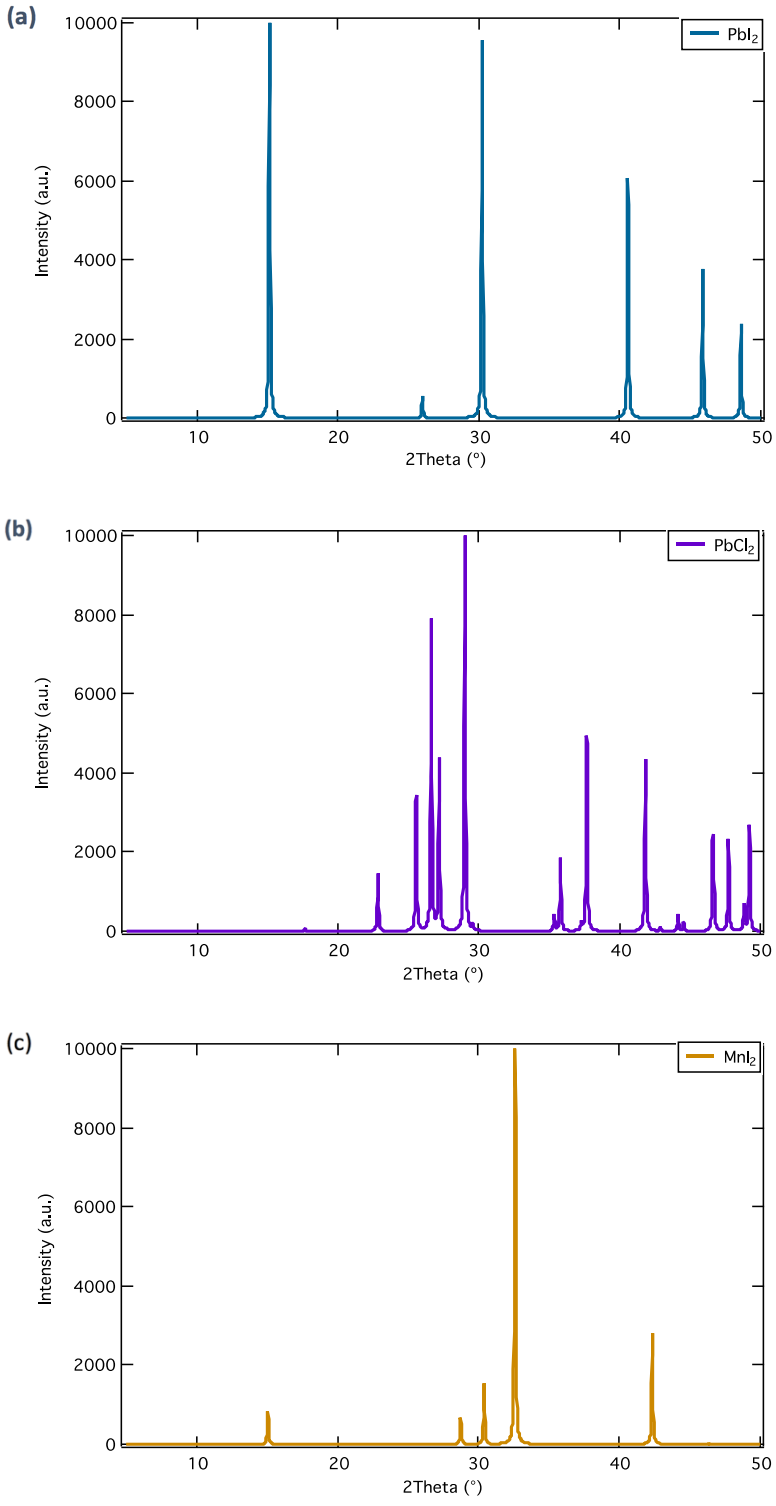

Figure 72: Simulated XRD diffractograms of possible precursor compounds formed during the reaction (a) PbI_2 (b) $PbCl_2$ (c) MnI_2

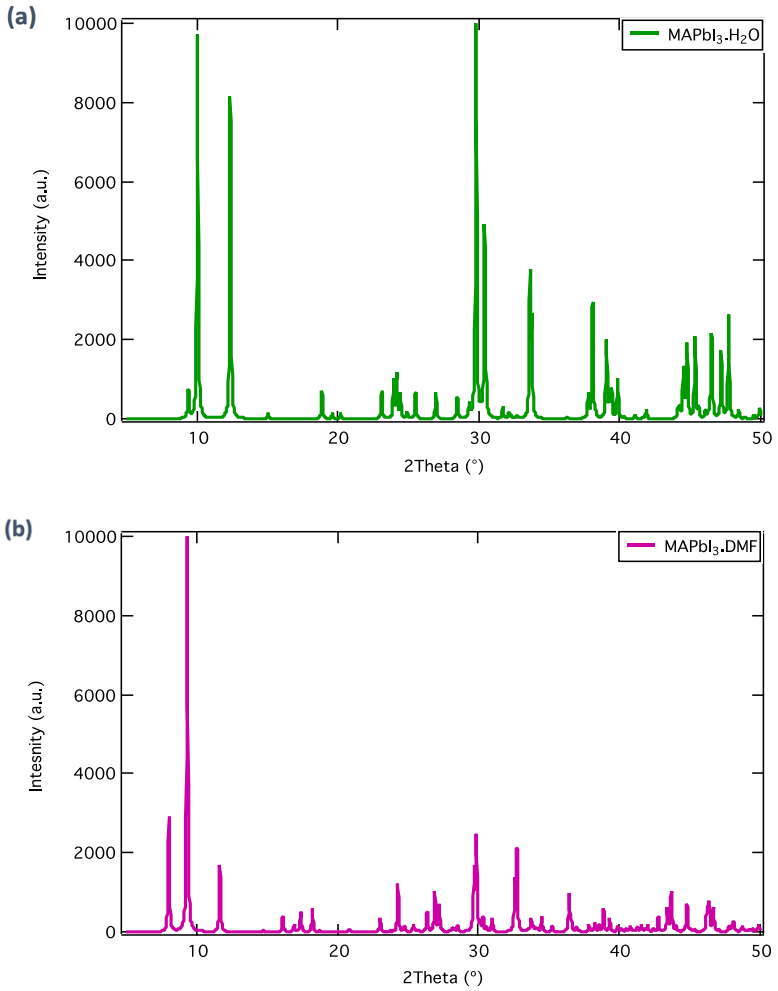

Figure 73: Simulated XRD diffractograms of possible intermediate perovskite compounds (a) $MAPbI_3.H_2O$ (b) $MAPbI_3.DMF$

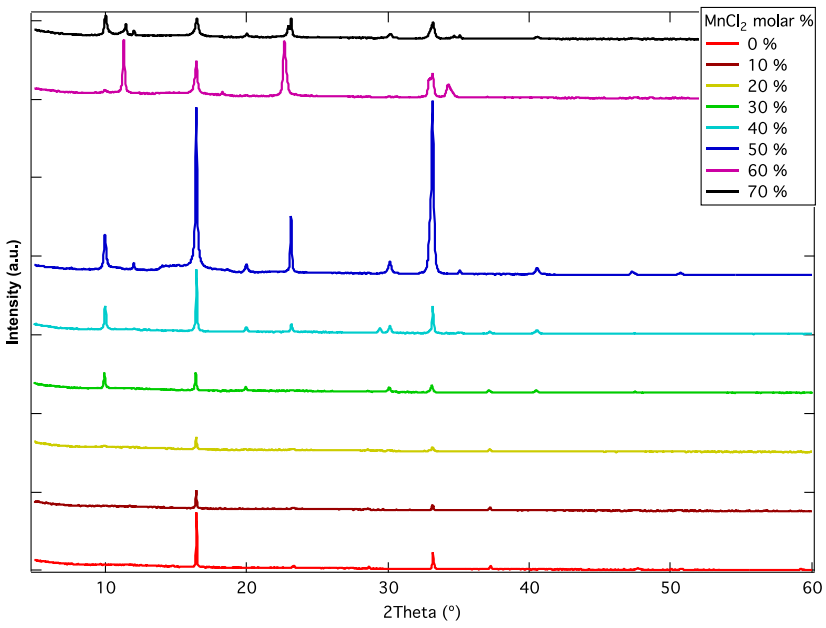

Figure 74: XRD diffractogram of perovskite films with increasing amount of $MnCl_2$

Appendix B

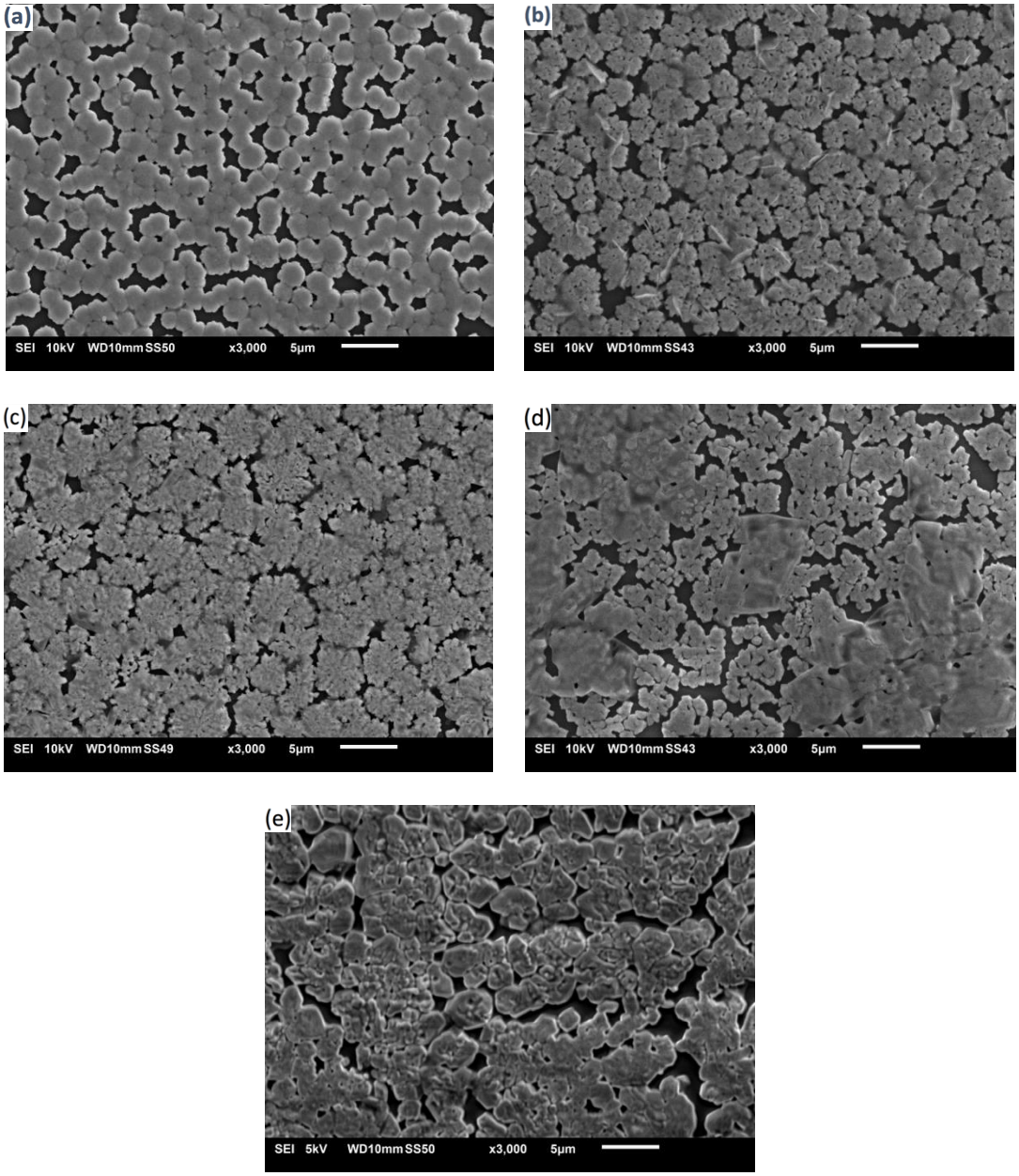

Figure 75: Secondary electron images of perovskite thin films synthesized using different molar % of $MnCl_2$ (a) 10 % (b) 20 % (c) 30% (d) 40 % (e) 50 %

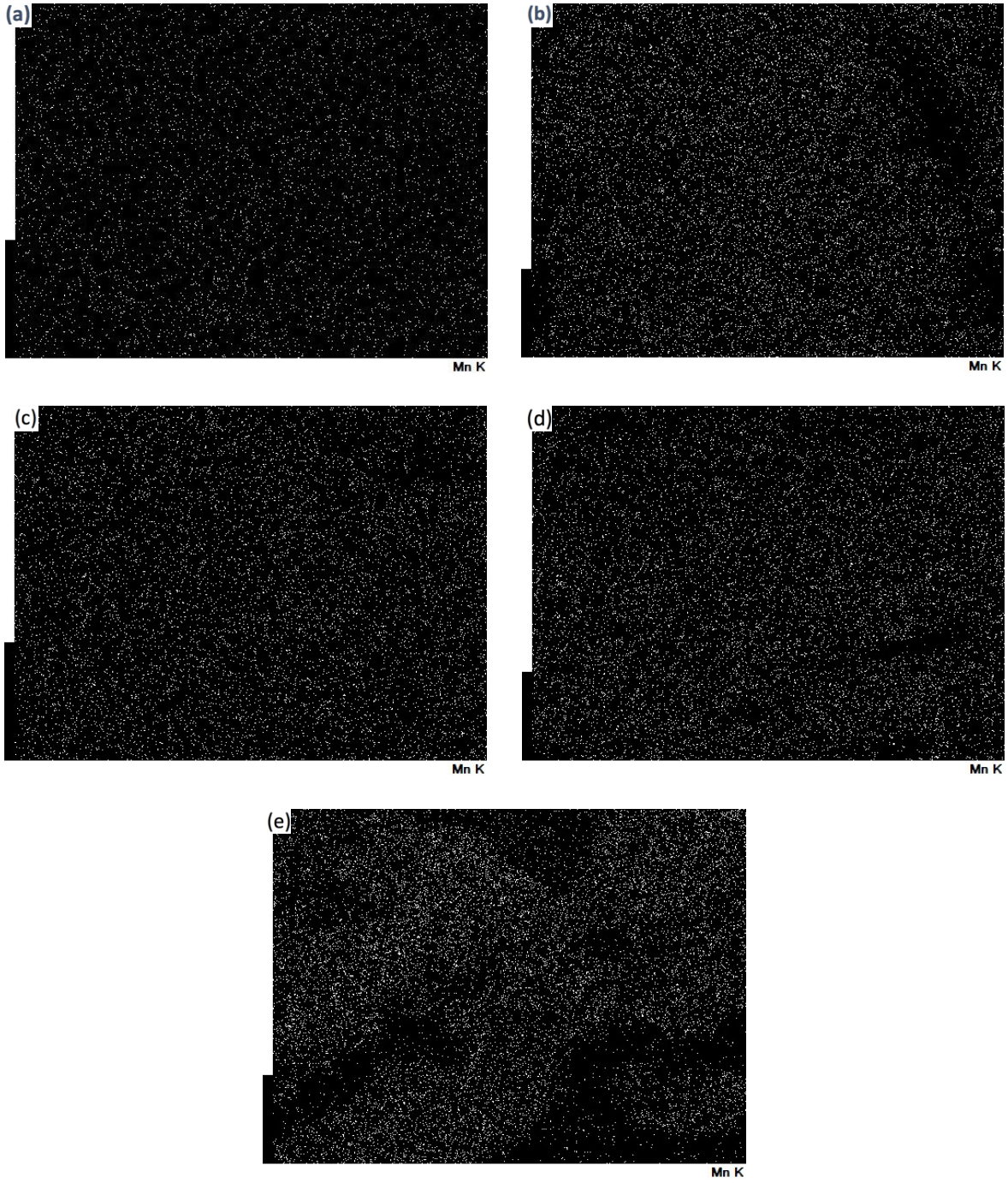

Figure 76: Elemental maps for manganese in perovskite thin films synthesized using different molar % of $MnCl_2$ (a) 10 % (b) 20 % (c) 30% (d) 40 % (e) 50 %

Appendix C

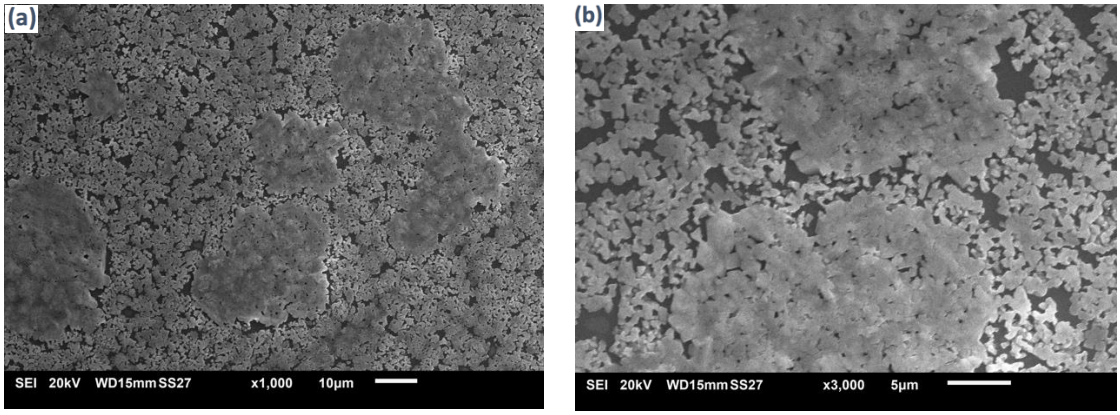

Figure 77: Secondary electron images of perovskite thin films synthesized using 30 molar % $MnBr_2$ (a) x1000 (b) x3000

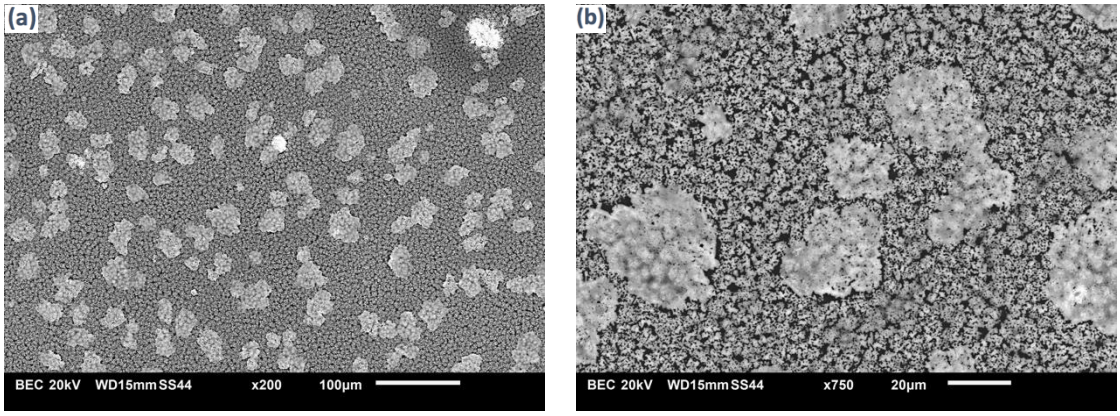

Figure 78: Backscattered electron images of perovskite thin films synthesized using 30 molar % $MnBr_2$ (a) x200 (x) x750

Appendix D

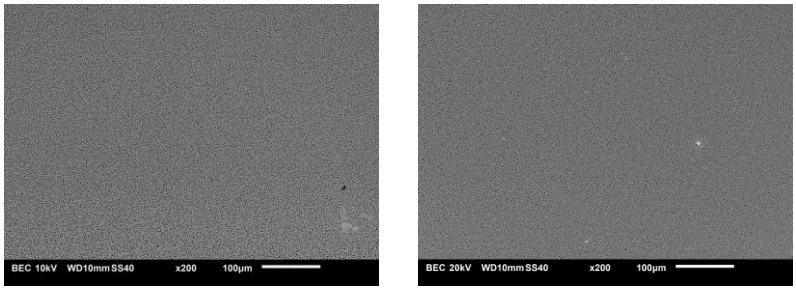

Figure 79: Backscattered electron images for 2.5:1 (MAI:metal salts) films annealed for (a) 30 mins (b) 60 mins

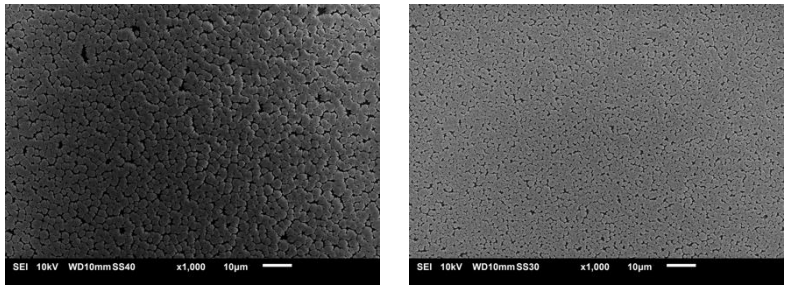

Figure 80: Secondary electron electron images for 2.5:1 (MAI:metal salts) films annealed for (a) 30 mins (b) 60 mins

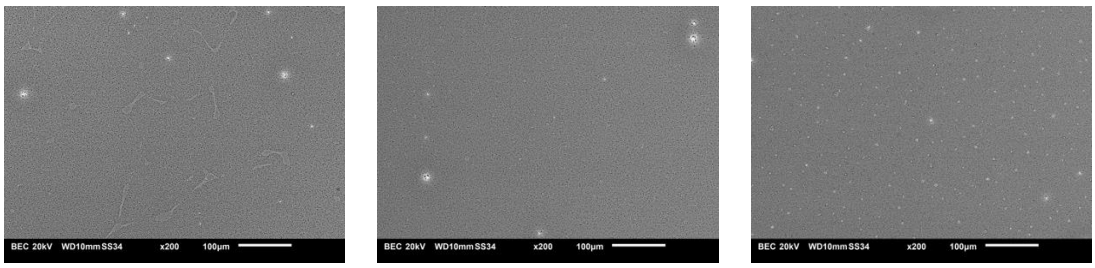

Figure 81: Backscattered electron images for 2:1 (MAI:metal salt) films annealed for (a) 30 mins (b) 60 mins (c) 120 mins

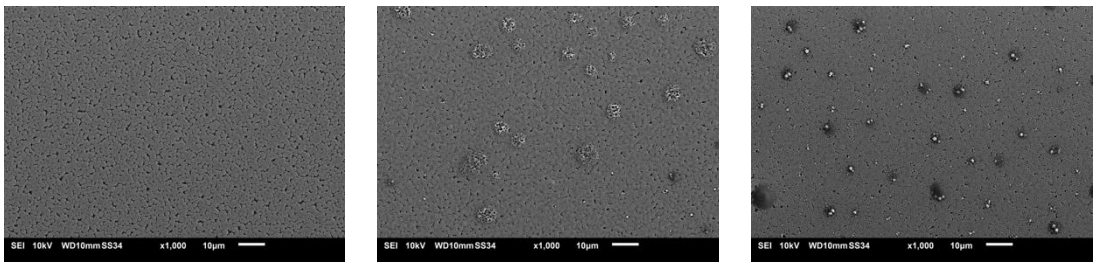

Figure 82: Secondary electron electron images for 2:1 (MAI:metal salts) films annealed for (a) 30 mins (b) 60 mins (c) 120 mins